Doctoral Dissertation
博士論文

Searches for Neutrinos from Astrophysical Origins Using Super-Kamiokande 20 years of High-energy Data
（スーパーカミオカンデ 20 年間の高エネルギーデータを用いた天体起源ニュートリノの探索）

A Dissertation Submitted for the Degree of Doctor of Philosophy
July　2025
令和 7 年 7 月博士（理学）申請

Department of Physics, Graduate School of Science,
The University of Tokyo
東京大学大学院理学系研究科物理学専攻

Xubin Wang
王　旭彬

Abstract

This thesis presents searches for high-energy astrophysical neutrinos from 1 GeV to 100 TeV using the Super-Kamiokande (SK) data from 1996 to 2019, corresponding to a total live-time of 6619.1 days. In this analysis, the live time is more than twice that of the previous analysis in SK. The unbinned maximum likelihood method is used to search for astrophysical neutrino excesses over the atmosphere neutrino. The data searched with is extended to all three high-energy samples, and energy information of the events are utilized and energy spectra of signals are fitted.

In addition to time-integrated search for ν_μ point sources, this analysis also include time-dependent search. While time-integrated search searches for neutrino spatial clusters from continuous emission sources, short-duration but intense emission may be diluted by background over a long time period. Time-dependent search is more sensitive to transient neutrino emission.

An improved event classification for fully-contained events is deployed to select charged current interacted ν_e-like events, and searches for high-energy astrophysical ν_e are performed with the selected data set. As atmosphere ν_e spectrum is much softer than ν_μ above 10 GeV, the fraction of background ν_e events, which dominate the observed data, can be sufficiently reduced by setting energy cut.

Recent result published by IceCube provides evidence of observation of high-energy diffuse neutrino from galactic plane. Since the model based on high-energy gamma-ray observations predicts a continuous diffuse neutrino spectrum down to the GeV region, and the cascade sample of IceCube used by that analysis consists of a considerable fraction of ν_e, the search for diffuse neutrino from the Galactic plane is performed using the selected ν_e like SK data that has visible energy above 10 GeV. This marks the first search for diffuse galactic ν_e in GeV region.

As the sources for cosmic ray acceleration in galaxy like supernova remnants and pulsar wind nebulae are candidates for diffuse neutrinos from galactic plane as well, this analysis also performed the stacked searches for ν_e from these types of galactic sources.

No significant excesses of high-energy astrophysical neutrinos over atmosphere neutrino background were found in any of the searches describe above. 90% confidence level upper limits of neutrino flux are set for the time-integrated and time-dependent search for ν_μ, in all search directions of the full-sky scan, and at the positions of the neutrino source candidates, in the energy range from 1 GeV to 100 TeV. This analysis also set neutrino flux upper limits of ν_e in the energy range from 10 GeV to 1 TeV on diffuse neutrino from the Galactic plane and stacked sources in the Galaxy, as well as the time-integrated search for point sources. The first flux upper limit on diffuse ν_e from the Galactic plane is set to $\left(\frac{d\Phi}{dE}\right)^{\mathrm{90C.L.}}_{\mathrm{diffuse}} = 7.5 \times 10^{-7}\ \mathrm{GeV}^{-1}\mathrm{cm}^{-2}\mathrm{s}^{-1} \cdot \left(\frac{\mathrm{E}_\nu}{10\mathrm{GeV}}\right)^{-2.7}$.

Acknowledgments

I am deeply grateful for the opportunity to be part of the Institute for Cosmic Ray Research at The University of Tokyo and to work with the outstanding members of the Super-Kamiokande Collaboration.

I am sincerely grateful to Professor Kimihiro Okumura, who provided me with the opportunity to explore astrophysical neutrino physics. The research journey was not always smooth, but thanks to Professor Okumura's guidance I overcame many challenges and developed the essential skills of an experimental physicist. His support also helped me acclimate to life in Japan and navigate the pandemic.

I also express my gratitude to Professor Yoshitaka Itow, whose keen insight guided my choice of research topic and deepened my understanding of fundamental physics.

I am truly thankful to Professor Roger Wendell for guidance on the technical details of atmospheric-neutrino reconstruction and simulation, and for helping me navigate the extensive Super-Kamiokande documentation.

I extend my appreciation to Professor Ed Kearns, Professor Magdalena Posiadala-Zezula, and Dr. Koun Choi for their insightful suggestions on manuscript structure and the presentation of results.

My thanks also go to Dr. Patrick de Perio and Dr. Takuya Tashiro for their help in understanding and applying machine-learning methods.

My heartfelt thanks to my friends—Junjie Xia, Seungho Han, Seisho Abe, Yosuke Ashida, Ka-Ming Tsui, Nahid Bhuiyan, Takuya Tomiya, Yushi Yoshioka, Shuoyu Chen, Lorenzo Perisse, Andres Munos, Christine Quach, Rhea Gaur, and Joshua Dilly—for making the life in the past five years so enjoyable. Special thanks to Junjie and Han-san for their support in research and in daily life in Kashiwa. I am also grateful to Mashima-san for her assistance with administrative procedures and for her thoughtful care.

My profound appreciation to my dear parents, from the bottom of my heart, for their unwavering support in every aspect and for encouraging me to pursue my dreams.

Contents

List of Figures

List of Tables

Chapter 1

Introduction

The observation of astrophysical neutrino (in comparison with atmosphere neutrino) can be traced back to solar neutrino and supernova neutrino observations in the last century. These astrophysical neutrinos are mainly generated via nuclei reactions and lepton-nucleon interactions, and the energies of such neutrinos are very low (typically in the MeV range). There is, however, another kind of astrophysical neutrino, which has a completely different origin, that IceCube observed in 2013. Such neutrinos have much higher energy (up to PeV) and are believed to be related to high-energy cosmic rays. The relation between high-energy neutrinos, cosmic rays, and gamma rays will be introduced later in this chapter.

There are several advantages of neutrino as a messenger to study high-energy astroparticle physics comparing to cosmic rays and gamma rays. Due to the existence of magnetic field in the galaxy, charged particles (which cosmic ray consists of) got deflected on the way of propagation. As a result, the arriving direction of cosmic rays on earth is de-correlated with their origins, making it difficult to identify the source of cosmic rays. Gamma ray, on the other hand, is neutral in charge, but high-energy gamma ray can be absorbed by celestial objects or interstellar medium, which make the flux of observed gamma ray in high-energy region very low. The advantage of using neutrino as a tool to study high-energy astroparticle physics is that it carries zero charge, is almost massless and has tiny cross section with all mater even with very high energies. These features almost guaranteed the coming direction and spectrum of neutrinos detected on Earth stay unchanged from the sources.

1.1 Cosmic Ray

Cosmic ray is composed with protons, helium nuclei and small fraction of electrons. The measured cosmic ray spectrum covers energy range from 10^8 to 10^{20} eV. The most interesting part for high-energy astroparticle physics would be from 10^{14} to 10^{20}. In general the energy spectrum of high-energy cosmic ray fluxes can be described by a power-law spectrum:

$$\frac{d\Phi}{dE} = \Phi_0 \times \left(\frac{E}{E_0}\right)^{-\gamma} \tag{1.1}$$

where Φ_0 is the flux normalization and γ is the spectrum index. $\gamma \approx 2.7$ from several GeV to about 100 TeV, but does not apply to higher energy range. As shown in Figure 1.1, there are three structures and a cut off at maximum energy.

The first turning point in the spectrum around 1 PeV is called the knee, as the spectrum

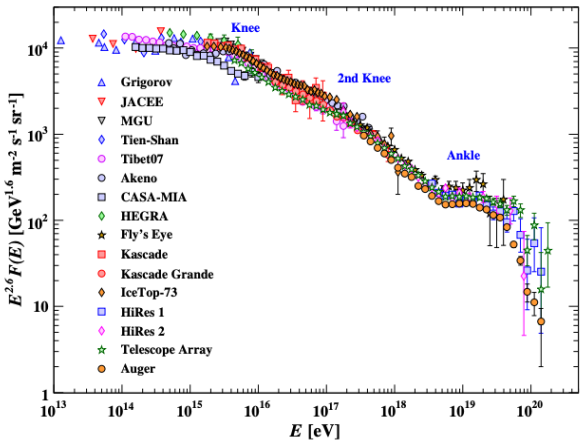

Figure 1.1: The flux spectrum of cosmic rays against energy-per-nucleus. Taken from Ref.[36].

steepens to $\gamma \approx 3.1$ after that point. At around 100 PeV, a second knee appears, but the spectrum is only slightly softer than in the region after first knee. As energy goes up to 1 EeV, the spectrum becomes harder and index is back to around 2.7 again. The cutoff occurs at the energy of 5 EeV.

One of the scenarios to explain the structures assumes that the spectrum is the sum of several power-law spectra with cutoffs, which results from different sources[37]. The chemical composition considered in this scenario usually includes the following groups of elements: hydrogen, helium, carbon and oxygen, and iron. Above the knee proton (hydrogen) reaches maximal energy by galactic accelerator[5]. At the energy of the second knee (which is about 26 times larger than knee), iron energy also reaches the maximum[5].

The other one assumes that the change of spectra indices are the results of extra-

galactic component scattering with cosmic microwave background (CMB). At the energies above the ankle, pair production from cosmic ray and CMB scattering occurs. At the cutoff energy, the scatter creates Δ resonance, which later decay into pions. Such cutoff is called Greisen-Zatsepin-Kuzmin (GZK) cutoff[55, 14].

1.1.1 Acceleration Mechanism

The spectrum of the cosmic ray suggests a non-thermal origin of high-energy cosmic rays, and acceleration mechanism is introduced to explain the hard spectrum. Fermi first proposed a mechanism in Ref. [8]. Acceleration happens at the boundary (called shock front) of two parts of media moving with different velocities when particle moves across the front and scatter on magnetic field of gas cloud. The particle gain energy when moving from low-speed (upstream) region to high-speed (downstream) region and lose energy vise versa. The energy gain of the particle passing through the shock front back and forth (called a cycle) is assumed to be proportional to its initial energy:

$$\Delta E = E' - E = \xi E \tag{1.2}$$

Then the energy of the particle after k cycles becomes $E_k = E_0(\xi + 1)^k$ where E_0 is the initial energy before being accelerated. Suppose the probability for a particle to escape the shock front in one cycle is p, the expected number of survived particles after k cycles is

$$N_k = N_0(1 - p)^k \tag{1.3}$$

where N_0 is the number of events has starting energy E_0. Putting them together

$$N(E > E_k) = \sum_{n=k}^{\infty} N_0(1-p)^n = N_0\frac{(1-p)^k}{p} = \frac{N_0}{p}(1-p)^{\frac{\ln(E_k/E_0)}{\ln(1+\xi)}} = \frac{N_0}{p}\left(\frac{E_k}{E_0}\right)^{\frac{\ln(1-p)}{\ln(1+\xi)}} \tag{1.4}$$

Let $\gamma = 1 - \frac{\ln(1-p)}{\ln(1+\xi)}$, and assume ξ is small so E_k is approximately continuous

$$\frac{dN}{dE} \approx \frac{N(E_k < E < \xi E_k)}{\xi E_k} = \frac{N_0}{E_k}\frac{1}{\xi p}\left(\frac{E_k}{E_0}\right)^{-\gamma+1}\left[1 - (\xi+1)^{-\gamma+1}\right] = \frac{N_0}{\xi E_0}\left(\frac{E_k}{E_0}\right)^{-\gamma} \tag{1.5}$$

The first order Fermi acceleration is achieved in the process of particle crossing the shock front. For mono-atomic ideal gas, the ratio of the velocity of upstream u_1 and down stream u_2 in the shock front reference system is $u_1/u_2 = 4$[29]. As the velocity distribution of the relativistic particles in both region are isotropic, they see a $V = 3/4U$ speed relative to the medium, where U is the velocity of the shock front, both when they move from the upstream to downstream and vice versa. According to Ref.[29] energy gain in one cycle

is thus

$$\xi = \frac{4}{3}\frac{V}{c} = \frac{U}{c} \tag{1.6}$$

The escape probability of a particle in one cycle is given by $p = 4u_2/c = U/c$[29], so the power law spectra index γ can be approximated by

$$\gamma = 1 - \frac{\ln(1-p)}{\ln(1+\xi)} = 1 - \frac{\ln(1-U/c)}{\ln(1+U/c)} \approx 2 \tag{1.7}$$

when $U \ll c$ (non-relativistic shock). In reality, however, the spectrum of cosmic rays observed on Earth is softer, as a result of the existence of relativistic shock and secondary particle generation.

There is a maximum energy that can be reached within an acceleration. When the Larmor-radius of particle with energy E and unit of charge Z is larger than the acceleration region, it can no longer be constrained within the acceleration by the magnetic field. So the maximum energy is given by

$$E_{max} = \mathrm{PeV} \cdot Z \cdot \frac{B}{\mathrm{G}} \cdot \frac{R}{\mathrm{pc}} \tag{1.8}$$

where B and R are the magnetic field and size of the acceleration region, respectively. Such criteria is known as Hellas criteria[26]. Figure 1.2 shows the relation between the size and magnetic and the corresponding maximal energy for different sources.

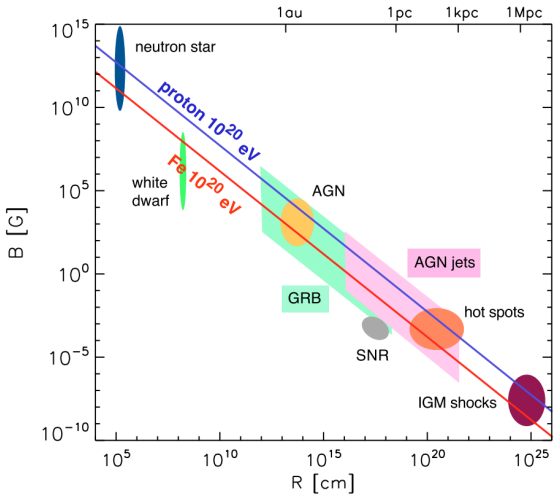

Figure 1.2: Hillas diagram. Taken from Ref. [26]

1.2 High-energy Neutrino Production

As cosmic rays being accelerated to a certain energy, they interact with interstellar media (proton or heavier nuclei) or high-energy high-luminosity gamma rays via the following process:

$$\begin{aligned} p + p &\to X + \pi^{\pm} \\ &\to X + \pi^{0} \\ p + \gamma \to \Delta &\to p + \pi^{0} \\ &\to n + \pi^{+} \end{aligned} \tag{1.9}$$

Following the production of pions, they decay through the channel

$$\begin{aligned} \pi^{+} &\to \mu^{+} + \nu_{\mu} \\ \pi^{-} &\to \mu^{-} + \bar{\nu}_{\mu} \\ \pi^{0} &\to \gamma\gamma \end{aligned} \tag{1.10}$$

The energy carried by the pions is about $0.2/A$ of the cosmic ray energy, with A being the atomic number. The neutrino will carry 0.25 of the pion energy on average, while gamma ray carry 0.5[33]. This means the neutrino and gamma ray created from cosmic rays will succeed the spectrum of cosmic rays. Using energy conservation, the gamma ray and neutrino spectrum can be connected through the following equation

$$\int_{E_\gamma^{min}}^{E_\gamma^{max}} E_\gamma \frac{d\Phi_\gamma}{dE_\gamma} dE_\gamma = K \int_{E_\nu^{min}}^{E_\nu^{max}} E_\nu \frac{d\Phi_\nu}{dE_\nu} dE_\nu \tag{1.11}$$

with $K = 1$ for pp collision and $K = 4$ for $p\gamma$ interaction[16]. Since the gamma ray can also be created by cosmic rays via synchrotron radiation, bremstrahlung or inverse Compton scattering, the observation of neutrino flux will help to constrain the composition of gamma rays.

The muons decayed from pions are not stable and will further decay via

$$\begin{aligned} \mu^{+} &\to e^{+} + \bar{\nu}_{\mu} + \nu_{e} \\ \mu^{-} &\to e^{-} + \nu_{\mu} + \bar{\nu}_{e} \end{aligned} \tag{1.12}$$

Neutrons from $p\gamma$ interaction will also decay

$$n \to p + e^{-} + \bar{\nu}_{e}$$

In both of these two processes electron neutrino is generated. The ratio of the three flavor neutrino flux at source will be $(\nu_e : \nu_\mu : \nu_\tau) = (1 : 2 : 0)$ if the contributions from pion and muon decay are the same. This will generally be the case when the magnetic field at the source is small, as the life time of pion and muon are small. However, if the magnetic field is strong, the synchrotron radiations of pion and muon are not negligible. The synchrotron radiation will reduce the energy of particle, and thus suppress some of the decay process. The sources include muon damped source where muon lose most energy before decay and have a ratio of $(\nu_e : \nu_\mu : \nu_\tau) = (0 : 1 : 0)$, and neutron beam source where both pion and muon lose most energy before decay, with the ratio $(\nu_e : \nu_\mu : \nu_\tau) = (1 : 0 : 0)$[20]. Thus the neutrino flavor ratio will help to understand the acceleration mechanism of the neutrino source.

However, the ratio will not stay unchanged during the propagation to Earth. Although the interaction with other particle of all flavors are negligible due to small cross section, neutrino will go through the so called oscillation and flavor can change after long-distance propagation.

1.2.1 Neutrino Oscillation

In the neutrino oscillation theory, the neutrino flavor eigenstates are assumed to be mixtures of neutrino mass eigenstates. The transformation from mass states to flavor states is represented by the so called Pontecorvo-Maki-Nakagawa-Sakata (PMNS) matrix[38, 30]:

$$\begin{pmatrix} \nu_e \\ \nu_\mu \\ \nu_\tau \end{pmatrix} = \begin{pmatrix} \mathbf{U}_{e1} & \mathbf{U}_{e2} & \mathbf{U}_{e3} \\ \mathbf{U}_{\mu 1} & \mathbf{U}_{\mu 2} & \mathbf{U}_{\mu 3} \\ \mathbf{U}_{\tau 1} & \mathbf{U}_{\tau 2} & \mathbf{U}_{\tau 3} \end{pmatrix} \begin{pmatrix} \nu_1 \\ \nu_2 \\ \nu_3 \end{pmatrix}$$

The the neutrino in flavor eigenstate of α is expanded to

$$|\nu_\alpha\rangle = \sum_{i=1}^{3} \mathbf{U}_{\alpha,i} |\nu_i(0)\rangle \tag{1.13}$$

After propagation of time t, the neutrino state becomes

$$|\nu_\alpha(t)\rangle = \sum_{i=1}^{3} \mathbf{U}_{\alpha,i} e^{-iE_i t} |\nu_i(0)\rangle \tag{1.14}$$

where E_i is the energy eigenvalue. The probability to observe a neutrino of flavor α as flavor β is given by

$$P_{\nu_\alpha \to \nu_\beta} = |\langle \nu_\beta(t) | \nu_\alpha(0) \rangle|^2 \tag{1.15}$$

$$= \left| \sum_{i=1}^{3} \mathbf{U}^*_{\beta,i} \mathbf{U}_{\alpha,i} e^{-E_i t} \right|^2 \tag{1.16}$$

$$= \sum_{i=1}^{3} |\mathbf{U}^*_{\alpha,i} \mathbf{U}_{\beta,i}|^2 + \sum_{j \neq i} \mathbf{U}^*_{\alpha,j} \mathbf{U}_{\beta,j} \mathbf{U}_{\alpha,i} \mathbf{U}^*_{\beta,i} e^{-(E_i - E_j)t} \tag{1.17}$$

$$\tag{1.18}$$

Since the neutrino mass compared with the energy of astrophysical neutrino of interest is very small, the energy can be approximated by $E_i \approx E + \frac{m_i^2}{2E}$ where E is the energy of neutrino. Thus $(E_i - E_j)t \approx \frac{\Delta m_{ij}^2 L}{2E}$ where L is the distance traveled by the neutrino in time t, and $\Delta m_{ij}^2 = m_i^2 - m_j^2$. Now the probability can be written by

$$P_{\nu_\alpha \to \nu_\beta} = \delta_{\alpha\beta} \tag{1.19}$$

$$- 4 \sum_{j>i} \mathrm{Re}(\mathbf{U}^*_{\alpha,j} \mathbf{U}_{\beta,j} \mathbf{U}_{\alpha,i} \mathbf{U}^*_{\beta,i}) \sin^2 \left(\frac{\Delta m_{ij}^2 L}{4E} \right) \tag{1.20}$$

$$+ 2 \sum_{j>i} \mathrm{Im}(\mathbf{U}^*_{\alpha,j} \mathbf{U}_{\beta,j} \mathbf{U}_{\alpha,i} \mathbf{U}^*_{\beta,i}) \sin \left(\frac{\Delta m_{ij}^2 L}{2E} \right) \tag{1.21}$$

Since the astrophysical neutrino sources are very far away from the Earth, in the very long-distance oscillation process, e.g. $L \gg \frac{4\pi E}{|\Delta m_{ij}^2|}$, the oscillation pattern got averaged out, with $\left\langle \sin \left(\frac{\Delta m_{ij}^2 L}{2E_\nu} \right) \right\rangle = 0$ and $\left\langle \sin^2 \left(\frac{\Delta m_{ij}^2 L}{4E_\nu} \right) \right\rangle = 1/2$[36]. The probability now becomes

$$P_{\nu_\alpha \to \nu_\beta} = \sum_{i=1}^{3} \mathbf{U}^*_{\alpha,i} \mathbf{U}_{\beta,i} \mathbf{U}_{\alpha,i} \mathbf{U}^*_{\beta,i} \tag{1.22}$$

The expected ratio at Earth is $(\nu_e : \nu_\mu : \nu_\tau) = (1 : 2 : 0) \to (\nu_e : \nu_\mu : \nu_\tau) \approx (1 : 1 : 1)$, $(\nu_e : \nu_\mu : \nu_\tau) = (0 : 1 : 0) \to (\nu_e : \nu_\mu : \nu_\tau) \approx (0.6 : 1.3 : 1.1)$, and $(\nu_e : \nu_\mu : \nu_\tau) = (1 : 0 : 0) \to (\nu_e : \nu_\mu : \nu_\tau) \approx (1.6 : 0.6 : 0.8)$, respectively, given the current measured oscillation parameter[45].

1.3 Sources of High-energy Astrophysical Neutrino

There are sources that satisfy the condition of both acceleration mechanism and pp or $p\gamma$ interactions and thus can be considered as source candidates of high-energy astrophysical neutrino. The candidates can be galactic and extra-galactic.

1.3.1 Supernova Remnant (SNR)

After the star life ends with a core-collapse supernova, most of the energy will be released by thermal neutrino. Some of the stellar material are also ejected and first encounters the circumstellar material (CSM) and then reaches interstellar material (ISM), creating fast-moving shock wave, which is the candidate for the first order Fermi acceleration source. The shock front will sweep up surrounding gas and dust and keep accelerating them. The strong magnetic field in the medium ensures a high maximum energy that can be accelerated to. As the shock front expand and the radius increase, the matter density per solid angle remains almost unchanged but the density per volume decrease with respect to $1/R_{SN}^3$. When the density of shock front drops to the same level as ISM, the acceleration becomes inefficient. The lifetime of the shock wave can be estimated by the density and velocity of shock front (obtained from mass of supernova). The estimated life time is about the order of 1000 years, which is enough to provide acceleration energy[42]. The expected rate for supernova with mass of $\sim 10M_\odot$, where $M_\odot$ is the solar mass, is about 2 per century. A few percent of the power output from supernova is sufficient for the energy of the cosmic rays in the galaxy[44]. The maximum energy that can be accelerated to by Type II with 1500 years life time is around $E_{max} \approx Z \times 100\text{TeV}$[27].

1.3.2 Pulsar Wind Nebula (PWN)

Pulsars are fast-rotating neutron stars with strong magnetic field formed from supernova explosion. The fast rotating magnetic field will generate strong electric field near the pulsar surface, which pull electrons out and accelerate them. The electrons moves in spiral and emit synchrotron radiation, which undergo pair production in the magnetic field. The electrons and positrons being ejected form magnetic plasma, called pulsar wind. When the pulsar wind interact with the ambient material (eg. from SNR), a termination shock occurs, which is the potential source of Fermi acceleration.

1.3.3 Active Galactic Nucleus

Active galactic nucleus (AGN), different from SNR and PWN, is extra-galactic source. It is a region at the center of a high-luminosity galaxy. In the center, a supper-massive black hole is surrounded by accretion disc. As matter in the accretion disc falls into black hole, gravitational energy is converted to radiation. Two relativistic jets perpendicular to the accretion disc pointing opposite direction are emitted. Figure 1.3 shows a schematic of the structure of AGN. The jets can be collimated and accelerated by the magnetic field, and become a source of shock acceleration. An interesting process may happen in the center region of AGN, where the protons interact with internal radiation, creating photons being absorbed and lower-energy protons captured, and leaving only neutrinos to

flee [32]. The AGNs are generally classified with respect to the radio emission, luminosity and the jet orientation to Earth. If one of the jet is pointing close to Earth, is it called blazar[4].

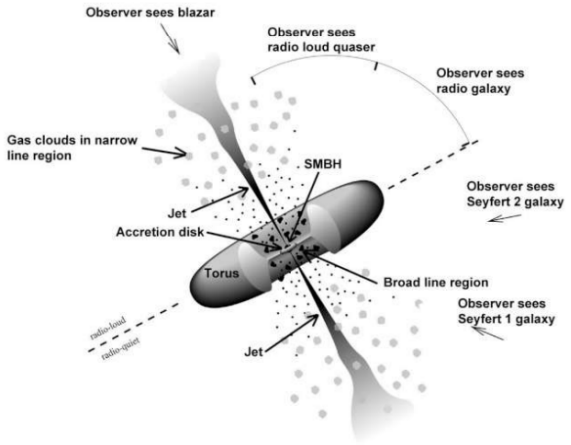

Figure 1.3: Schematic of an AGN with the supper massive black hole in the center, accretion disc and dust torus surrounding it and jets emitted perpendicular to the disc. Taken from Ref. [9].

1.3.4 Galactic Plane

Galactic plane is also a promising source of high-energy astrophysical neutrinos. The neutrinos may have two components: one is diffused cosmic rays interacting with the ISM in the galaxy, and the other is sources of acceleration in the galaxy (like SNR or PWN). In this sense galactic plane is not a single source, but a combination of several population of sources.

When cosmic rays propagating in the galaxy, pions are created via *pp* interactions with ISM, which later decay into photons, neutrinos and finally electrons, as discussed in Section 1.2. The gamma rays from the π^0 decays are referred to gamma rays from hadronic process. The electrons created from this process can undergo synchrotron radiation with the magnetic field in galaxy, bremstrahlung with charged particles, or inverse Compton (IC) scattering on low-energy photons and emit gamma rays as well[29]. These processes are called leptonic process. The diffuse flux of gamma ray observed on Earth by observatories like Fermi Large Area Telescope (Fermi-LAT) is the combination of these two processes.

Fermi-LAT collaboration simulated the spatial distribution and energy spectra of Galactic diffuse gamma-ray emission (DGE) from models with different model param-

eters and compared to the observed data. Figure 1.4 shows a comparison of spatial distribution between the observed data and model prediction of ${}^{S}S^{Z}4^{R}20^{T}150^{C}5$, and the spectra in the center galaxy region ($|b| < 8°, |l| < 80°$) is shown in Figure 1.5.

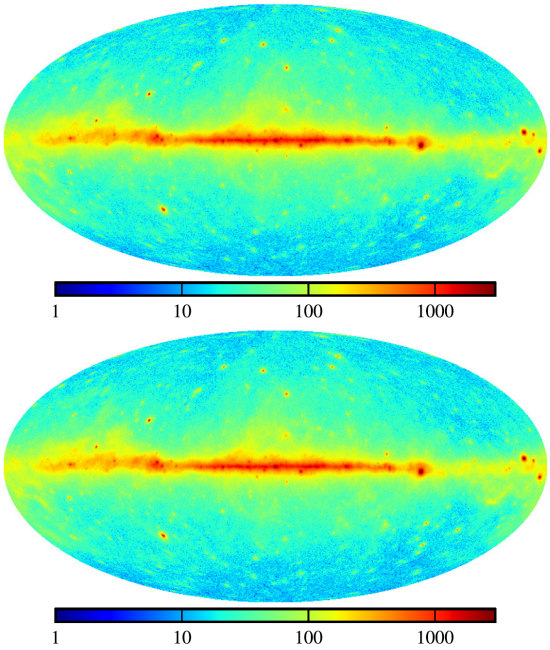

Figure 1.4: Gamma ray counts in galactic plane observed by Fermi-LAT (upper) and predicted by ${}^{S}S^{Z}4^{R}20^{T}150^{C}5$ (lower). Taken from Ref.[1].

More recent observations of high-energy and ultrahigh-energy gamma rays were made by ARGO-YBJ and Tibet AS+MD collaborations respectively. The observed results are shown in Figure 1.6 and Figure 1.7. The flux spectrum is consistent with a single power-law spectrum from 1 GeV to 100 GeV energy range, and become harder above 100 GeV. The spatial distribution by ARGO-YBJ shows agreement with the Fermi-DGE model.

The neutrino from sources in the galaxy follows the same mechanism of each source. As discussed in Section 1.3.1, SNRs are potential sources. In Ref.[31], lepto-hadronic models based on GeV gamma ray and radio observation are established for 21 well-studied SNR. The predicted neutrino flux spectra for each source and the total flux are shown in Figure 1.8.

The neutrino flux of the unresolved SNR is estimated by the radio observation, and diffuse neutrino from SNRs in galaxy is calculated by adding the resolved and unresolved SNRs (see Figure 1.9).

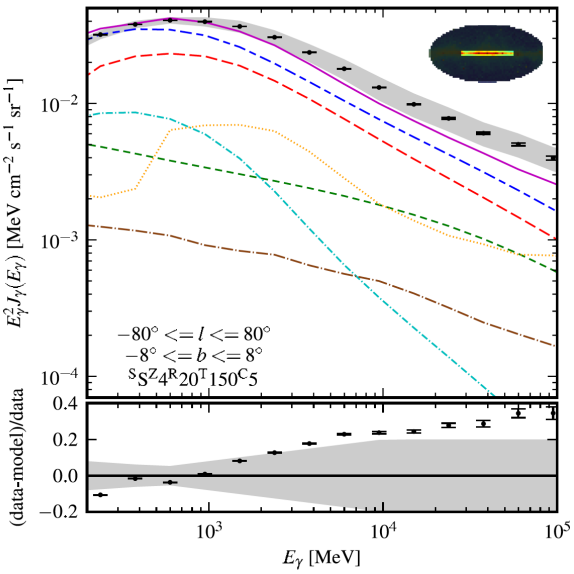

Figure 1.5: Energy spectra of gamma ray in inner galaxy ($|b| < 8°, |l| < 80°$), with isotropic background (brown), detected sources (orange), model compositions from π^0 decay (red), IC (green) and bremstrahlung (cyan), the sum of three components (blue) and total emission including source and background (magenta). Taken from Ref.[1]

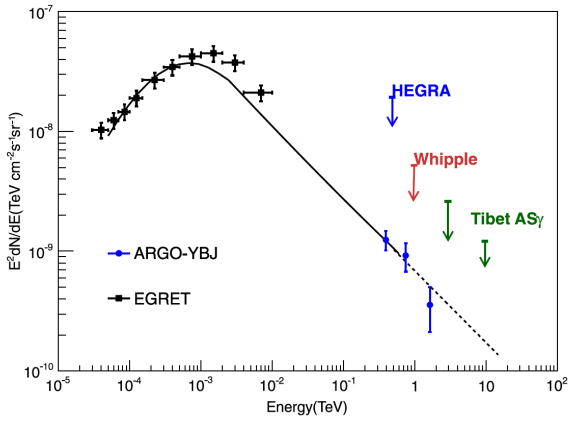

Figure 1.6: Energy spectra from ARGO-YBJ observatories in Galactic plane region of $|b| < 5°$ and $25° < l < 100°$. Taken from Ref.[3].

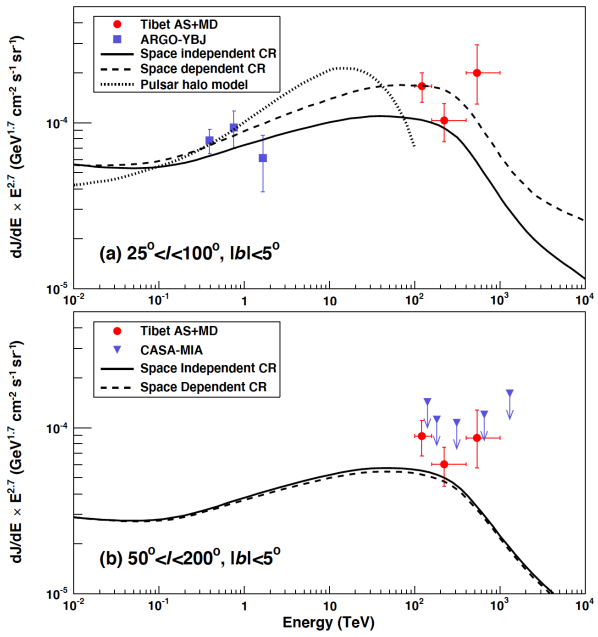

Figure 1.7: Energy spectra from Tibet AS+MD observatories in Galactic plane region of $|b| < 5°, 25° < l < 100°$ (upper) and $|b| < 5°, 50° < l < 200°$ (lower). Taken from Ref.[52].

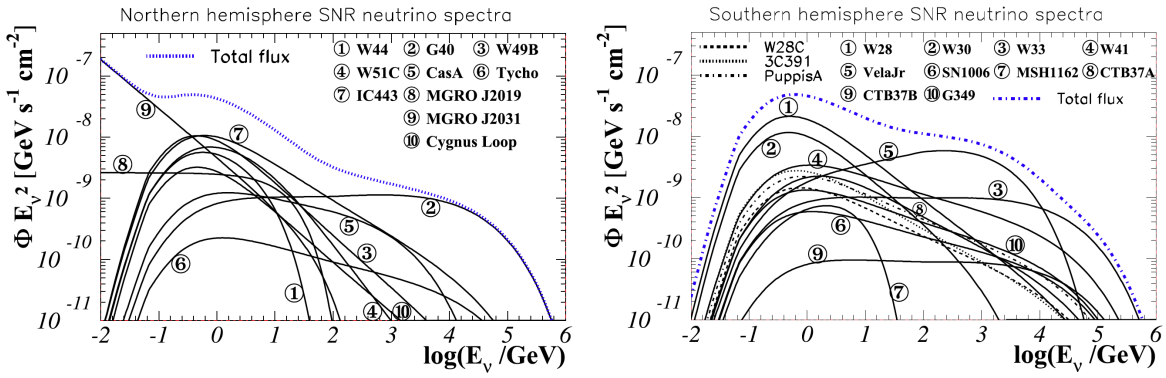

Figure 1.8: Model predicted neutrino fluxes from SNR in northern hemisphere (upper) and southern hemisphere (lower). Taken from Ref.[31]

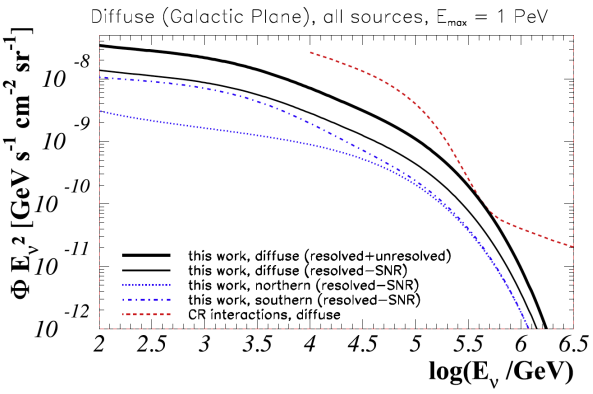

Figure 1.9: Model predicted diffuse neutrino flux from SNR in the galaxy, in comparison with model predicted diffuse neutrino flux from diffuse cosmic ray interactions. Taken from Ref.[31]

1.4 High-energy Astrophysical Neutrino Observation

So far there have been several observations or evidences of observation being made by neutrino observatories. In 2017, a 290 TeV energy muon neutrino, IC170922A, was detected by IceCube and a real-time alert was issued. Following this alert, gamma ray telescope Fermi-LAT and MAGIC found a blazar TXS 0506+056, of which the location coincide with the neutrino direction, in flaring state (Figure 1.10[7]). This marks the first evidence of high-energy neutrino from point source.

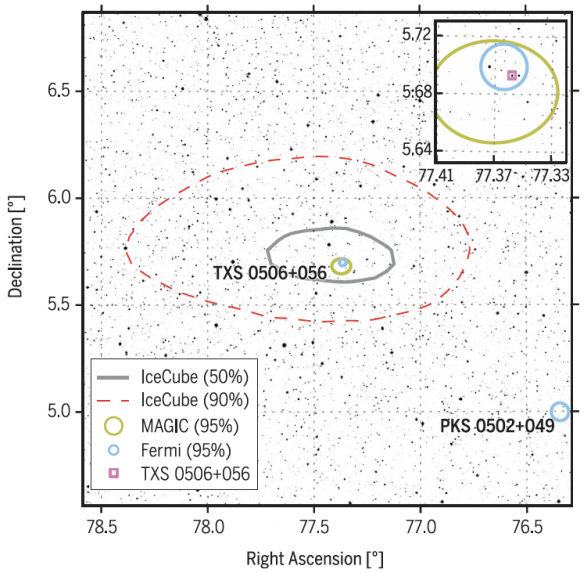

Figure 1.10: TXS 0506+056 (pink square in top right zoomed in sub figure), Firmi-LAT previous detection (blue circle), MAGIC follow-up detection (yellow circle) and IceCube observation (gray and red circle). Taken from Ref.[7].

IceCube later performed a time-dependent search independent from IC170922A near

the location of TXS 0506+056[23]. In this search, an excess of transient emission of neutrino two years before IC170922A was found (Figure 1.11), with significance exceed 3.5σ. The neutrino fluence normalization times square of neutrino energy is fitted to $2.1 \times 10^{-4}\mathrm{TeVcm}^{-2}$ at 100 TeV with a spectrum index $\gamma = 2.1$. This result provides strong evidence that TXS 0506+056 is a point source of high-energy astrophysical neutrinos.

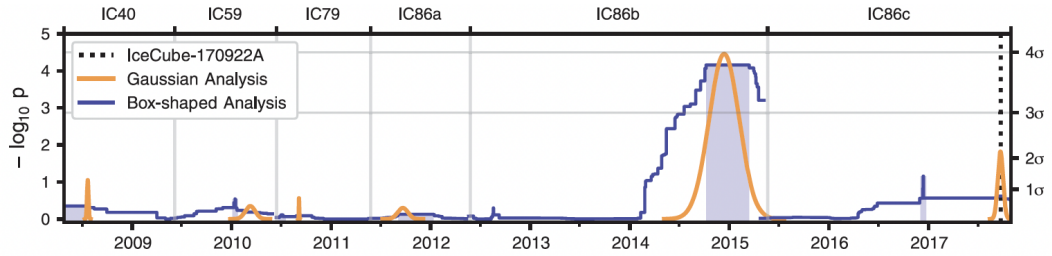

Figure 1.11: The significance of results from time-dependent search around TXS 0506+056. Significant excess of transient neutrino emission was seen around 2015. High-energy event IC170922A is marked by black dashed line, and does not contribute to the excess in 2015. Taken from Ref.[23].

Another source that has been found with evidence to be high-energy neutrino source is NGC 1068. In the full sky scan of time-integrated search, the most significant search direction is 0.35° away from an active galaxy, NGC 1068[22]. The post-trial p-value of the result at that direction after taking into account the trial factor of looking elsewhere is not significant enough, but NGC 1068 stands out in the search with a list of candidates with a global significance of 4.2σ. The neutrino flux normalization from location of NGC 1068 is fitted to $5\times10^{-11}\mathrm{TeV}^{-1}\mathrm{cm}^{-2}\mathrm{s}^{-1}$ at 1 TeV with $\gamma = 3.2$, as presented in Figure 1.12.

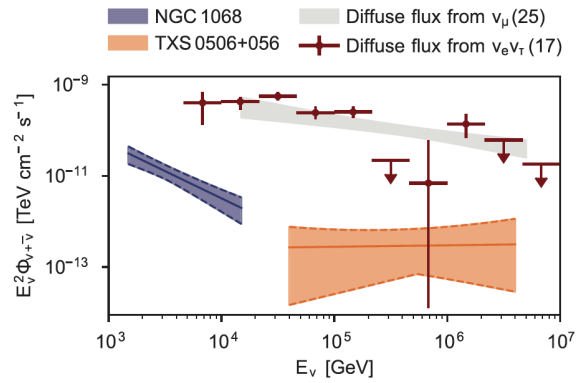

Figure 1.12: Result of neutrino flux from NGC 1068 (blue), together with neutrino flux from TXS 0506+056 (orange). Taken from Ref.[22]

One of the most recent result is the evidence of observing diffuse neutrino from Galactic plane by IceCube[21]. The search was performed with cascade events, which mainly

consists of ν_e and ν_τ. The π^0 model introduced in Section 1.3.4 is implemented as the sky template, and γ is assumed to be 2.7. KRA_γ^5 and $\mathrm{KRA}_\gamma^{500}$ model, which introduce cut-offs at certain energies to the π^0 model, are also used as template and performed search with. Significant excesses exceeding 3σ are found with all three model templates inside the Galactic plane region $|b| < 15°$. The best fitted neutrino flux using three models are presented in Figure 1.13.

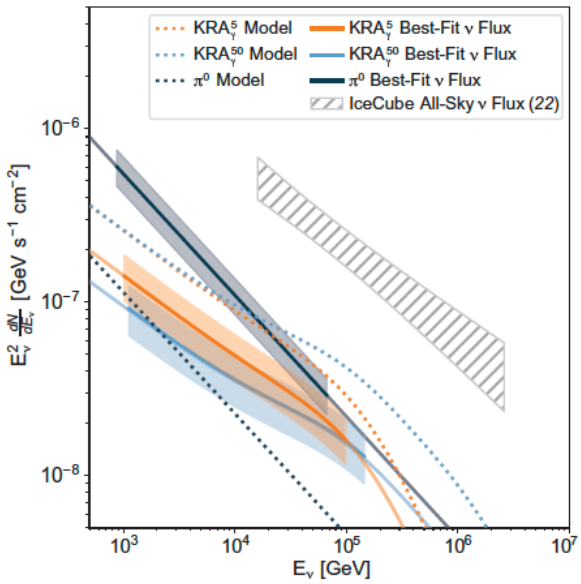

Figure 1.13: Flux of diffuse neutrino from Galactic plane vs neutrino energy from IceCube search result. The best fitted fluxes (solid) using three model templates are shown together with the fluxes from model prediction (dashed). Taken from Ref.[22].

1.5 Introduction to Thesis

In this thesis, results for searches for high-energy astrophysical neutrinos is presented. The searches use data of three SK high-energy samples, covering neutrino energy range from GeV to TeV collected over 6619.1 days of live-time. Unbinned maximum likelihood is deployed to search for signals exceeding from atmosphere neutrino background. Searches include time-integrated and time-dependent full-sky scans for astrophysical ν_μ and ν_e point sources, time-integrated search for astrophysical ν_μ and ν_e with lists of source candidates, search for diffuse ν_e from galactic plane and stacked search for ν_e from SNR, PWN and UNID in galaxy.

The previous search for high-energy astrophysical neutrino in SK was performed by Eric Thrane in 2008[51], in which time-integrated search for ν_μ point sources using data of UPMU sample from SK-I to SK-III was performed. This analysis extended the data to FC, PC and UPMU samples from SK-I to SK-V, which is about twice live-time of SK-I

to SK-III. The fractions of signal events from three samples is introduced to fit energy spectrum for the first time in SK. This analysis also implemented a developed neutrino flavor selection for FC sample and performed the first search for high-energy astrophysical ν_e with the selected data sample in SK. Time-dependent search for point source, as well as search for diffuse neutrino from galactic plane and stacked search for neutrino sources in galaxy are new searches in this analysis.

Chapter 2

The Super-Kamiokande Detector

Super-Kamiokande is a water Cherenkov detector located under Mt. Ikenoyama in Japan. The distance from the detector to the top of the mountain is about 1,000 meters, which is equivalent to 2,700 meters deep water, and cosmic rays are shielded by the mountain. The main part of the detector is a cylindrical water tank with 41.4 m in hight and 39.3 m in diameter and containing 50 kt of ultra-pure water. Illustration of the detector is shown in Figure 2.1 The construction of the detector was completed in 1996 and data taking started from April 1st in the same year. The data-taking periods are divided into five water phases, SK-I to SK-V, and Gd phases. From 2020 SK Gd phases started with loading of gadolinium into the water in detector. This analysis only uses data taken in five SK water phases. Each phase has different dector configuration and is summarized in Table 2.1. In 2001 before the beginning of SK-II, one photomultiplier tube (PMT) imploded, which caused a chain reaction. Since more than have of the PMTs are destroyed, SK-II operated with 19% of photocathode coverage. Replacement PMT installation started from July 2006 and SK-III began operation with photocathode coverage back to 40%. After SK-III, upgrades were implemented to electronics and data acquisition systems. SK-IV operated steadily for almost 10 years before tank opening in 2018. During the opening new water system was installed and refurbishment like replacing failed PMT and cleaning were also made. The last water phase SK-V started after the work and ended in 2020.

Table 2.1: Summary of start/end time, live time, photocathode coverage and electronics of SK water phases.

Phase	Running Period	Live Time (days)	Photocathode Coverage	Electronics
SK-I	1996/05-2001/07	1489.2	40%	ATM
SK-II	2002/10-2005/10	798.6	19%	ATM
SK-III	2006/07-2008/08	518.1	40%	ATM
SK-IV	2008/09-2018/05	3244.4	40%	QBEE
SK-V	2019/02-2020/07	461.0	40%	QBEE

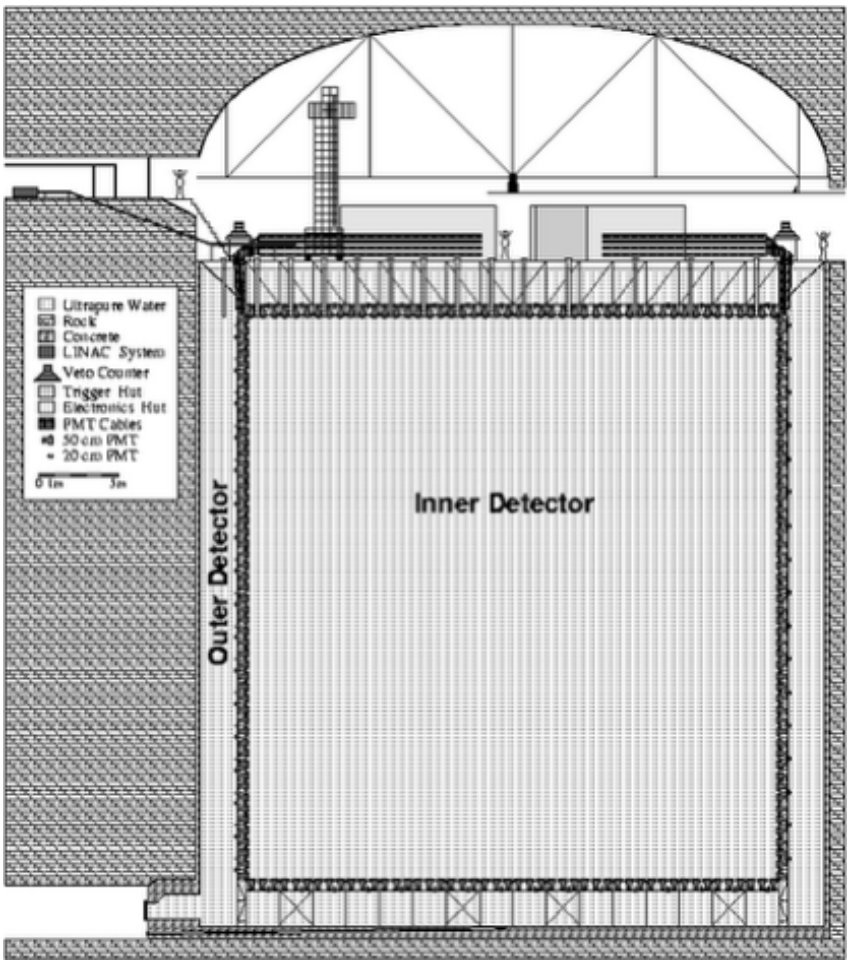

Figure 2.1: Illustration of SK detector. Taken from Ref.[11].

2.1 Cherenkov Radiation

When charged particles that travel with a speed larger than the speed of light in water, they emit Cherenkov radiation, which is used by SK for detection. The emitted lights go outward and form a shape of cone. Kinematic energy threshold to emit Cherenkov radiation for a particle with rest mass of m in the medium or refractive index n is

$$p_{thr} = \frac{mc}{\sqrt{n^2 - 1}} \tag{2.1}$$

The refractive index is dependent on wave length of photon, but for water it can be approximated with $n \approx 1.33$. The momentum threshold of Cherenkov radiation is about 1.14 times of the particle mass, which is 0.57 MeV/c for electron, 118 MeV/c for muon, 156 MeV/c, and 1052 MeV/c for proton.

The opening angle of the cone is given by:

$$\theta_C = \arccos\left(\frac{1}{n\beta}\right) \tag{2.2}$$

where $\beta = v/c$. For an ultra-relativistic particle, where $\beta \approx 1$, the Cherenkov opening angle is $\theta \approx 42°$.

Number of photons emitted per unit length of traveling per wave length through Cherenkov radiation is

$$\frac{dN}{dxd\lambda} = 2\pi\alpha Z^2 \left(1 - \frac{1}{n^2\beta^2}\right) \frac{1}{\lambda^2} \tag{2.3}$$

where α is the fine-structure constant, Z is the charge of particle in unit of unit charge e.

2.2 Detector System

2.2.1 Inner and Outer Detector

The SK detector is divided into two regions: inner detector (ID) and outer detector (OD). The two parts are optically isolated and have a boundary of stainless steel support frame structure, which is about 2.2 m from the wall. Over 11,000 50 cm PMTs facing inward and 1,885 20 cm PMTs facing outward are mounted on the steel structure. Opaque black sheets are placed in gaps between ID PMTs to isolate ID and OD optically.

Inside the support structure is the 32 kt ID, where particles are reconstructed. The

reconstruction is achieved using the Cherenkov pattern projected on the ID PMTs and the charge and time information collected by PMTs. The ID PMT is Hamamatsu R3600 50 cm PMT, and the schematic is shown in Figure 2.2. The photocathode is Bialkali glass (Sb-K-Cs), which is sensitive to 300 nm to 600 nm wavelength photons. The quantum efficiency versus photon wavelength is shown in Figure 2.3. PMT response is dependent on photon incident angle and is measured by calibrations. An acrylic case was installed around the PMT to prevent chain reaction implosion by reducing the flow rate of water entering PMT.

The 18 kt cylindrical volume between the support structure and the tank wall defines

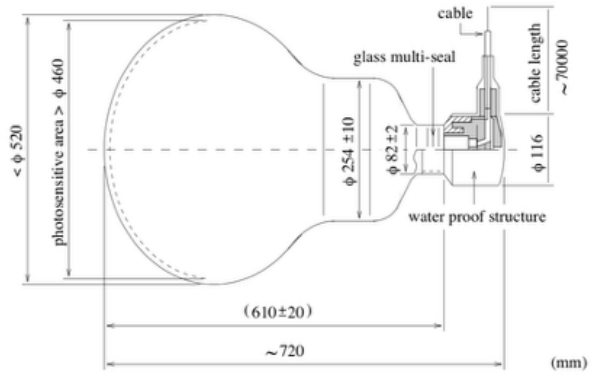

Figure 2.2: Schematic diagram of SK ID 50 cm PMT. Taken from Ref.[11].

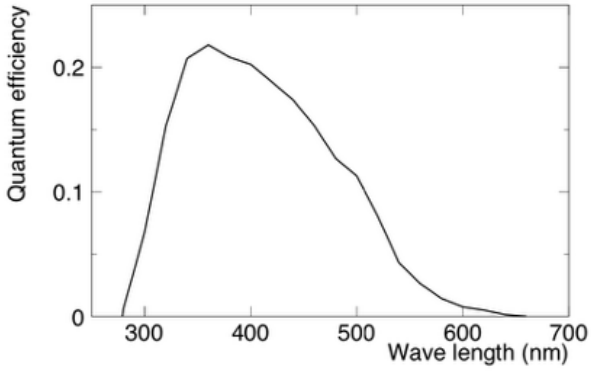

Figure 2.3: Quantum efficiency as a function of wave length for SK 50 cm PMT. Taken from Ref.[11].

the OD. OD is used to reject cosmic ray muons or identify muons generated from neutrinos interacting with water in OD or rock near tank. When muons entering the ID from outside, the emit light in the OD. Refractive white Tyvek sheets covers the wall, and wavelength shifting plate is place on the PMTs to enhance photon detection. Additionally the OD barrel region is optically isolated from the top and bottom region by Tyvek after SK-II.

2.2.2 Water System

The purity of the ultra-pure water used by SK is maintained by the water system, which continuously circulates and purifies the water. Radioactive matter like Radon that emits radiation and become noise background, and those reduce the transparency are removed during purification. 30 to 60 t of water per hour is circulated to water purification system and processed, and all water in tank is fully circulated approximately every month.

The water first goes though a 1 μm filter to remove large particles. Then a heat exchanger cools down the water to 13°C to maintain uniform PMT noise and inhibit bacterial growth. Next water passes ion exchanger to remove heavy molecule and ion, after which the UV sterilizer is used to kill renaming bacteria. Then the Radon-less air is dissolved in the water and water passage through a vacuum degasifier to remove dissolved oxygen and Radon. Finally an ultra filter and a membrane degasifier are used to further remove small particles and reduce Radon. After purification, the resistivity of water increased to 18 MΩ·cm, particulates smaller than 0.2 μm are reduced to 6 cm^{-3}, and Radon concentration reduced to 0.4 mBq m^{-3}.

2.2.3 Data Acquisition System

The SK data acquisition (DAQ) system captures signals from each PMT and triggers data record. There have been two generations of DAQ systems used by SK. The first one is the Analog-Timing-Module (ATM) used from SK-I to SK-III. From SK-IV, the DAQ system is upgraded to QTC-Based Electronics with Ethernet (QBEE). Figure **??** shows the schematic of the QBEE DAQ system for ID PMT. The QTC (charge-to-time converter) read the signal and convert it to a rectangular pulse. The time and integrated charge information is encoded in the leading-edge time and time width of the pulse. If the amplitude of the signal exceeds 0.25 photoelectrons, the process will initiate. The QBEE has three gain stages with the ratio set to $1 : 1/7 : 1/49$, and allowing a maximum 2500 pC charge to be recorded. Output pulse of QTC is then digitized by time-to-didital converter (TDC). The digitized time and charge information is later processed by field programmable gate arrays (FPGA) and applied with software trigger to be constructed as event. Triggers include Super High Energy (SHE) trigger, High Energy (HE) trigger, Low Energy (LE) trigger and Super Low Energy (SLE) trigger. Table 2.2 summarized the threshold (in terms of number of PMT hits within a sliding 200 ns time window) and event window of each type. Finally triggered events are stored on dedicated computers in the format of CERN ZEBRA and ROOT.

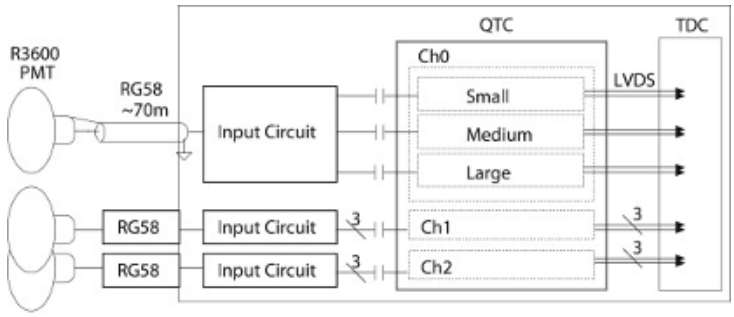

Figure 2.4: Schematic diagram of ID ATM DAQ system. Taken from Ref.[35]

Table 2.2: Summary of trigger threshold and event window for four types of triggers.

Type	Threshold (nhits in 200 ns)	Event Window [μs]
SHE	70→58	[-5,35]
HE	50	[-5,35]
LE	47	[-5,35]
SLE	34→31	[-0.5,1.0]

Chapter 3

Atmosphere Neutrino Simulation

As this analysis searches for astrophysical neutrinos, which only differs from atmosphere in spectrum, the atmosphere neutrino simulation in SK is adapted. This chapter introduces the Monte Carlo (MC) simulation for atmosphere neutrinos. Astrophysical neutrino MC is discussed in Section 5.3.1.

3.1 Atmospheric Neutrino Flux

Atmosphere neutrinos are the major backgrounds in the searches for high-energy astrophysical neutrinos. Atmosphere neutrinos are produced by interactions between cosmic rays discussed in Section 1.2 with atmosphere nuclei. The flux model used in the SK atmosphere neutrino simulation is the Honda-Kajita-Kasahara-Midorikawa (HKKM) model[18]. The model is based on measurements of AMS[2] (satellite) and BESS[15] (high-altitude balloon). Atmosphere density uses the US-standard atmosphere '76 model. PHITS [34] and DPMJET-III[40] are adopted for simulations of hadronic interactions (including genration of mesons and leptons) above and below 32 GeV, respectively. Figure 3.1 shows the atmosphere spectrum predicted by HKKM 2011 model and measured by detectors including SK.

Solar activity also affects the neutrino flux as solar wind disperse low-energy cosmic rays and reduce energy of high-energy cosmic rays pass through it[39]. The solar activity fluctuates periodically every 11 years. To account for this difference, three levels of solar activity, minimum, middle and maximum are calculated in the model. SK generates the atmosphere neutrinos with the solar middle activity, and assign a weight to every event by the fraction of time spent in minimum and maximum solar activity for that SK phase. The sunspot number and neutron monitor counts, shown in Figure 3.2, are used to calculate the fraction.

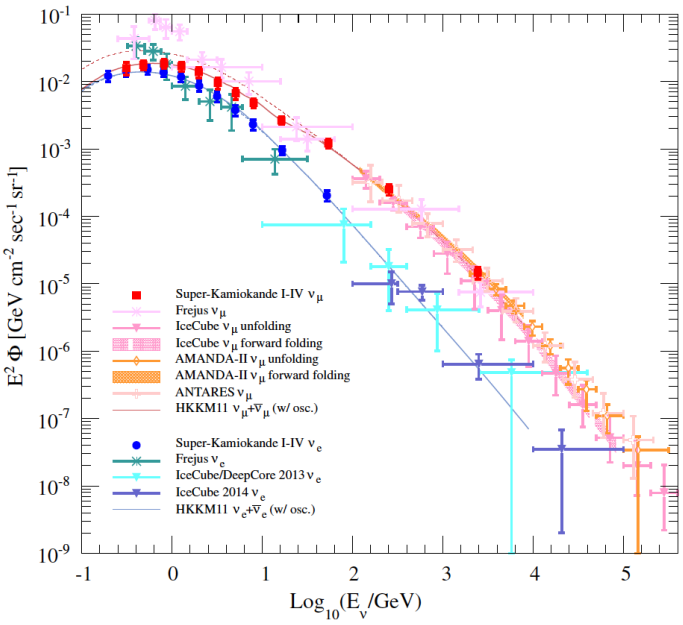

Figure 3.1: Atmospheric neutrino flux predicted by HKKM 2011 model (pink and blue solid lines) and measured by SK and other detectors. Taken from Ref.[46]

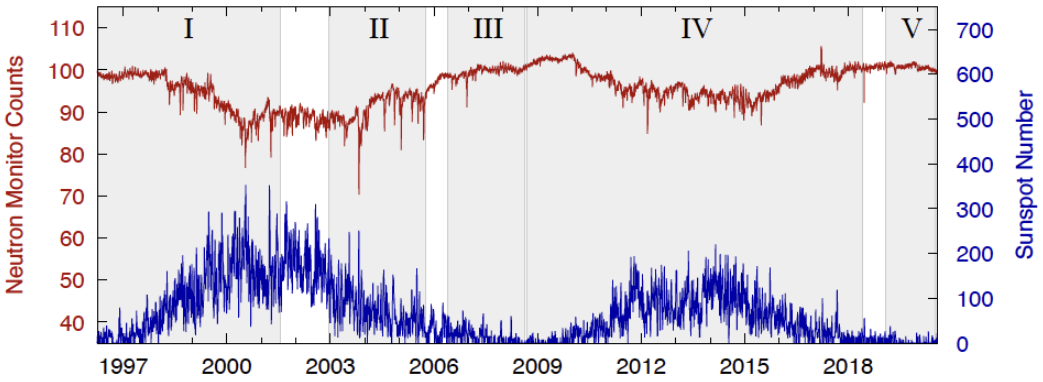

Figure 3.2: Neutron monitor counts (left side y-axis and red line) and sunspot numbers (right side y-axis and blue line) in SK-I to SK-V phases (gray shaded region). Taken from Ref.[50].

The neutrino oscillation is not taken into account in the simulation stage. Instead, an oscillation weight is calculated for each event based on its energy, direction and flavor, using oscillation parameters obtained from Ref.[45].

3.2 Neutrino Interaction

Neutrino interactions with target in the water can be categorized in two ways. Depending on the propagators of the interactions, they are classified as charged current (CC) interactions, mediated by $W^{\pm}$, and neutral current (NC) interactions in which Z^0 is exchanged. Interactions can be classified as quasi-elastic (QE) scattering, single pion production and deep inelastic scattering (DIS), based on the particles produced in the final states. Such neutrino interactions are simulated with `NEUT` in SK.

3.2.1 Quasi-Elastic Scattering

In quasi-elastic scattering, the neutrino interact with a nucleon and produce an outgoing lepton/neutrino and ejected nucleon in CC/NC interaction:

$$\begin{aligned} \text{CC} &: \nu + N \rightarrow N' + l \\ \text{NC} &: \nu + N \rightarrow N + \nu \end{aligned} \tag{3.1}$$

where ν is neutrino, l is lepton and N and N' are nucleon. The Feynman diagram for CCQE interaction is shown in Figure 3.3

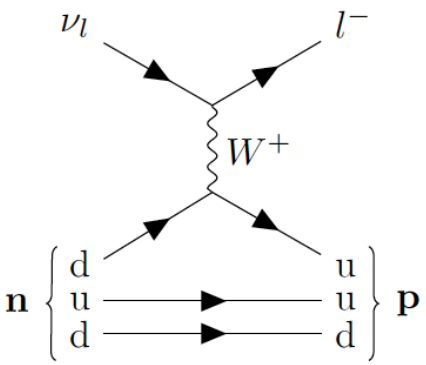

Figure 3.3: Feynman diagram of neutrino scattering with neutron producing proton and lepton via CCQE. Taken from Ref.[50].

Relativistic Fermi gas (RFG) and local Fermi gas (LFG) models are implemented by NEUT for the nucleon bounded in a nuclear (Oxygen for example). In the case two nucleon are strongly-correlated, two nucleon can be knocked off, which is called two-particle two-hole (2p2h). The estimated fraction of 2p2h in QE can be approximately 20%[13].

3.2.2 Single Pion Production

As neutrino energy goes up, a single pion can be produced together with the outgoing lepton or neutrino and ejected nuclei:

$$\begin{aligned} &\text{CC}: \nu + N \rightarrow l + N + \pi^{\pm} \\ &\text{CC}: \nu + N \rightarrow l + N' + \pi^{0} \\ &\text{NC}: \nu + N \rightarrow \nu + N + \pi^{0} \\ &\text{NC}: \nu + N \rightarrow \nu + N' + \pi^{\pm} \end{aligned} \tag{3.2}$$

The processes are mediated by Δ-baryons. Figure 3.4 shows the Feynman diagram of a CC interaction producing a charged pion.

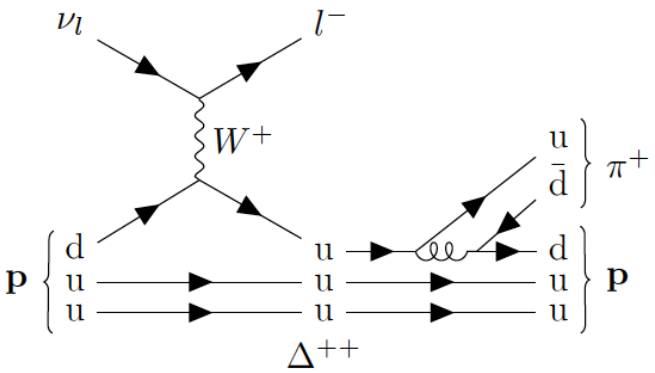

Figure 3.4: Feynman diagram of neutrino scattering with proton producing outgoing proton, lepton and charged pion via CC single pion interaction intermediated by Δ^{++} resonance. Taken from Ref.[50]

18 baryon resonances states up to W <2 GeV are considered by NEUT, and resonant production for other mesons like K and η are taken into account in simulation. The coherent pion production, in which neutrino interact with the whole nucleus (for example Oxygen) and produce a single pion, is also simulated by `NEUT`.

3.2.3 Deep Inelastic Scattering

DIS is the dominant interaction channel in the energy range above approximately 5 GeV, which is also the energy range for high-energy astrophysical neutrino search mainly looks into. In this process, multiple pions or even heavier mesons are produced after scattering in both CC and NC channel.

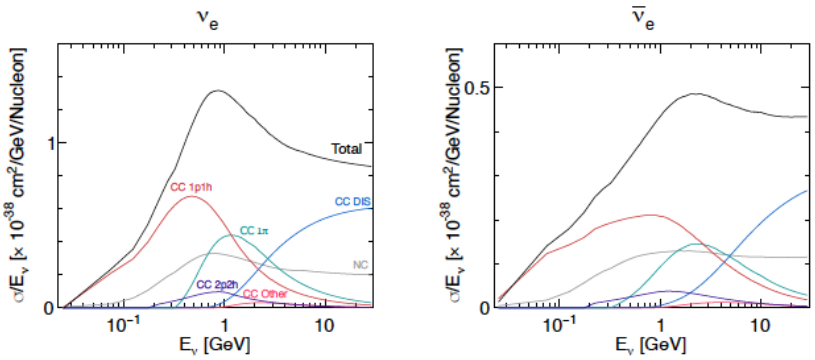

Figure 3.5: Differential cross section for water target of each neutrino interaction channel versus neutrino energy used by NEUT. Taken from Refl.[53].

$$\frac{d^2\sigma}{dxdy} = \frac{G_F^2 ME}{\pi}\left[\left(1-y+\frac{y^2}{2}+C_1\right)F_2(x) \pm y\left(1-\frac{y}{2}+C_2\right)xF_3(x)\right] \tag{3.3}$$

$$C_1 = \frac{m^2(y-2)}{4MEx} - \frac{Mxy}{2E} - \frac{m^2}{4E^2} \tag{3.4}$$

$$C_2 = -\frac{m^2}{4MEx}$$

where $x = -q^2/(2M\Delta E)$ and $y = \Delta E/E$, with ΔE being the energy difference between incoming neutrino and outgoing lepton, and M is the nucleon mass, m is the outgoing lepton mass and E is the incoming neutrino energy. F_2 and F_3 are parton distribution function.

Figure 3.5 summarized the ν-^{12}C cross section for each interaction channel as a function of neutrino energy used by `NEUT`.

3.3 Detector Simulation

The primary outgoing particles produced in the neutrino interactions discussed above are then put into a `GEANT3` based SK detector simulator called `SKDETSIM`. In the simulator, the propagation, decay, scatter, capture and other interactions of primary particles and corresponding secondary particles are simulated. The scattering, reflection and absorption of photons emitted from Cherenkov radiation, together with the PMT response are also simulated.

Chapter 4

Data

SK detector receives triggers with a frequency of several tens of Hz and record about 10^6 events per day. For HE and SHE trigger discussed in Chapter 2, most of the triggered events are cosmic muons and low-energy radioactive backgrounds. These backgrounds need to be removed before performing event reconstructions, otherwise will waste huge amount of computing resources. Atmosphere neutrinos in SK are categorized as three samples:

- Fully contained (FC)
  The interaction vertex is inside ID and all visible outgoing particles are contained in the ID.
- Partially contained (PC)
  The interaction vertex is inside ID as well, but some visible outgoing particles reached OD.
- Upward-going muon (UPMU)
  Muons come below horizon, produced by neutrino interacting with rock near SK tank or water in OD region. UPMU are further classified as stopping muons and through-going muons depending on whether muon leaves ID before energy drops below Cherenkov threshold.

Figure 4.1 shows a schematic of the topologies of the three samples. All three samples will be used in this analysis.

4.1 Reduction

The SK reduction includes sequences of procedure. In this section an overview of the reduction for the three sample is presented. Details can be found in Ref.[28].

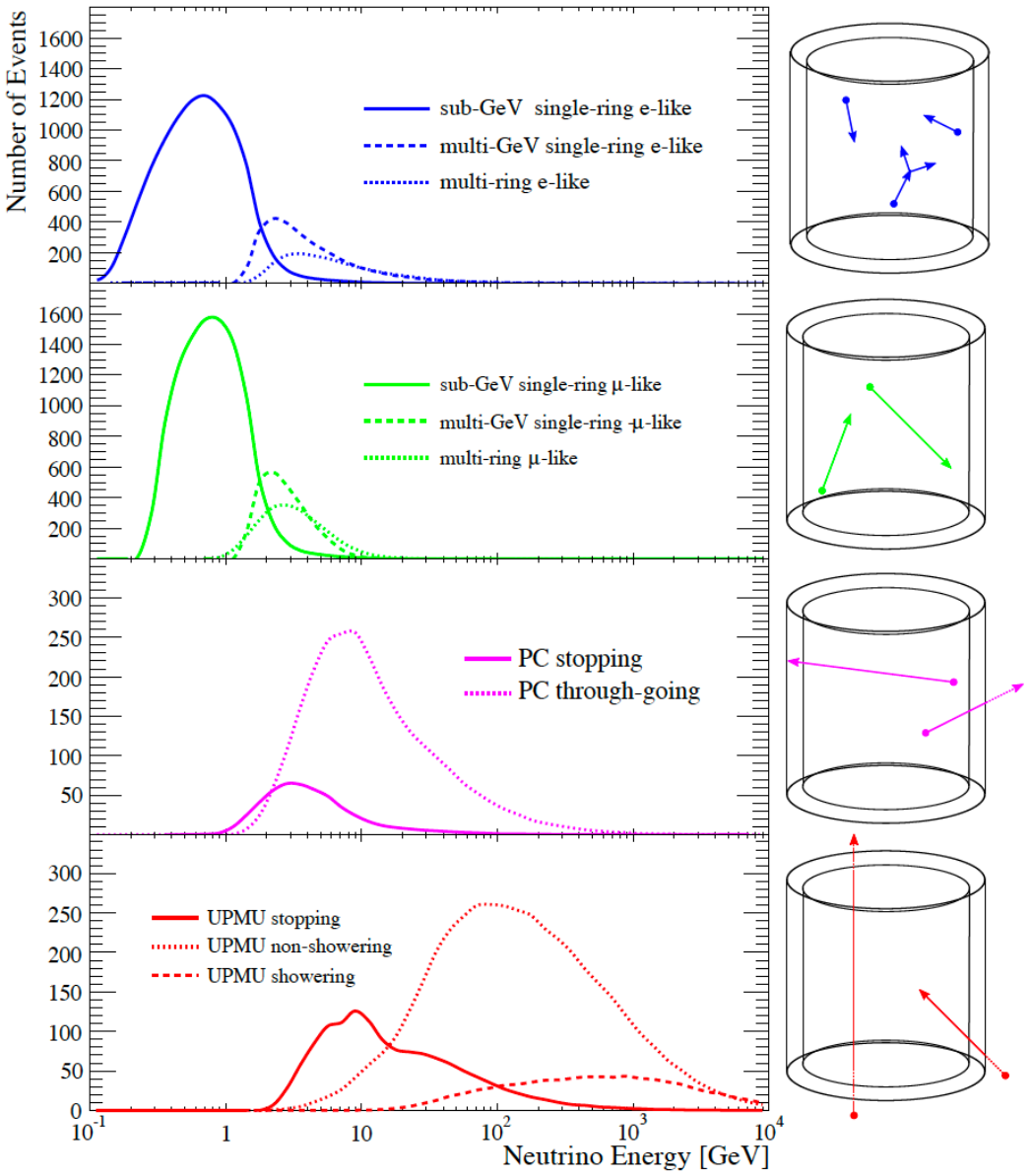

Figure 4.1: Atmosphere neutrino event topologies of three samples and their neutrino energy distribution. Taken from [28].

4.1.1 FC Reduction

FC1

FC1 removes low-energy energy triggers including radioactive backgrounds and cosmic muons. The following cuts are applied:

1. $PE_{300} > 200$ p.e.s (100 p.e.s for SK-II)
   PE_{300} is the total charge observed by ID PMTs within 300 ns sliding window.

2. $NHITA_{800} \leq 55$ (50 for SK-I to SK-III) or OD trigger is not triggered
   $NHITA_{800}$ is the number of hit OD PMTs in the 800 ns time window (-300 ns to +500 ns).

Event rate reduced to ~3500 per day after FC1.

FC2

In FC2 the following cuts are applied

1. $NHITA_{800} \leq 30$ (25 for SK-I to SK-III) or $PE_{total} > 100,000$ p.e.s (500,000 p.e.s for SK-II) or OD trigger is not triggered

2. $PE_{max}/PE_{300} < 0.5$
   PE_{max} is maximum charge observed by a single ID PMT among all hit PMTs.

The first cut removes cosmic ray muons while the second removes low energy events and noises. Distribution of $NHITA_{800}$ and PE_{max}/PE_{300} for SK-IV data and MC are shown in Figure 4.2 and Figure 4.3, respectively.
Event rate reduced to ~900 per day after FC2.

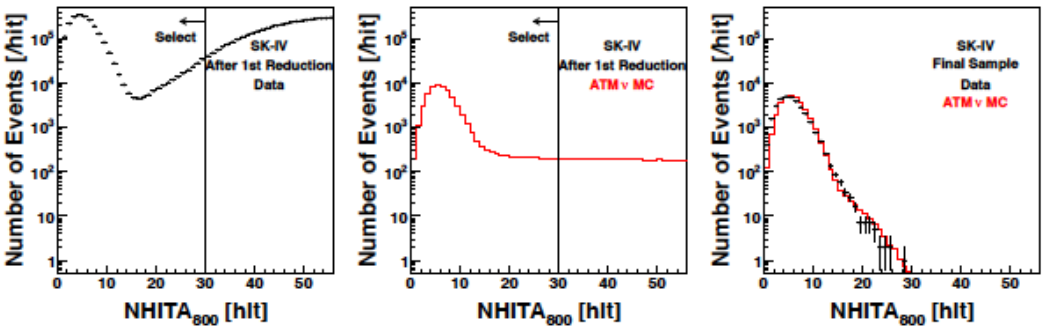

Figure 4.2: $NHITA_{800}$ distribution for SK-IV data (left) and MC (center) before FC2 reduction, and data and MC after reduction (right). Taken from Ref.[48].

FC3

FC3 includes several sub reduction criterion.

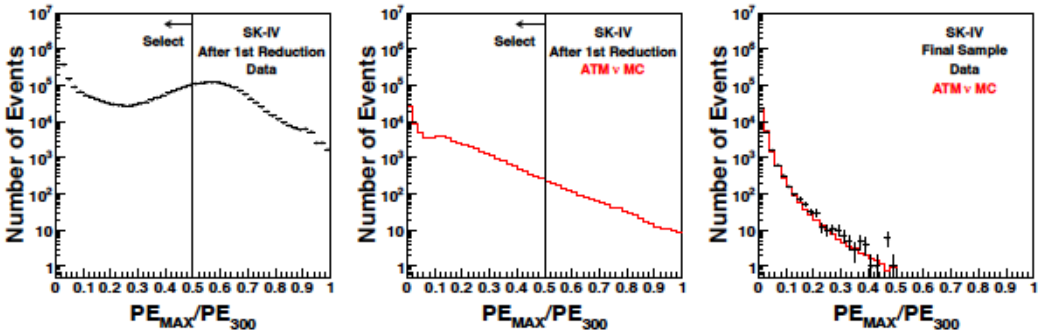

Figure 4.3: PE_{max}/PE_{300} distribution for SK-IV data (left) and MC (center) before FC2 reduction, and data and MC after reduction (right). Taken from Ref.[48].

Through-going Muon Rejection

Cosmic ray muons passing through and exiting the detector are removed by the following step. First a fitter to find the entry and exit of muon is applied to all events with number of ID PMT observed charge over 230 p.e.s exceeding 1000

$$goodness = \frac{1}{\sum_i \frac{1}{\sigma_i}} \times \sum_i \frac{1}{\sigma_i^2} \exp\left[-\frac{(t_i' - t_0)^2}{2(1.5\sigma_i)^2}\right] \tag{4.1}$$

where t_i' is the hit time of i^{th} PMT, σ_i is time resolution of i^{th} PMT, and t_0 is fitted to maximize *goodness*. Then events satisfying the following criteria are removed:

1. $goodness > 0.75$
2. $\text{NHITA}_{in} > 10$ or $\text{NHITA}_{out} > 10$
   $\text{NHITA}_{in}(\text{NHITA}_{out})$ is the number of OD hit within 8 m from the entrance (exit) point in 800 ns time window.

NHITA_{in} and NHITA_{out} distribution for SK-IV data and MC are shown in Figure 4.4.

Stoping Muon Rejection

Cosmic ray muons entering and stopping in the detector are removed by first fitting Function 4.1 and obtaining goodness. Then events satisfying the following criteria are removed:

1. $goodness > 0$ (0.5 for SK-I)
2. $\text{NHITA}_{in} > 10$ (5 for Sk-I)

NHITA_{in} distribution for SK-IV data and MC is shown in Figure 4.5.

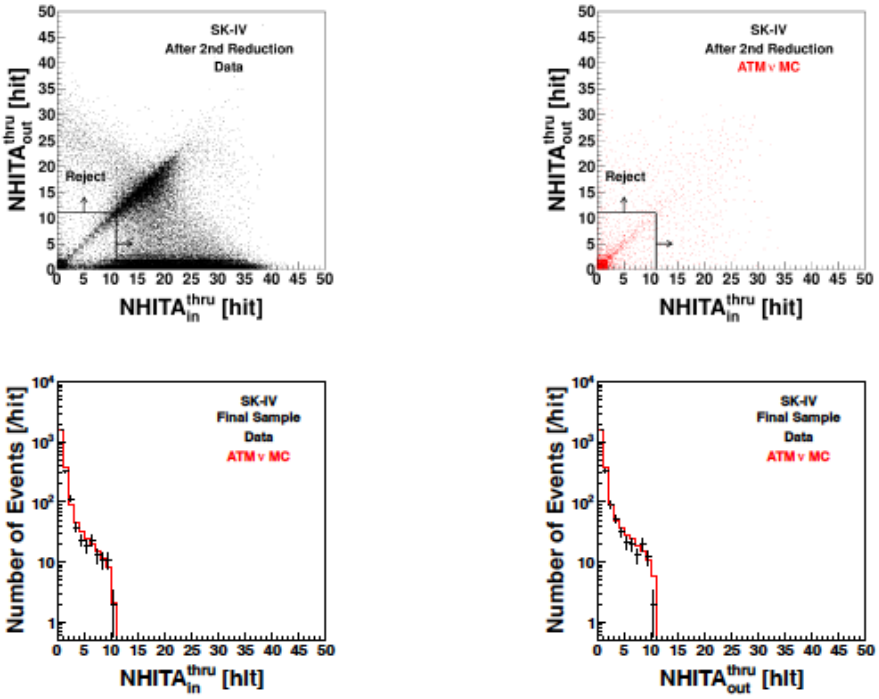

Figure 4.4: 2-dimensional NHITA$_{in}$ and NHITA$_{out}$ distribution for SK-IV data (top left) and simulation (top right) before through-going muon rejection, and NHITA$_{in}$ (bottom left) and NHITA$_{out}$ (bottom right) after rejection (bottom). Taken from Ref.[48].

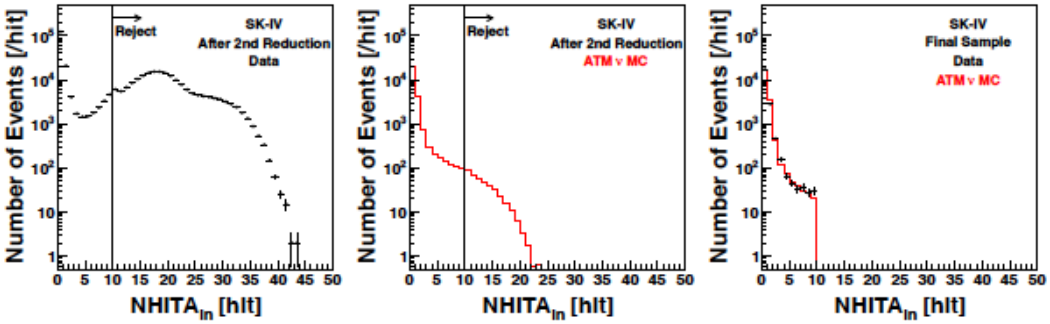

Figure 4.5: NHITA$_{in}$ distribution for SK-IV data (left) and MC (center) before stopping muon rejection, and data and MC after rejection (right). Taken from Ref.[48].

Cable Hole Muon Rejection

There are 12 holes on top of SK tank for signal and high voltage supply cables. To identify cosmic ray muons that may pass through the holes, 4 of them have plastic scintillator plate made veto counters installed. Then cosmic ray muons are rejected by cutting on scintillator paddle activity.

Flasher Event Rejection

The minimum number of ID hits in a 100 ns sliding window scans from +300 ns to +800 ns (NHIT_{min100}) is used to reject the flasher events that in general have a broader time distribution compared to signals.

- $\mathrm{NHIT}_{min100} \geq 15$ or $\mathrm{NHIT}_{min100} \geq 10$ and ID PMT hit less than 800 for SK-I
- $\mathrm{NHIT}_{min100} \geq 20$ from SK-II

Distribution of NHIT_{min100} for SK-IV data and MC are shown in Figure 4.6.

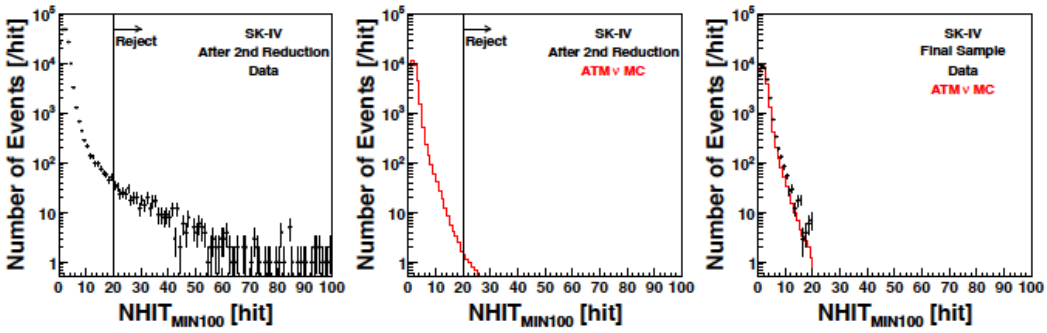

Figure 4.6: NHIT_{min100} distribution for SK-IV data (left) and simulation (middle) before flasher event rejection, and data and MC after reduction (bottom). Taken from Ref.[48].

Low Energy Event Rejection

Multiple coincident low-energy backgrounds are removed according to vertex information reconstructed by low-energy event fitter with the following criteria:

1. ID hit is smaller than 500
2. $\mathrm{N}_{50} \leq 50$ (25 for SK-II)
   N_{50} is ID hit in a 50 ns sliding time window after subtracting time of flight of each observed photon. The vertex is fitted so that the time residual is maximized.

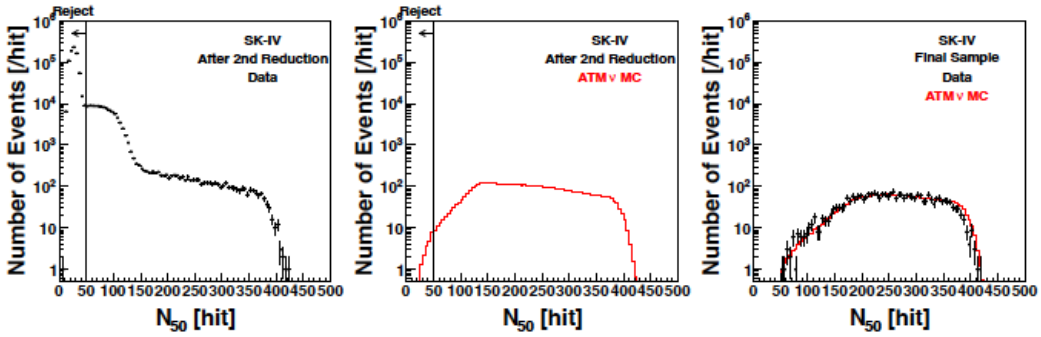

Figure 4.7: NHIT_{50} distribution for SK-IV data (left) and simulation (middle) before flasher event rejection, and data and MC after reduction (bottom). Taken from Ref.[48].

The distribution of N_{50} for SK-IV data and MC are shown in Figure 4.7.

Additionally cosmic muon entered ID after low energy activity without triggering OD activity are also removed in FC3. Event rate reduced to ~80 per day after FC3.

FC4

Flasher events are further removed by pattern-matching methods with data driven cut. In SK-I and SK-II, a single parameter (correlation coefficient) is used for reduction. From SK-III, a new parameter called *prob*, which combines the correlation coefficient with the result of Kolmogorov-Smirnov test is used instead (check Ref.[48] for more details). The distribution of *prob* for SK-IV data and MC are shown in Figure **??**.

A few events per day are rejected by FC4.

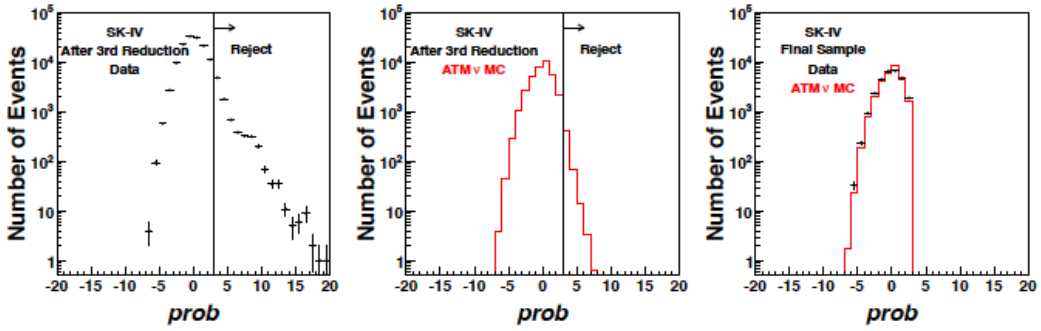

Figure 4.8: Variable *prob* distribution for SK-IV data (left) and simulation (middle) before flasher event rejection, and data and MC after reduction (bottom). Taken from Ref.[48].

FC5

Finally the following quality cut are applied to remove remaining backgrounds.

- Invisible muon cut, which rejects muon below Cherenkov threshold entering ID and produce a decay electron emitting Cherenkov radiation.
- Accident coincident event cut, which rejects remaining coincidence event from FC3 using more sophisticated criteria.
- Flasher event cut, which rejects remaining flasher events using vertex reconstruction.
- Cable hole muon cut, which rejects events with any coincidence with veto counter.
- Stopping muon cut, which rejects remaining muons using vertex reconstruction.

The final FC event rate after all FC cuts is ~10 per day. Final selection efficiency for neutrino events is above 99%, with total non-neutrino contamination smaller than 1%.

4.1.2 PC Reduction

PC1

PC1 ensures event does not have OD activity in two OD hit clusters, and muon event must have enough energy deposited in ID to be able to penetrate fiducial volume (FV).

PC2

PC2 uses clustering algorithm to search for region with more than 10 OD hits. Events are rejected if algorithm fail to find one. PC2 also reject events based on number of end-cap hits versus number of barrel hits.

PC3

PC3 removes flasher events similar to FC3 by cutting on ID hits after primary trigger.

PC4

PC4 uses fitter called muboy to reject events with improbable vertices.

PC5

PC5 sets optional conditions for through-going muon, stopping muon, cable whole muon and clipper corner muon, and a condition that at least 1 decay electron must exist. Event fails more than one optional condition will be rejected.
The final PC event rate after all PC cuts is ~0.6 per day.

4.1.3 UPMU Reduction

First Reduction

This reduction cut requires muon momentum must be larger than 1 GeV/c.

Second Reduction

In this step events are reconstructed with seven fitters. Events are rejected or accepted according to fitted direction if goodness of one fitter exceed threshold.
More details can be found in Ref.[24]

Third Reduction

Events are reconstructed by a fitter called precisefit. Downward-going muons are rejected. Stopping muons with fitted momentum (called p_{Fit}) above 1.6 and through-going muons with fitted track length (called l_{Fit}) above 700 cm are accepted.

Fourth Reduction

The fourth reduction implements the clustering algorithm used in PC2 and rejects events with zero or more than one OD hit clusters.

Fifth Reduction

Events are checked manually by experts in fifth reduction.
The final UPMU event rate is ~1.5 per day.

4.2 Reconstruction

The information of the charged particles above Cherenkov threshold produced in neutrino interaction, such as energy, direction, and interaction vertex, is reflected to the Cherenkov rings, which are further recorded in the charge and time information on ID PMTs within trigger time window. A set of algorithms called APFit is utilized by SK to reconstruct the Cherenkov rings and extract information of neutrino interaction. Here in this section the brief overview of APFit is presented, and detailed documentation can be found in Ref.[41].

4.2.1 Vertex Reconstruction

Event reconstruction starts with the reconstruction of the vertex. The vertex position $\vec{x}$ is fitted to maximize the goodness of fit parameter G given by

$$G(\vec{x}) = \sum_i \frac{1}{\sigma_i} \exp\left\{-\frac{(t_i - n/c|\vec{x} - \vec{x}_i^{PMT}| - t_0)^2}{2(1.5\sigma_i)^2}\right\} \tag{4.2}$$

where σ_i is the time resolution(which is related to the charge q_i), t_i is the hit time and $\vec{x}_i^{PMT}$ is the position of the i^{th} PMT, and t_0 is the assumed generation time of the signal. Assuming the photons are emitted from 1 ring, the ring direction $\vec{d}$ can be defined by

$$\vec{d} = \sum_i q_i^{corr} \frac{\vec{x}_i^{PMT} - \vec{x}}{|\vec{x}_i^{PMT} - \vec{x}|} \tag{4.3}$$

with q_i^{corr} being corrected charge of i^{th} PMT

$$q_i^{corr}(\vec{x}) = q_i \exp\left[-\frac{|\vec{x} - \vec{x}_i^{PMT}|}{L} \frac{\cos(\theta(\vec{x}))}{f(\theta)}\right] \tag{4.4}$$

where L is the water attenuation length, and $\theta(\vec{x})$ is the incident angle of photon originates from $\vec{x}$ on the hit PMT. $f(\theta)$ is the PMT acceptance at incident angle θ. The the ring direction $\vec{d}$ and ring opening angle (which is also the opening angle to the edge of the ring pattern) θ_{egde} can be better fitted by the new goodness of fit parameter given by

$$G(\vec{d}, \theta_c) = \frac{1}{\sin\theta_{edge}} \cdot \exp\left[-\frac{(\theta_{edge} - \theta_{exp})^2}{2\sigma_\theta^2}\right] \cdot \left(\left.\frac{dq^{corr}(\theta)}{d\theta}\right|_{\theta=\theta_{edge}}\right)^2 \cdot \int_0^{\theta_{edge}} q^{corr}(\theta) d\theta \tag{4.5}$$

where $q^{corr}(\theta) = \sum_{i,\theta_i=\theta} q_i^{corr}$ is the corrected charge distribution as a function of opening angle θ from $\vec{d}$. θ_{exp} is the expected Cherenkov angle, either set to 42°, or angle given by Equation 2.2 with energy corresponding the the observed charge from Equation 2.2, assuming muon or electron. σ_θ is the angular resolution of expected θ_{edge}. Figure 4.9 shows the distribution of charge and its second derivative with respect to θ as function of θ. θ_{edge} is determined by the point that second derivative equals to 0 and is negative below and positive above this value.

4.2.2 Ring Counting

The Hough transformation method[19] is used for ring counting in APFit, in which the ring candidates are searched for as illustrated in Figure 4.10. Each hit PMT is treated as the center of a virtual Cherenkov ring with the assumed Cherenkov angle. The virtual

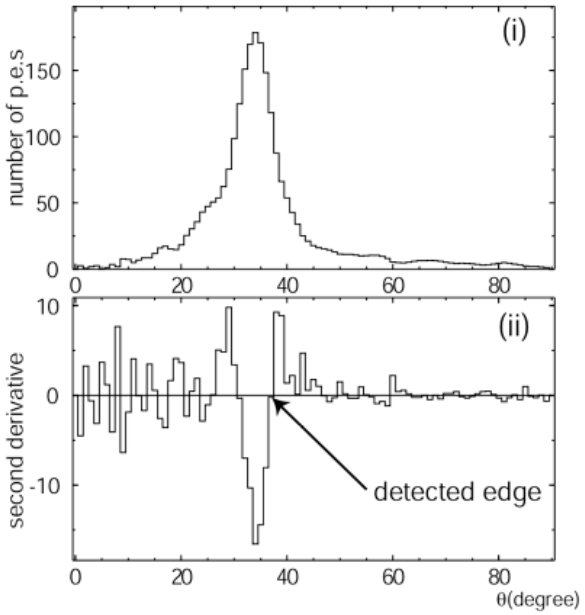

Figure 4.9: Corrected charge as a function of opening angle (top) and its second derivative (bottom). Taken from Ref.[41]

rings overlap with each other, and ideally all circles will overlap at the true ring direction. The expected charges for each PMT assuming $\vec{d}$ and θ_c can be implemented as the weight to each virtual ring. The weight at a position is the sum of the ring weights, and the candidates of the ring directions are chosen to be the positions of the peaks. In reality in Hough transformation, altitude and azimuth of PMT are used instead of 3D Cartesian coordinate (as PMTs are installed on the cylindrical frame and only has two-degree of freedom in position).

Rings are counted iteratively. When testing the n^{th} ring in the ring candidates, corrected PMT charges from $n-1$ rings are subtracted. Likelihood of the hypothesis to have the $N_{ring}+1^{th}$ ring with N_{ring} rings being already identified is given by

$$L(N_{ring}) = \sum_{i,\theta_{i,j}<1.2\theta_{c,j}}^{N_{PMT}} \log\left[P\left(q_i, \sum_j^{N_{ring}} \alpha_j q_{i,j}^{exp}\right)\right] \tag{4.6}$$

where $q_{i,j}^{exp}$ is the expected charge to be observed by i^{th} PMT from the j^{th} ring. PMTs in the cone with opening angle of $1.2\theta_c$ are taken into account. $P(q^{obs}, q^{exp})$ is the probability of observing charge q^{obs} given expected charge q^{exp} with Poisson (for small $q_{i,j}^{exp}$) or Gaussian (for large $q_{i,j}^{exp}$) distribution. α_j is the weight of ring j, and is optimized for every hypothesis of N_{ring}. The likelihood $L(N_{ring})$ is compared to $L(N_{ring}-1)$, and the hypothesis of having $N_{ring}+1$ will be rejected if $L(N_{ring}-1) > L(N_{ring})$. At least one ring has to be fitted. Distribution of $L(N_{ring}=2) - L(N_{ring}=1)$ for SK-IV and SK-V

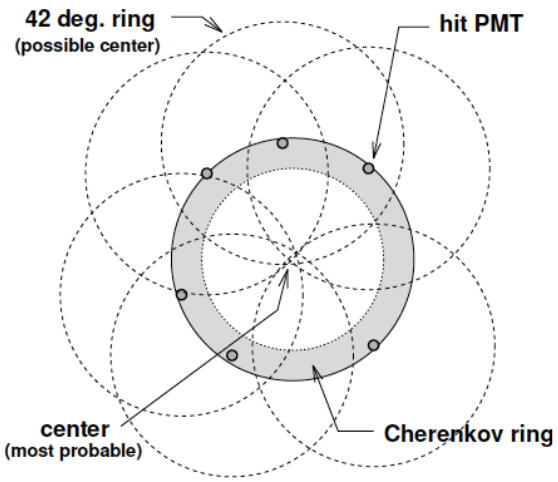

Figure 4.10: Illustration of how Hough transformation works. Big solid circle with shade is the real Cherenkov ring. Circles on the solid ring are the hit PMTs. Dashed circles are virtual ring centered at each PMT. Most probable position of the Cherenkov ring is pointed out. Taken from Ref.[28].

atmospheric neutrino data and simulation are shown in Figure 4.11.

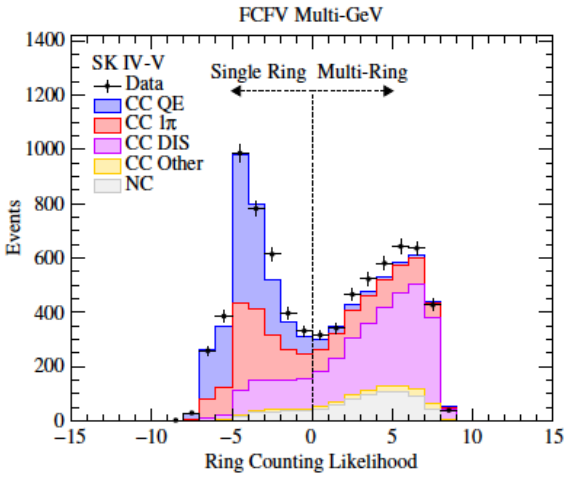

Figure 4.11: Ring counting likelihood of the hypothesis that at least two ring exist over single-ring hypothesis ($L(N_{ring} = 2) - L(N_{ring} = 1)$). Taken from Ref.[53].

4.2.3 Particle Identification

APFit classify rings as e-like or μ-like, depending on whether electromagnetic shower occurs or not. When bremstrahlung or Compton are dominant to ionization in Cherenkov radiation, high-energy gamma rays are generated and electron is deflected. The gamma rays then produce electrons and positrons via pair production. These electrons can undergo Cherenkov radiation as well, making the ring fuzzier. Electron is lighter than muon, thus bremstrahlung or Compton become dominant to ionization at lower energy. Ener-

getic photons, from π^0 decay for example, will also have e-like patterns, while patterns of charged pions are μ-like. Figure 4.12 shows the event displays of e-like and μ-like rings.

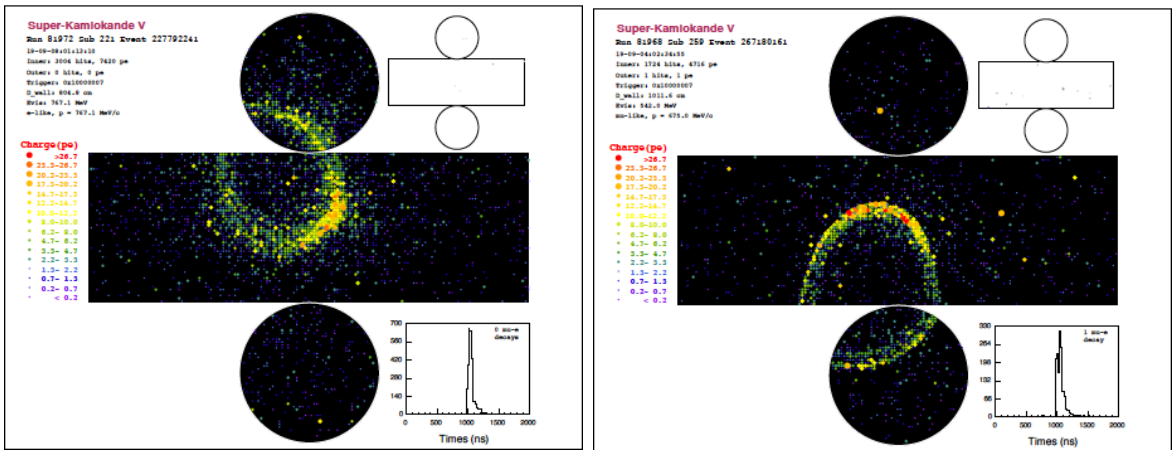

Figure 4.12: Event display of e-like (left) and μ-like (right) neutrino candidate from SK-V. Taken from Ref.[53].

Likelihood for the pattern of k^{th} ring to be l-like (l is e or μ) is given by

$$L_k^{pattern}(l) = \prod_{\theta_i<1.5\theta_c}^{N_{PMT}} P\left(q_i, q_{i,k}^{exp}(l) + \sum_{j\neq k} q_{i,j}^{exp}\right) \tag{4.7}$$

where $q_{i,k}^{exp}$ is the expected charge to be observed by i^{th} PMT from the k^{th} ring assuming k^{th} ring is e- or μ-like. PMTs in the cone with opening angle of $1.5\theta_c$ are taken into account. $P(q^{obs}, q^{exp})$ is defined the same as Equation 4.6. Contributions from other rings are taken into account as well. $q_i^{exp}(l)$ is calculated from simulations measured parameters. Probability of the likelihood following a χ^2 distribution is

$$P_k^{pattern}(l) = \exp\left\{-\frac{[\chi_k^2(l) - \min(\chi_k^2(l=e), \chi_k^2(l=\mu))]^2}{4N_{PMT}}\right\} \tag{4.8}$$

with χ^2 parameter defined as

$$\chi_k^2(l) = -2\log L_k^{pattern}(l) \tag{4.9}$$

For single ring events, the probability of having the observed Cherenkov angle for l-like events at given energy is also taken into account

$$P_k^{angle}(l) = \text{const} \cdot \exp\left[-\frac{(\theta_{\mathrm{c,k}} - \theta_{\mathrm{k}}^{\mathrm{exp}}(\mathrm{l}))^2}{2\sigma_\theta}\right] \tag{4.10}$$

But this value is set to 1 for multi-ring case. Use $P_k(l) = P_k^{pattern} \cdot P_k^{angle}(l)$ to denote the

total probability, the PID likelihood of the k^{th} ring is defined by

$$L_k^{PID} = \sqrt{-\log P_k(l=\mu)} - \sqrt{-\log P_k(l=e)} \tag{4.11}$$

Distribution of L_k^{PID} for SK-IV and SK-V atmospheric neutrino data and simulation are shown in Figure 4.13.

In the searches for high-energy astrophysical neutrinos, an improved event classification

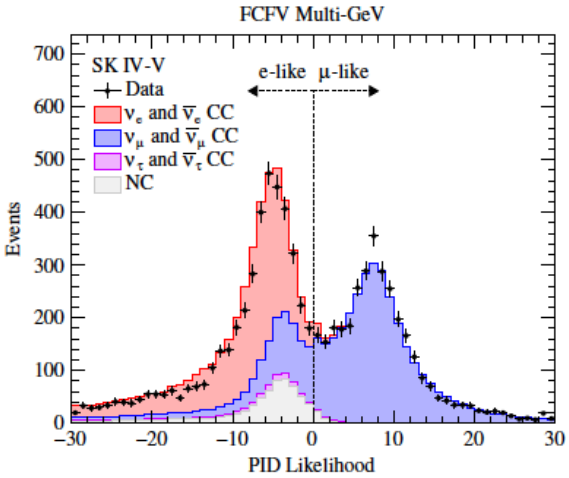

Figure 4.13: Particle identification likelihood of the μ-like hypothesis over e-like hypothesis for the leading ring ($\sqrt{-\log P_1(l=\mu)} - \sqrt{\log P_1(l=e)}$). Taken from Ref.[53].

algorithm is implemented, and is discussed later in Section 5.1.

4.2.4 Momentum Reconstruction

The momentum of the event is reconstructed ring by ring. In order to avoid counting the charge of the PMTs in the ring-overlapping region multiple times, the charge on PMT is distributed to rings. Contribution from each ring on one PMT is calculated by

$$q_{i,k} = q_i \cdot \frac{q_{i,k}^{exp}}{\sum_k q_{i,k}^{exp}} \tag{4.12}$$

where $q_{i,k}^{exp}$ is the same as used in Equation 4.7. The total charge of the k^{th} ring, usually denoted by R_k^{tot}, can be expressed by

$$R_k^{tot} = \frac{G_{MC}}{G_{data}} \left[\sum_{i\in(\theta_{i,k}<70^\circ, -50\text{ns}<t_i^{resi}<250\text{ns})} q_{i,k}^{corr} - \sum_{j\in(\theta_{j,k}<70^\circ)} (q_j^{scat} + q_j^{refl}) \right] \tag{4.13}$$

where $q_{i,k}^{corr}$ is obtained by inserting Equation 4.12 into Equation 4.4, and G_{MC} and G_{data} are PMTs gain factors in simulation and data. q_j^{scat} and q_j^{refl} are expected charge due

to photon scattering and reflection. Mapping between R^{tot} and ring momenta have been tabulated by simulation, and the converted momenta will be used as visible energy E_{vis} in later analysis.

4.3 Global Cut

A set of global cuts are applied after the data reduction and reconstruction procedures before data analysis as follows:

- FC: The number of OD hits must be less than 16 (10 for SK-I) and distance from reconstructed vertex to the nearest detector wall must be greater than 100 cm.
- PC: The number of OD hits must be more than 16 (10 for SK-I) and distance from reconstructed vertex to the nearest detector wall must be greater than 200 cm.
- UPMU: The reconstructed traveling direction of events must be upward, and the reconstructed muon momentum must be larger than 1.6 GeV for stopping muon or the fitted muon track length must be larger than 700 cm for through-going muon.

The cut on the distance from the reconstructed vertex to the nearest wall can reduce poorly reconstructed events. If an event interact too close to the wall, the uncertainty of its reconstructed vertex, direction and momentum will be large, as the number of PMT being light is small. It also reduce non-neutrino background. Figure 4.14 shows the number of non-neutrino backgrounds as a function of distance to wall. The conventional region is that more than 200 cm away from the wall, and is applied to PC events. For FC events, an additional region between 100 cm and 200 cm is expanded from the conventional region, adding 4.7 kt additional volume (about 20%)[47].

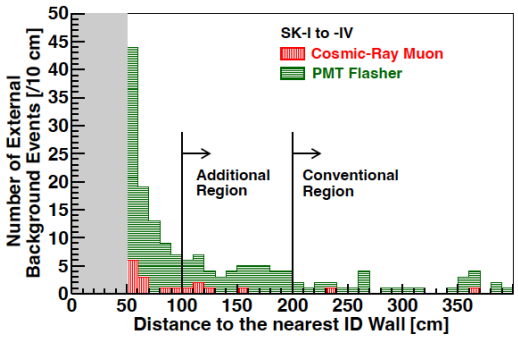

Figure 4.14: Non-neutrino background (cosmic-ray muon and PMT flasher) distribution vs distance to the wall. Taken from Ref.[47].

The cut on the number of OD hits for both FC and PC is to make sure that there is no overlapping between the data set of these two samples. Distributions of the number of OD hits for FC and PC are shown in Figure 4.15.

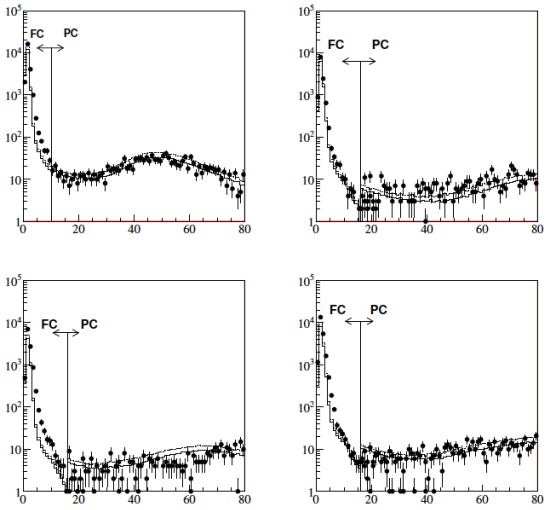

Figure 4.15: Distribution of number of OD hit (NHITAC) for final FC and PC data and simulation of SK-I (top left), SK-II (top right), SK-III (bottom left) and SK-IV (bottom right). Taken from Ref.[28].

The cut for UPMU sample is the same as the requirement for the third UPMU reduction, and the cut is set on the final reconstructed parameters here.

Chapter 5

Astrophysical Neutrino Search Analysis

In this chapter, the analysis methods for searching for high-energy astrophysical neutrinos with high-energy neutrino data from SK-I to SK-V are described. This analysis performs searches for ν_μ and ν_e independently. Searches for ν_μ include full-sky scans for steady and transient point sources without prior source information, as well as a search in the position of known source candidates. In searches for ν_e, search for diffuse neutrino from the galactic plane and stacked search for neutrino from sources inside the galactic plane are performed, together with full-sky scan for the point source and search with point source candidates. The event selection criteria are determined for searches for ν_μ and ν_e and the search algorithms are constructed using the unbinned maximum likelihood method for each search of different sources. Trials (pseudo experiments) using toy MC produced from atmospheric neutrino simulation (Chapter 3) are then run to calculate the sensitivity and later to determine the p-value of the results.

5.1 Analysis Data Sample

As described in Chapter 4, ATMPD sample is further categorized into FC, PC, and UPMU events. All of them contain a considerable fraction of ν_μ events, while most of ν_e events through CC channel fall into FC sample as electron of GeV level dumps most of its kinematic energy within several meters. For this reason, all three samples are used in ν_μ searches and only FC is used for ν_e searches.

Beside the selection cut discussed in Chapter 4, additional energy cuts are introduced to each sample for the following reasons:
1. Angular resolution between the reconstructed event direction and the true neutrino direction will decrease as energy becomes larger. Figure 5.1 shows the plot of 1σ angular resolution vs reconstructed energy. As UPMU is sensitive to energies up to 100 TeV, most of the astrophysical neutrino signals will fall into this category. A 15° search

cone is applied for ν_μ point source search, which corresponds to the angular resolution of UPMU minimum energy events. FC and PC energy cuts are set to 3.5 GeV and 1.0 GeV accordingly so that 90% of signal events stay within 15° search cone.

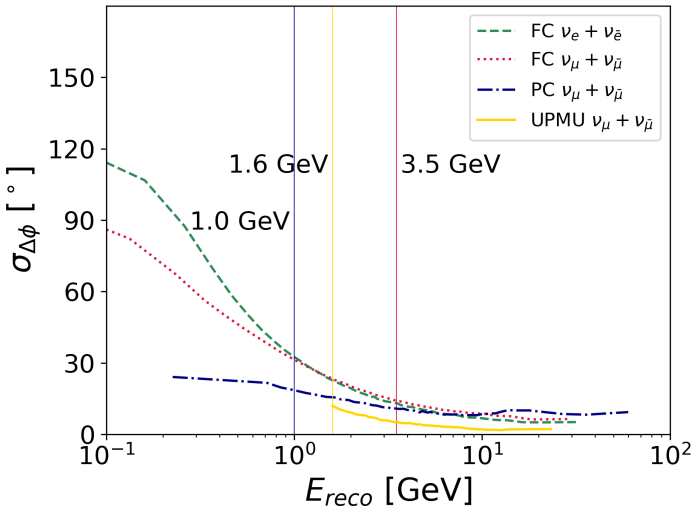

Figure 5.1: 1σ angular resolution between reconstructed event direction and true neutrino direction against reconstructed energy for FC ν_e (green dashed), FC ν_μ (red dotted), PC ν_μ (blue dash-dotted) and UPMU ν_μ (yellow solid). The corresponding energy cut of each sample is indicated by solid vertical line with corresponding color.

2. High-energy astrophysical neutrinos have harder spectrum compared with atmospheric neutrinos, especially for ν_e. As discussed in Chapter 3, the advantage of search for high energy astrophysical ν_e is that it has much fewer background events. From Figure 3.1, atmospheric ν_e flux becomes much smaller than ν_μ flux at 10 GeV, and cut on E_{vis} is set to 10 GeV for FC events used in ν_e search.
Table 5.1 summarized energy cut for samples and searches.

Table 5.1: Summary of energy cuts for samples and searches. Here E_{vis} is the visible energy, and p_{Fit} is the fitted momentum of upward-going muon.

Search	Sample	Variable	Cut [GeV]
ν_μ	FC	E_{vis}	3.5
ν_μ	PC	E_{vis}	1.0
ν_μ	UPMU	p_{Fit}	1.6
ν_e	FC	E_{vis}	10.0

The comparison between the atmospheric neutrino data and MC events of different sample are shown in Figure 5.2.

The effective area of each sample and neutrino flavor is calculated using atmosphere

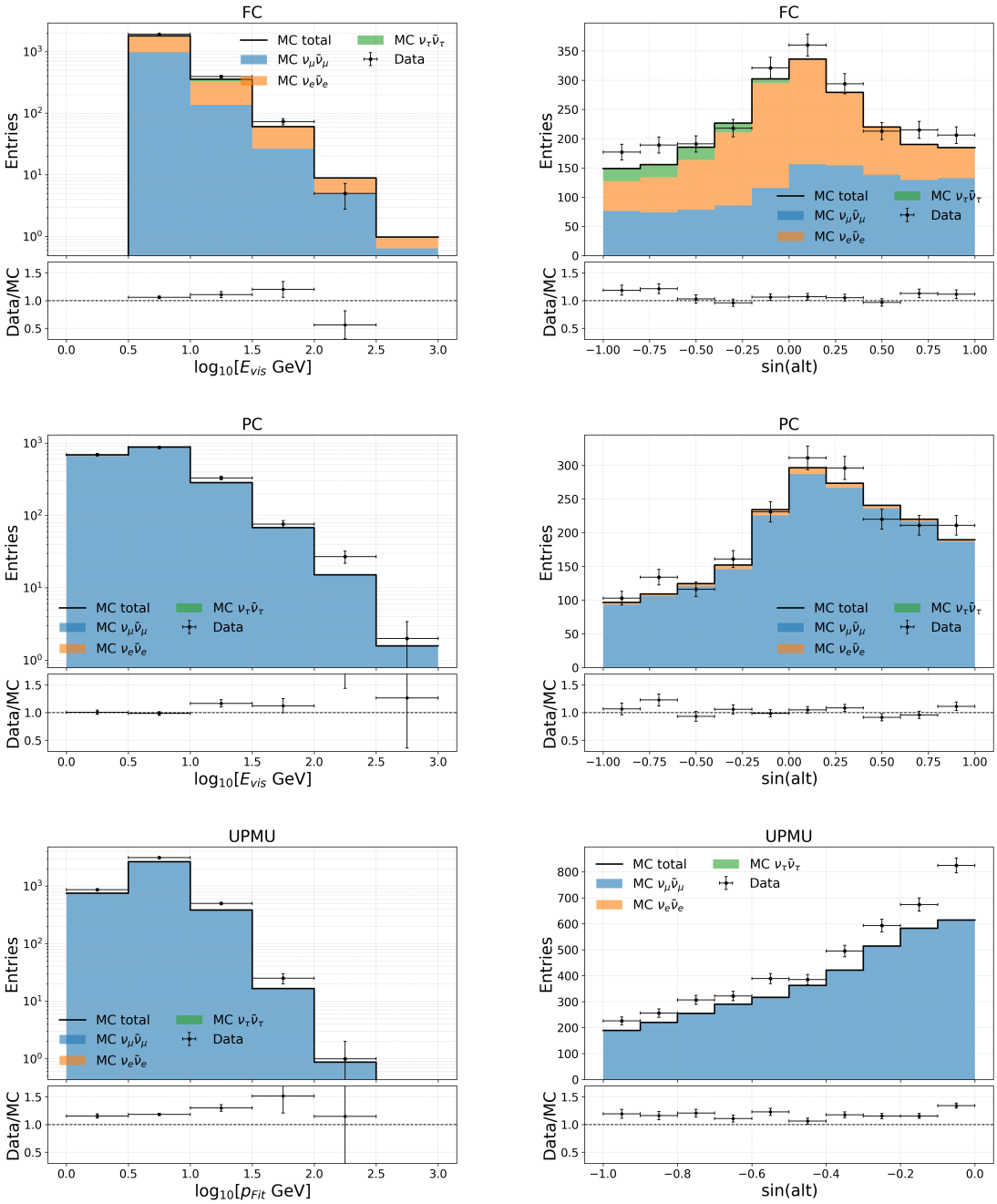

Figure 5.2: $\log_{10}[E_{vis}$ (GeV)] or $\log_{10}[p_{Fit}$ (GeV)] (left column) and $\sin(alt)$ distribution for SK-IV atmospheric FC (top), PC (middle) and UPMU (bottom) neutrino events. Black dot shows observed number of data in each bin, while black solid line shows the expected number from MC. Number of MC is normalized by the live time of SK-IV, and included neutrino oscillation and solar activity discussed in Section 3.1. Contributions of $\nu_\mu\bar{\nu}_\mu$(blue), $\nu_e\bar{\nu}_e$(orange) and $\nu_\tau\bar{\nu}_\tau$(green) from MC prediction are shown by filled stacked histogram. The ratio of data over MC is plotted in the sub-figure beneath distribution. Error bar only shows statistical error.

neutrino MC by

$$A_{eff}(E_\nu, \theta) = \frac{n(E_\nu, \theta)}{\Phi_{Honda}(E_\nu, \theta) T_{sim}} \tag{5.1}$$

where θ is the zenith angle in the detector, Φ_{Honda} is the Honda flux used for atmosphere neutrino simulation (see Chapter 3), $n(E_\nu, \theta)$ is the number of MC events with E_ν and θ. The neutrino oscillation weighted is taken into account. The effective area averaged over θ is shown in Figure 5.3.

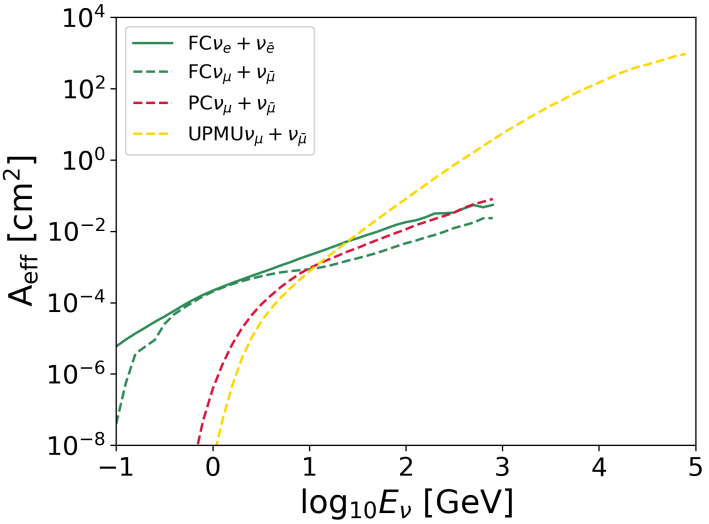

Figure 5.3: Effective area of FC ν_μ (green solid), FC ν_e (green dashed), PC ν_μ (red dashed) and UPMU ν_μ (yellow dashed) against neutrino energy.

In the ν_μ searches, no further selection cut is applied to event for event classification, because ν_e component in UPMU and PC are negligible, and UPMU sample contain the majority of the high-energy signal events due to its large effective area in high-energy region. However, event classification is necessary for the ν_e searches to separate astrophysical ν_μ component and suppress background atmosphere ν_μ events. The FC events are separated into two subsets: 1 ring events and multi-ring events, and both 1 ring and multi-ring events CCν_e-like are used in the sample. The flow of the selection procedure is illustrated in Figure 5.4.

5.1.1 FC Single-ring Event Selection

The classification of 1 ring e-like and μ-like events is described in 4. Figure 5.5 presents the particle identification (PID) likelihood used to classify e-like and μ-like events for $E_{vis} > 10$GeV. In this analysis, CC$\nu_e\bar{\nu}_e$ events are signals and CCν_μ, CCν_τ and NC are backgrounds. The selection cut on PID likelihood is changed from the one used in other SK analysis to optimize selection behavior for $E_{vis} > 10$GeV events. Since the detec-

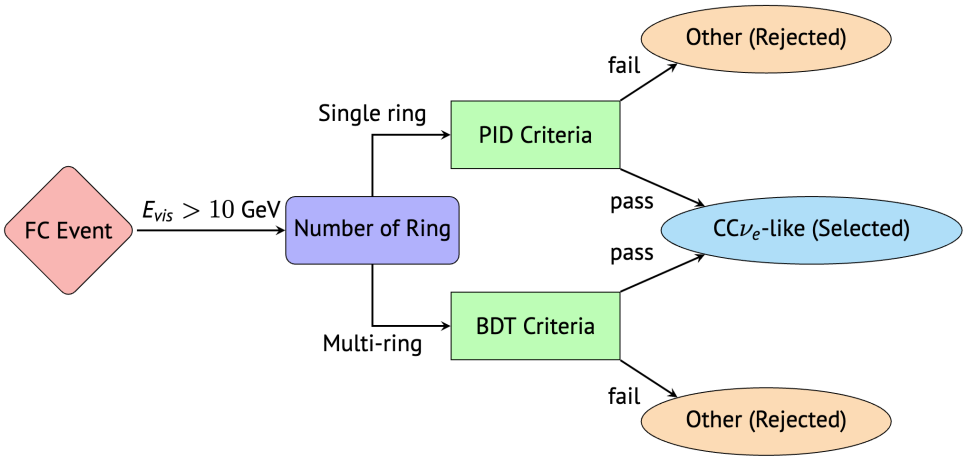

Figure 5.4: Schematic of the flow for ν_e FC event selection.

tor characteristics are not the same for each SK phase, the cut is optimized for each phase independently. For SK-IV, the events with PID smaller than -31.9 are selected, and new cut is drawn as vertical solid black line in Figure 5.5. Figure 5.6 presents the selection efficiency and expected event number assuming astrophysical neutrino flux ratio $\nu_e : \nu_\mu : \nu_\tau = 1 : 1 : 1$ at detector and power-law spectrum $\frac{d\Phi}{dE} = \Phi_0 E^{-2.7}$ for different neutrino energy E_ν bins.

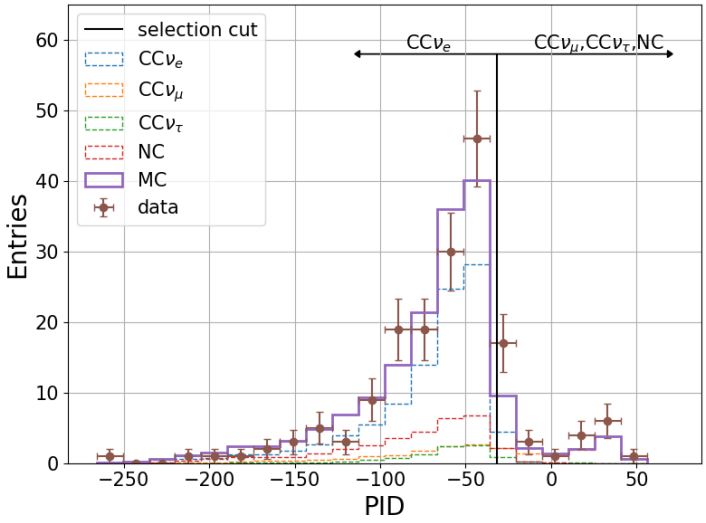

Figure 5.5: PID likelihood (square root of probms) of $E_{vis} > 10$GeV SK-IV 1 ring FC MC. Purple solid line is the sum of CCν_e (blue dashed) CCν_μ (orange dashed), CCν_τ (green dashed) and NC (pink dashed). Vertical black solid line indicate the selection cut at -31.9. Below the cut events are classified as CCν_e-like events and above it as other. Data (brown circle with error bar) of SK-IV are shown for comparison.

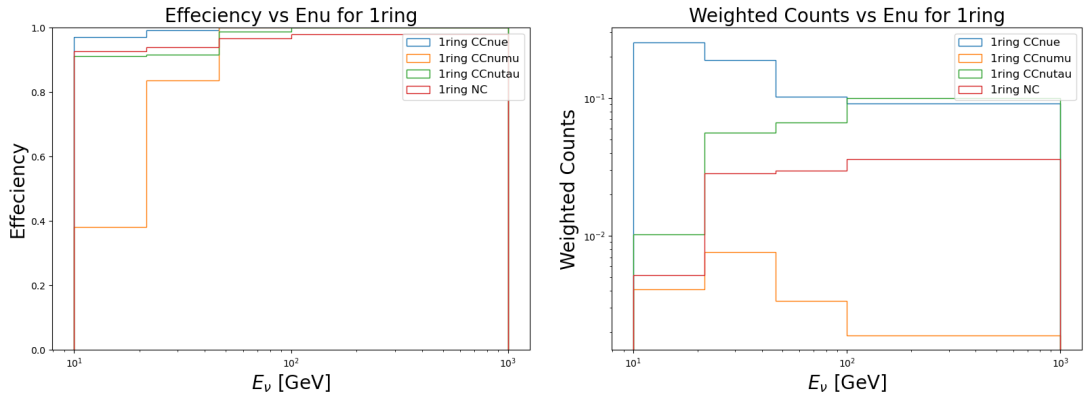

Figure 5.6: Selection efficiency (left) and relative number of events (right) of CCν_e (blue), CCν_μ (orange), CCν_τ (green) and NC (red) in different energy bins for SK-IV 1 ring FC MC. Events are weighted to follow $E^{-2.7}$ spectrum and assumes flux ratio $\nu_e : \nu_\mu : \nu_\tau = 1 : 1 : 1$.

5.1.2 FC Multi-ring Event Classification

A boosted decision tree (BDT) classifier to classify multi-GeV multir-ring CCν_e, CC$\bar{\nu}_e$, CC$\nu_\mu\bar{\nu}_\mu$, CC$\nu_\tau\bar{\nu}_\tau$ and NC is developed for other SK analysis[50]. This analysis uses the similar approach and simplified the classifier to separate signal CC$\nu_e\bar{\nu}_e$ events from background CC$\nu_\mu\bar{\nu}_\mu$, CC$\nu_\tau\bar{\nu}_\tau$ and NC events with $E_{Vis} > 10$GeV. The same seven variables are used for classification, which include:

- Visible energy (E_{vis})
- PID likelihood of the most energetic ring (PID of p_{max})
- Number of rings (N_{ring})
- Number of decay electrons ($N_{decay\ e}$)
- Largest distance between reconstructed vertex and decay electrons ($L_{decay\ e}$)
- Fraction of momentum carried by the most energetic ring (p_{max}/p_{tot})
- Transverse momentum relative to the most energetic ring ($p_{T/max}/p_{tot}$)

Figure 5.7 shows the distribution of these input variables.

The BDT score and the ROC curve is shown in Figure 5.8. The signal selection efficiency is about 60%, with a background rejection of 80%, which increased from 50% comparing with classification using PID of most energetic ring.

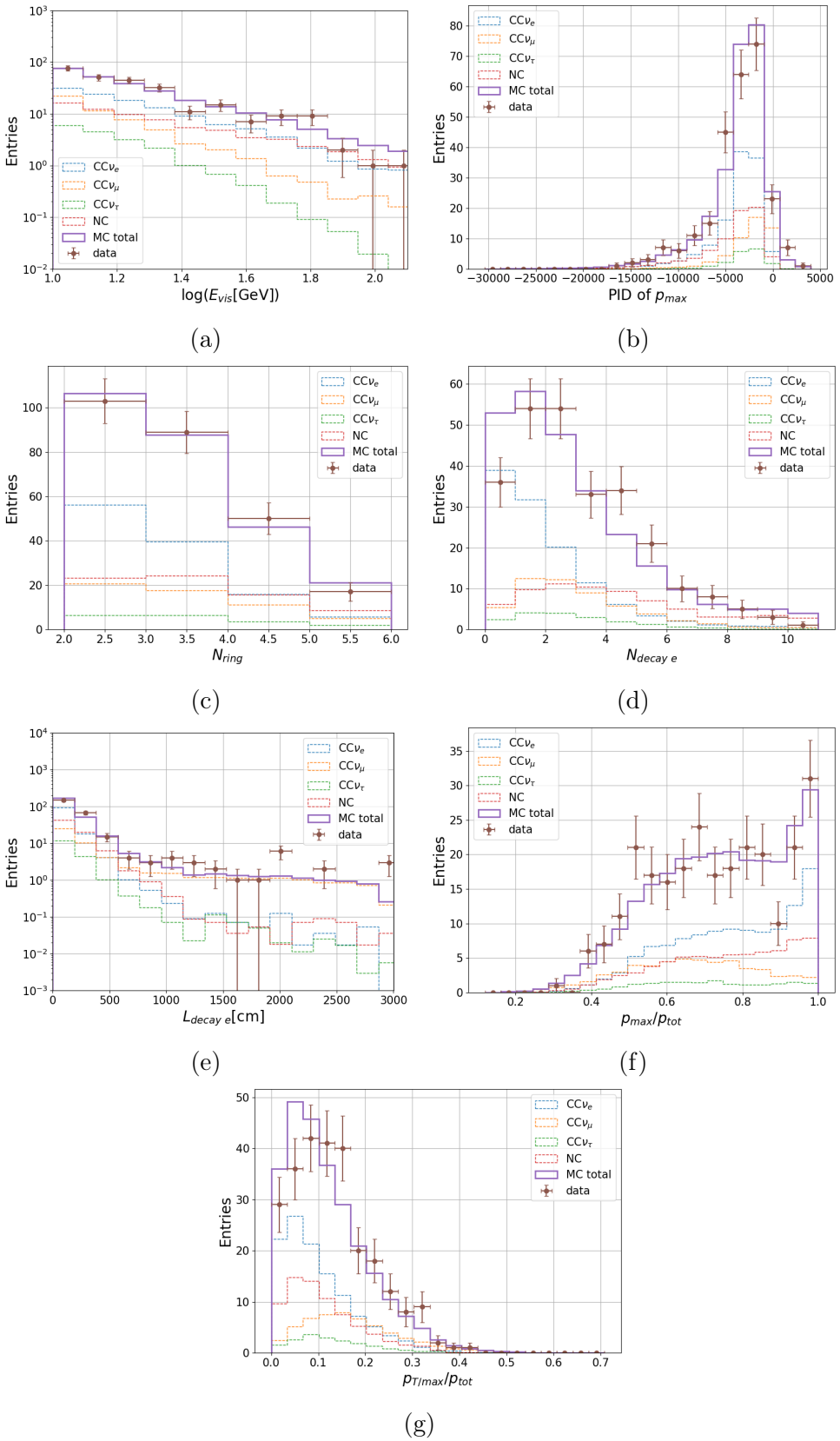

Figure 5.7: Distribution of variables for SK-IV MC used in BDT for multi-ring event classification. (a) visible energy (b) PID of most energetic ring (c) number of rings (d) number of decay electrons (e) largest distance between reconstructed vertex and decay electrons (f) fraction of momentum carried by the most energetic ring (g) transverse momentum relative to the most energetic ring. Purple solid line is the sum of CCν_e (blue dashed) CCν_μ (orange dashed), CCν_τ (green dashed) and NC (pink dashed). Data (brown circle with error bar) of SK-IV are shown for comparison.

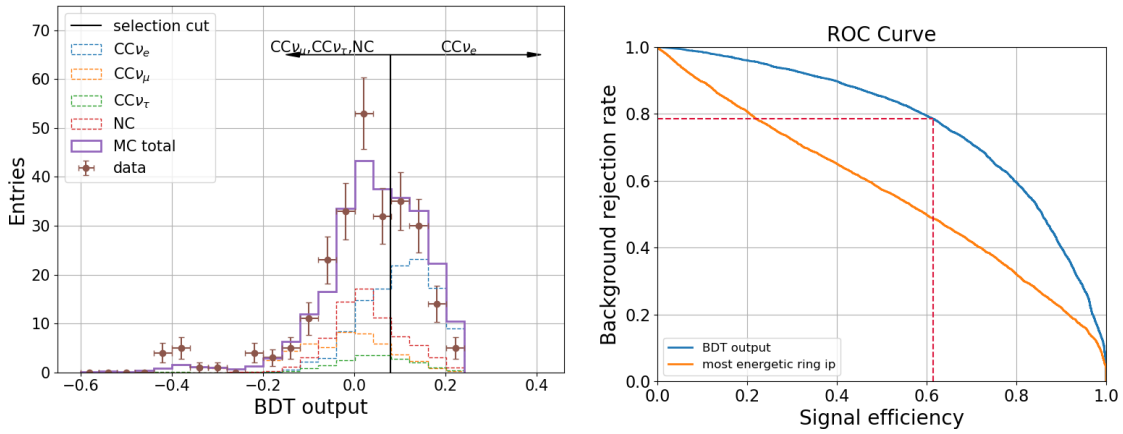

Figure 5.8: Left: BDT output distribution of SK-IV MC for multi-ring event selection. Purple solid line is the sum of CCν_e (blue dashed) CCν_μ (orange dashed), CCν_τ (green dashed) and NC (pink dashed). Vertical black solid line indicate the selection cut at 0.079. Above the cut events are classified as CCν_e-like events and below it as other. Data (brown circle with error bar) of SK-IV are shown for comparison.
Right: ROC curve of multi-ring event selection using BDT (blue) and PID of most energetic ring (orange). The signal efficiency and background rejection rate of the selection cut on BDT output are indicated by red dashed lines.

Selection efficiency and expected event number in E_ν bins assuming flux ratio $\nu_e : \nu_\mu : \nu_\tau = 1 : 1 : 1$ and $E^{-2.7}$ spectrum for multi-ring selection are shown in Figure 5.9, and Figure 5.10 shows those combining 1 ring and multi-ring events.

Summary of FC events selection results after applying the classification algorithm described above are listed in Table 5.2, while the selection efficiency and expected event number in E_ν bins for the combined 1 ring and multi-ring events are shown in Figure 5.10.

Table 5.2: MC purity of CCν_e, CCν_μ, CCν_τ and NC before and after selection cut, CCν_e events selection efficiency and number of data events before and after cut, for single ring events, multi-ring events and combining both of them.

	N_{ring}		MC Purity %				CCν_e Efficiency	Data
			CCν_e	CCν_μ	CCν_τ	NC		
ν_e-like	1 ring	before cut	60.1	13.8	5.6	20.5	97.8%	343
		after cut	64.7	8.1	5.6	21.6		302
	Mulit-r	before cut	44.9	20.7	7.0	27.4	61.4%	508
		after cut	70.0	7.0	6.0	1.7		167
	Total	before cut	50.7	18.1	6.5	24.7	78.0%	851
		after cut	66.9	7.6	5.88	19.7		469

Figure 5.11 presents the effective area of CCν_e, CCν_μ, CCν_τ and NC events after applying the selection cut for FC 1 ring and multi-ring events.

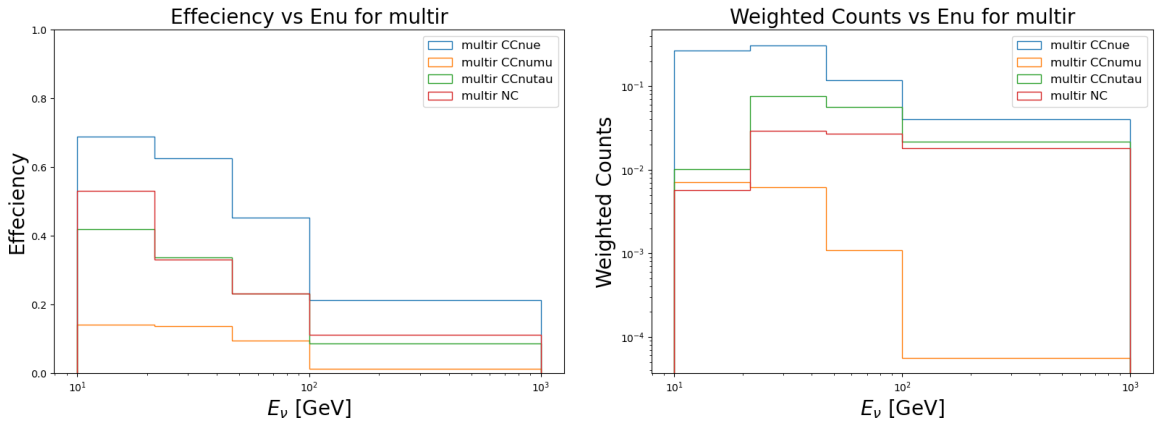

Figure 5.9: Selection efficiency (left) and relative number of events (right) of CCν_e (blue), CCν_μ (orange), CCν_τ (green) and NC (red) in different energy bins for SK-IV multi-ring FC MC. Events are weighted to follow $E^{-2.7}$ spectrum and assumes flux ratio $\nu_e : \nu_\mu : \nu_\tau = 1 : 1 : 1$.

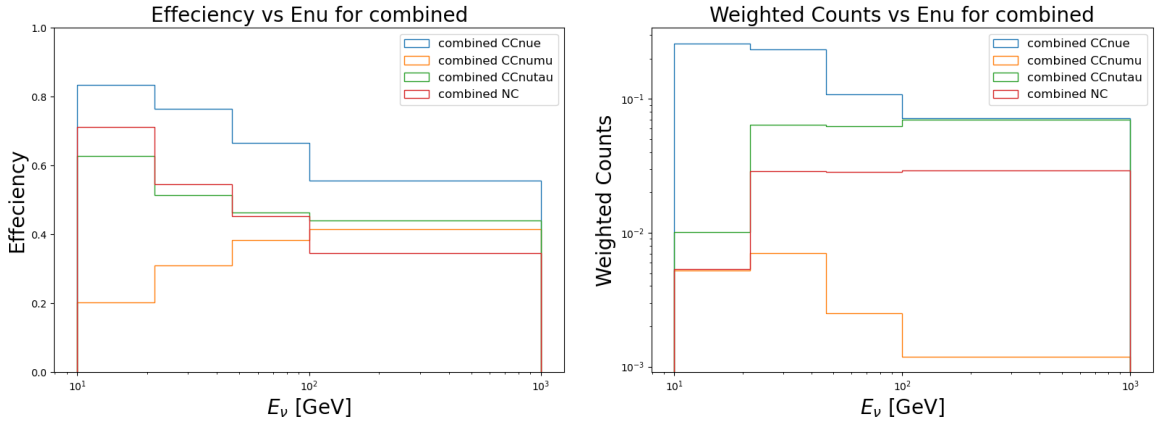

Figure 5.10: Selection efficiency (left) and relative number of events (right) of CCν_e (blue), CCν_μ (orange), CCν_τ (green) and NC (red) in different energy bins for SK-IV all FC MC (including 1 ring and multi-ring). Events are weighted to follow $E^{-2.7}$ spectrum and assumes flux ratio $\nu_e : \nu_\mu : \nu_\tau = 1 : 1 : 1$.

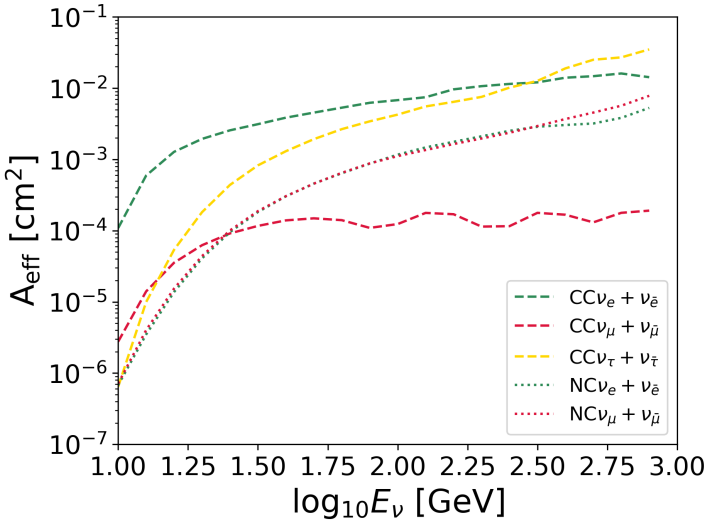

Figure 5.11: Effective area of ν_e (green), ν_μ (red), ν_τ (yellow) through CC (dashed) and NC (dotted) interactions for FC events versus logarithm of neutrino energy, after applying selection cut discussed in Section 5.1.

The summary of events used in this analysis is in Table 5.3. FC events that pass the selection cut discussed in this section will be used in the search for ν_e, and all FC, PC and UPMU events pass the energy cut will be used in the search for ν_μ in the following analysis.

Table 5.3: Live time and number of events for each SK phase and each data sample.

Phase	Live Time (days)	Number of Events			
		ν_μ			ν_e
		FC	PC	UPMU	FC
SK-I	1555.6	998	844	2325	117
SK-II	825.2	549	408	1078	41
SK-III	542.0	361	345	936	37
SK-IV	3242.9	2384	1994	4547	238
SK-V	453.4	307	268	647	36

5.2 Search Method

This analysis uses unbinned maximum likelihood method to search for excess of signal events (astrophysical neutrinos) over background (atmosphere neutrino). Depending on whether to include time information or not, searches are separated as time-dependent search and time-integrated search. Searches can also be separated as point source search and extended source search. Probability density functions (PDFs) are different for each search, but the form of the likelihood is the same. Parameters including number of signal events will be fitted to maximize the likelihood, and test statistics (TS) will be calculated to evaluate significance over null hypothesis. In the end TS will be compared with the results from trials using solely background toy MC to obtain p-value.

5.2.1 Unbinned Maximum Likelihood

In all of the following searches, energy spectrum of signal neutrino flux is assumed to be power-law spectrum $\frac{d\Phi}{dE_\nu} = \Phi_0 E^{-\gamma}$, and spectral index γ can be fixed or fitted. In a search region where expected number of signal events and background events are n_S and n_B, the likelihood to observe a event from direction $\vec{x}_i$ at time t_i with reconstructed energy E_i^{rec} (E_{vis} for FC and PC or p_{Fit} for UPMU) is given by

$$\frac{n_S}{n_S + n_B} S(\vec{x}_i, E_i^{reco}, t_i|\gamma) + \frac{n_B}{n_S + n_B} B(\vec{x}_i, E_i^{reco}, t_i) \tag{5.2}$$

where S and B are the signal and background PDF of a signal or background event, respectively. For total N events in the search region, likelihood for observing these events in their states is

$$\begin{aligned}\mathcal{L}(n_S, \gamma) &= \frac{e^{-(n_S+n_B)}(n_S+n_B)^N}{N!} \prod_{i=1}^{N} \left[\frac{n_S}{n_S + n_B} S(\vec{x}_i, E_i^{reco}, t_i|\gamma) + \frac{n_B}{n_S + n_B} B(\vec{x}_i, E_i^{reco}, t_i) \right] \\ &= \frac{e^{-(n_S+n_B)}}{N!} \prod_{i=1}^{N} \left[n_S S(\vec{x}_i, E_i^{reco}, t_i|\gamma) + n_B B(\vec{x}_i, E_i^{reco}, t_i) \right] \end{aligned} \tag{5.3}$$

For three samples (FC, PC or UPMU) and five SK phases (SK-I to SK-V), detector characteristics are different, which leads to difference in PDFs S and B. The total likelihood is the product of each sample j and phase K is

$$\mathcal{L}(n_S, \gamma) = \prod_k \prod_j \mathcal{L}_{k,j}(n_S^{k,j}, \gamma) \tag{5.4}$$

where $n_S = \sum_k \sum_j n_S^{k,j}$. Expected number of events for sample j and phase k is a related to live time T_{like}^k, effective area $A_{eff}^j(E_\nu, \delta_{src})$ at position δ_{src} and neutrino flux:

$$n_S^{k,j} = T_{live}^k \int_{E_{min}^j}^{E_{max}^j} A_{eff}^j(E_\nu, \delta_{src}) \Phi_0 E_\nu^{-\gamma} dE_\nu \tag{5.5}$$

where E_{min}^j and E_{max}^j are the minimum and maximum energy of sensitive energy region of sample j. Assuming the same flux spectrum for all phases, $n_S^{k,j}$ can be replaced by

$$n_S^{k,j} = n_S^{total} \mathcal{F}_k^{phase} \mathcal{F}_j^{sample}(\gamma, \delta_{src}) = n_S^{total} \mathcal{F}_{k,j}(\gamma, \delta_{src}) \tag{5.6}$$

with

$$\mathcal{F}_{sample}^j(\gamma, \delta_{src}) = \frac{\int_{E_{min}^j}^{E_{max}^j} A_{eff}^j(E_\nu, \delta_{src}) E_\nu^{-\gamma} dE_\nu}{\sum_j \int_{E_{min}^j}^{E_{max}^j} A_{eff}^j(E_\nu, \delta_{src}) E_\nu^{-\gamma} dE_\nu} \tag{5.7}$$

Since the difference of $\sum_j \int_{E_{min}^j}^{E_{max}^j} A_{eff}^j(E_\nu, \delta_{src}) E_\nu^{-\gamma} dE_\nu$ between phases is small, $\mathcal{F}_k^{phase}$ can be approximated by $\mathcal{F}_k^{phase} \approx \frac{T_{live}^k}{\sum_k T_{live}^k}$. Figure 5.12 presents $\mathcal{F}_j^{sample}(\gamma, \delta_{src})$ as a function of δ for different γ.

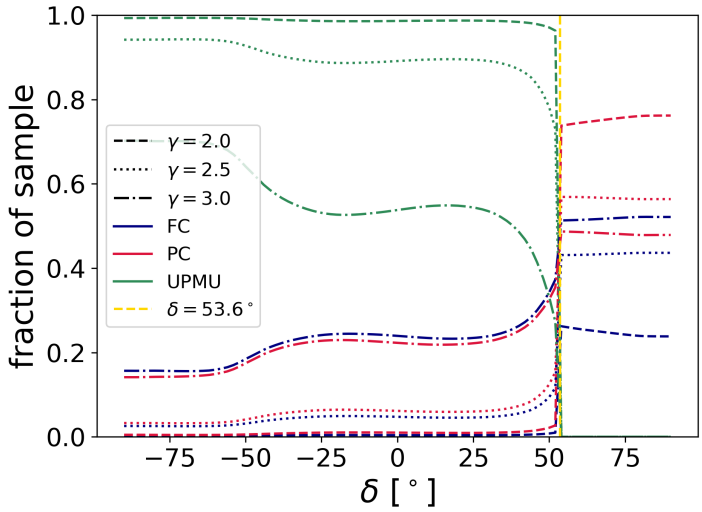

Figure 5.12: Expected fraction of SK-IV signal events in sample FC (blue), PC (red) and UPMU (green) against declination for different γs. Vertical gold dashed line indicates $\delta = 53.6°$.

Notice there is a "boarder" at around $\delta = 53.6°$, which is the UPMU sensitive region boundary. No UPMU event is coming from direction above it.
Now likelihood becomes

$$\mathcal{L}(n_S, \gamma) = \prod_k \prod_j \frac{e^{-\left[n_S \mathcal{F}_{k,j}(\gamma, \delta_{src}) + n_B^{k,j}\right]}}{N^{k,j}!} \times \prod_{i=1}^{N^{k,j}} \left[n_S \mathcal{F}_{k,j}(\gamma, \delta_{src}) S_{k,j}(\vec{x}_i, E_i^{reco}, t_i|\gamma)) + n_B^{k,j} B_{k,j}(\vec{x}_i, E_i^{reco}, t_i) \right] \tag{5.8}$$

Since n_S (and γ as well if not fixed) is an unknown variable, it can be fitted to maximize $\mathcal{L}(n_S, \gamma)$. Let $\hat{n}_S$ denote the best-fit value of number of signal events, significance of the likelihood of $\hat{n}_S$ is evaluated by the logarithmic ratio of two hypothesis:

- $\mathcal{H}_1$: data consists of $\hat{n}_S$ signal events with background event.
- $\mathcal{H}_0$: all these events are background events (null hypothesis).

and log ratio is called test statistics (TS):

$$TS = 2 \log \left[\frac{\mathcal{L}(\hat{n}_S)}{\mathcal{L}(n_S = 0)} \right] \tag{5.9}$$

with larger TS presenting more significant. Since constant $N^{k,j}$ and $n_B^{k,j}$ in the Poisson term affect neither fitting nor TS, $\mathcal{L}(n_S, \gamma)$ can be simplified to

$$\mathcal{L}(n_S, \gamma) = e^{-n_S} \prod_{k,j,i} \left[n_S \mathcal{F}_{k,j}(\gamma, \delta_{src}) S_{k,j}(\vec{x}_i, E_i^{reco}, t_i|\gamma)) + n_B^{k,j} B_{k,j}(\vec{x}_i, E_i^{reco}, t_i) \right] \tag{5.10}$$

So far the common part of likelihood and TS used in all searches have been completely constructed. In the following sections PDFs and detailed searching flow will be discussed.

5.3 Point Source Search

5.3.1 Time-Integrated Search for ν_μ and ν_e

The time-integrated search uses all events from any time in the five SK phases and searches for sources continuously emitting neutrinos. In time-integrated search for neutrino point sources, neutrino emission is assumed to be uniform over the whole search period and concentrated at a point. Time information of events is marginalized and excess integrated throughout the whole period is searched. For all point source searches, γ

is free to fit. Likelihood for a source at $\vec{x}_{src}$ is

$$\mathcal{L}(n_S, \gamma|\vec{x}_{src}) = e^{-n_S} \prod_{k,j,i} \left[n_S \mathcal{F}_{k,j}(\gamma, \delta_{src}) S_{k,j}(\vec{x}_i, E_i^{reco}|\gamma, \vec{x}_{src})) + n_B^{k,j} B_{k,j}(\vec{x}_i, E_i^{reco}) \right] \tag{5.11}$$

Since the data set is background dominated, $n_B^{k,j}$ is set to be the number of SK data events of sample j in k phase to avoid the effect of the uncertainty of atmospheric neutrino flux model. The PDFs include energy parts and spatial parts.

$$S_{k,j} = \mathcal{P}_{k,j}^{sig}(\vec{x}_i|\vec{x}_{src}, E_i^{reco}) \mathcal{E}_{k,j}^{sig}(E_{j,i}|\gamma) \tag{5.12}$$

$$B_{k,j} = \mathcal{P}_{k,j}^{bkg}(\vec{x}_i|E_i^{reco}) \mathcal{E}_{k,j}^{bkg}(E_i^{reco}) \tag{5.13}$$

For background, energy PDFs $\mathcal{E}_{k,j}^{bkg}(E_i^{reco})$ are obtained from E_{vis} (for FC and PC) or p_{Fit} (for UPMU) distribution of atmosphere neutrino MC (see Chapter 3). Blue lines in Figure 5.16 shows the PDF of FC, PC and UPMU.

The asymmetry of background distribution in right ascension is averaged out by the rotation of the earth, so spatial term in background PDF can be simplified to:

$$\mathcal{P}_{k,j}^{bkg}(\vec{x}_i|E_i^{reco}) = \mathcal{P}_{k,j}^{bkg,dec}(\delta_i|E_i^{reco})/(2\pi) \tag{5.14}$$

In atmosphere MC, distribution of sin of altitude (alt) and azimuth (az) are simulated and shown in Figure 5.13. To convert to declination distribution, a local sidereal time (LST) distribution is needed. This distribution is calculated from the run summaries by histogramizing the running hours of normal runs (see Figure 5.14). Then each MC event is randomly assigned with a detected LST according to the distribution and calculate corresponding right ascension and declination from alt, az and LST. Figure 5.15 shows the distribution of $\mathcal{P}_{k,j}^{bkg,dec}(\delta_i|E_i^{reco})$.

Distribution of background events reconstructed energy can also be obtained from atmospheric neutrino MC. The energy reconstruction efficiency has been taken into account during the simulation process. Energy PDFs of signal events are calculated by assigning weights to atmosphere MC events. For a background MC event with neutrino energy E_ν, the following weight is assigned for a given γ:

$$w = \frac{E_\nu^{-\gamma} / \int E_\nu^{-\gamma} dE_\nu}{\Phi^{atm}(E_\nu) / \int \Phi^{atm}(E_\nu) dE_\nu} \tag{5.15}$$

where Φ^{atm} is the flux spectrum used for atmosphere neutrino simulation (Figure 3.1). Systematic uncertainty between signal and background energy PDF for the same event is canceled in fitting and TS calculation. Expected energy PDF for different γ is shown

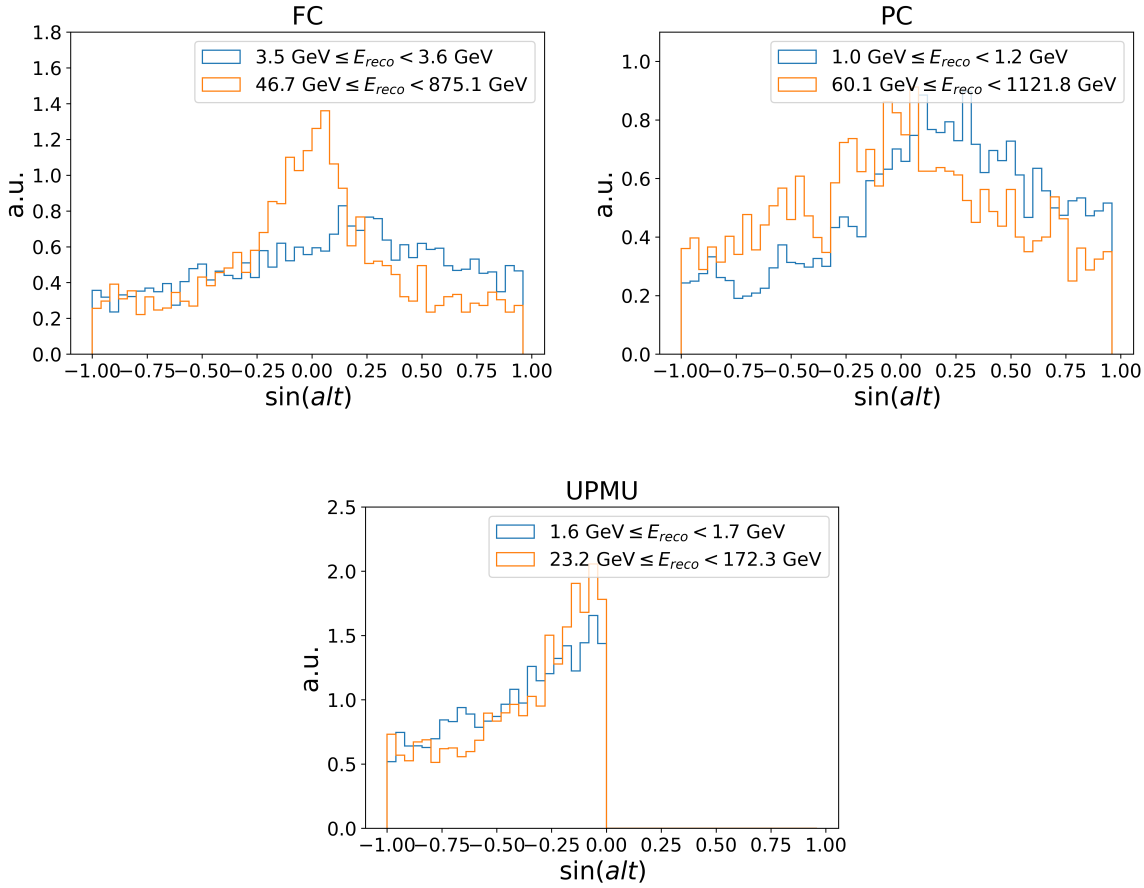

Figure 5.13: SK-IV MC spatial distribution in detector coordinate of FC ν_μ (top left), PC (top right) and UPMU (bottom) in lowest (blue) and highest (orange) reconstructed energy bin.

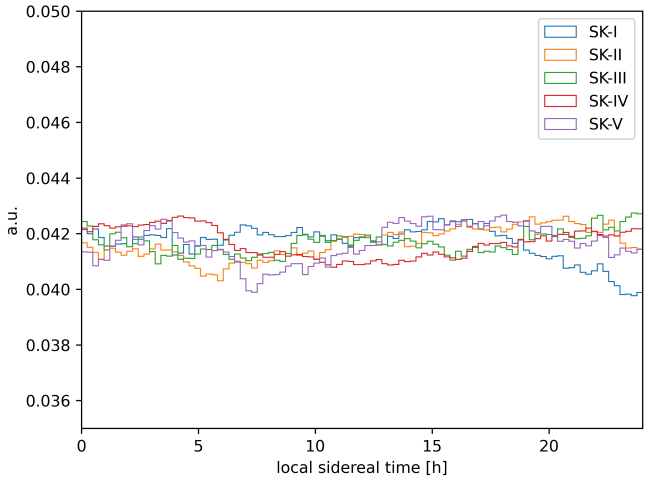

Figure 5.14: Distribution of LST obtained from run summaries of each SK phase.

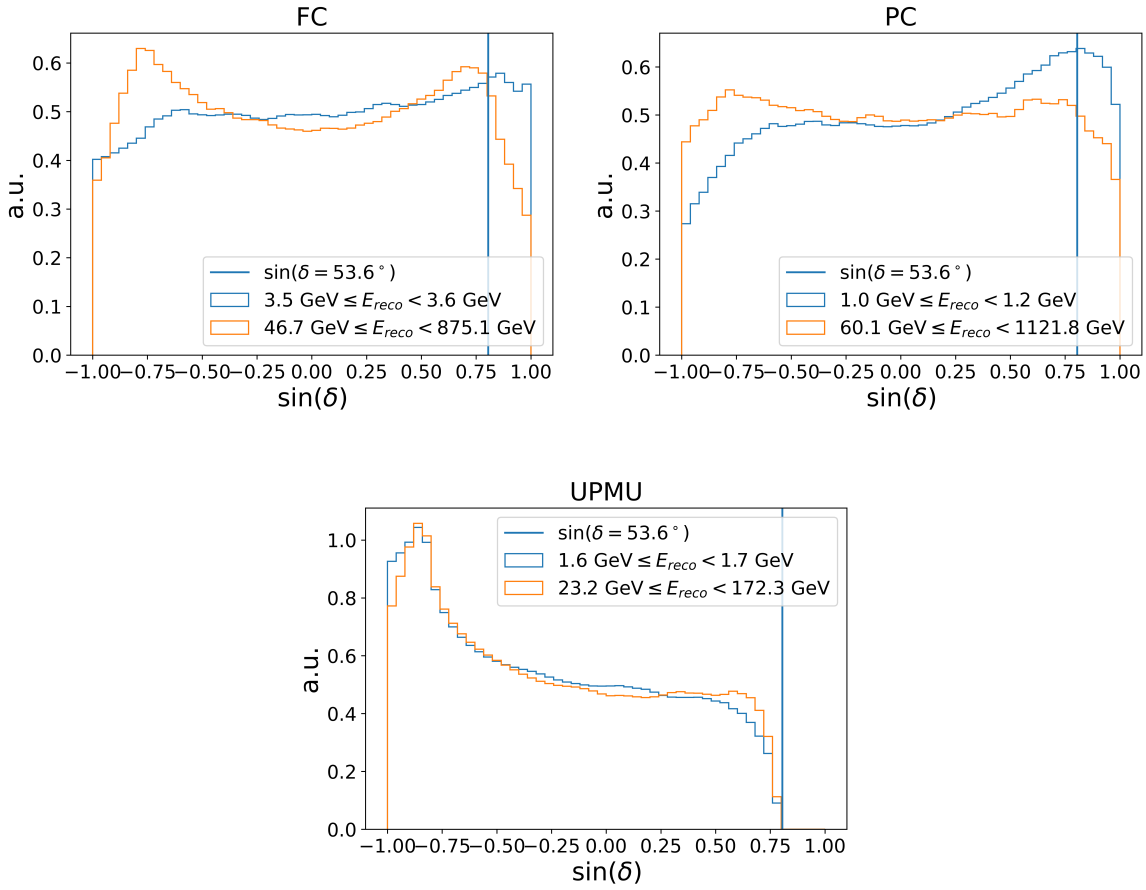

Figure 5.15: SK-IV MC spatial distribution in equatorial coordinate of FC ν_μ (top left), PC (top right) and UPMU (bottom) in lowest (blue) and highest (orange) reconstructed energy bin.

in Figure 5.16 in comparison with background energy PDF.

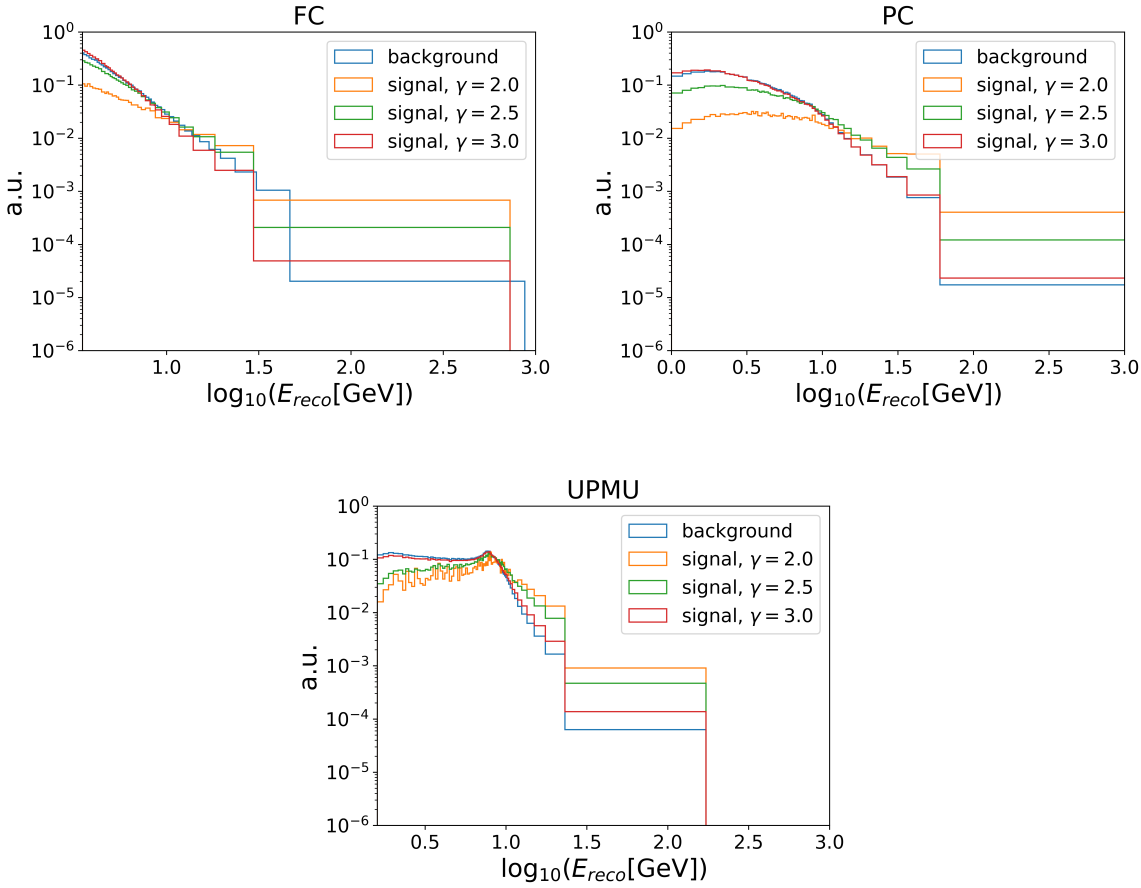

Figure 5.16: SK-IV MC energy distribution of FC ν_μ (top left), PC (top right) and UPMU (bottom) for background atmosphere neutrino (blue) and signal astrophysical neutrino assuming different spectra indices (orange, green and red).

The spatial PDF of signal depends on difference between reconstructed event position and source position $\vec{x}_i - \vec{x}_{src}$. Let $\Delta\phi \equiv \arccos\left(\frac{\vec{x}_i \cdot \vec{x}_{src}}{|\vec{x}_i||\vec{x}_{src}|}\right)$,

$$\mathcal{P}^{sig}_{k,j}(\vec{x}_i|\vec{x}_{src}, E_i^{reco}) = \mathcal{P}^{sig}_{k,j}(\vec{x}_i - \vec{x}_{src}|E_i^{reco}) = \mathcal{P}^{sig,\Delta\phi}_{k,j}(\Delta\phi|E_i^{reco})/(2\pi) \tag{5.16}$$

$\mathcal{P}^{sig,\Delta\phi}_{k,j,i}(\Delta\phi|E_i^{reco})$ is the distribution of angle between reconstructed neutrino direction and true neutrino direction of events in MC, which is shown in Figure 5.17.

When fitting the parameters, instead of maximizing $\mathcal{L}(n_S, \gamma|\vec{x}_{src})$, $-\log\mathcal{L}(n_S, \gamma|\vec{x}_{src})$ is minimized. The minimizer used in this search is iminuit, which is the python version of MINUIT. In principle n_S can be negative, representing down-ward fluctuation. However this search is seeking excess of neutrino, so n_S is limited to be non-negative. γ is scanned in the range $[1, 4]$ with a starting value of 2. The energy PDF $\mathcal{E}^{bkg}_{k,j}(E_i^{reco})$ for signal is cal-

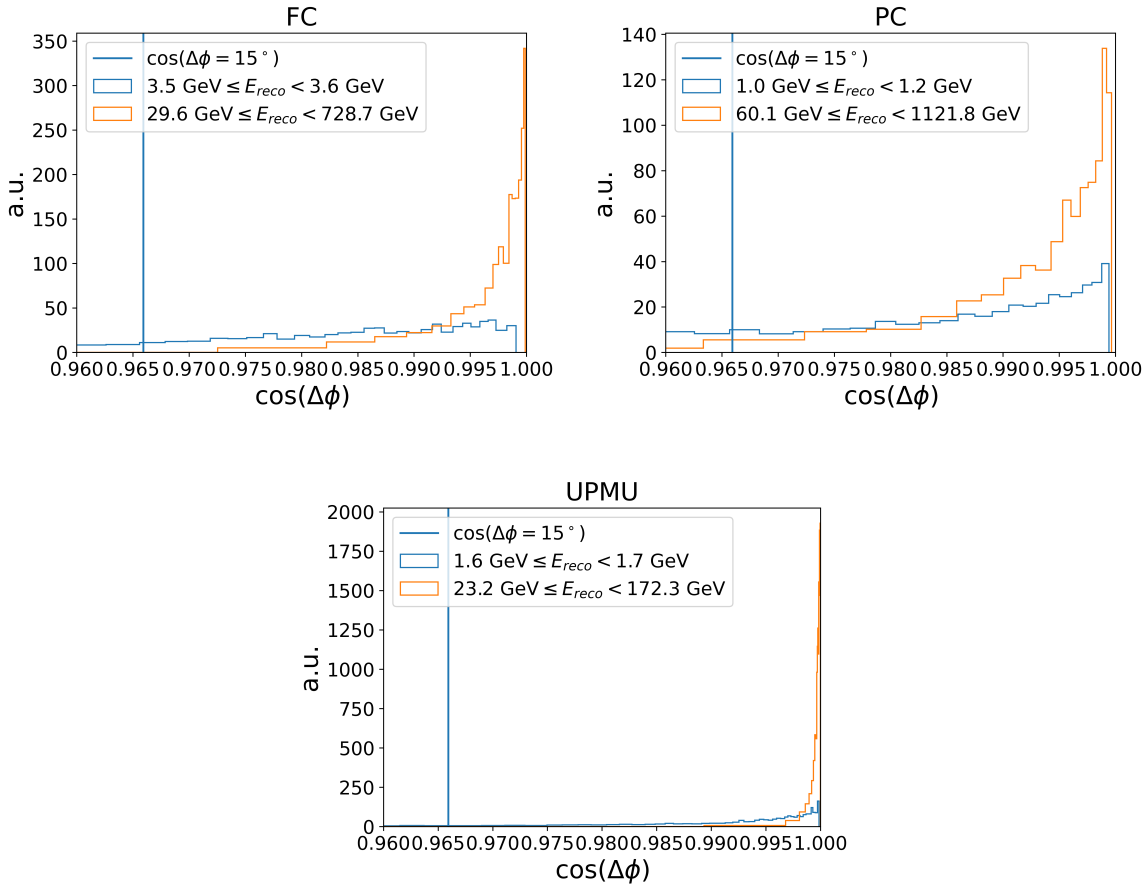

Figure 5.17: SK-IV MC point spread function FC ν_μ (top left), PC (top right) and UPMU (bottom) in lowest (blue) and highest (orange) reconstructed energy bin. Vertical line indicates cos(15°).

culated for γ with a step of 0.1. In order to make the minimizer fit γ smoothly, $\mathcal{E}_{k,j}^{bkg}(E_i^{reco})$ is interpolated linearly between two adjacent γs of which $\mathcal{E}_{k,j}^{bkg}(E_i^{reco})$ are calculated.

In the full-sky search the sky is divided into 49152 equal-area pixels using the HEALPix method[17] and the center of each pixel is used as one searching direction. Figure 5.18 shows a illustration of how the sky is divided into using HEALPix. The fit of parameters n_S, γ (and also t_0 and σ_t for time-dependent search) and maximization of likelihood, and the calculation of the TS is performed for every searching directions. Since there is no UPMU events coming above $\delta = 53.6°$, only FC and PC events are used for ν_μ search event if the search region overlapped with UPMU sensitive region.

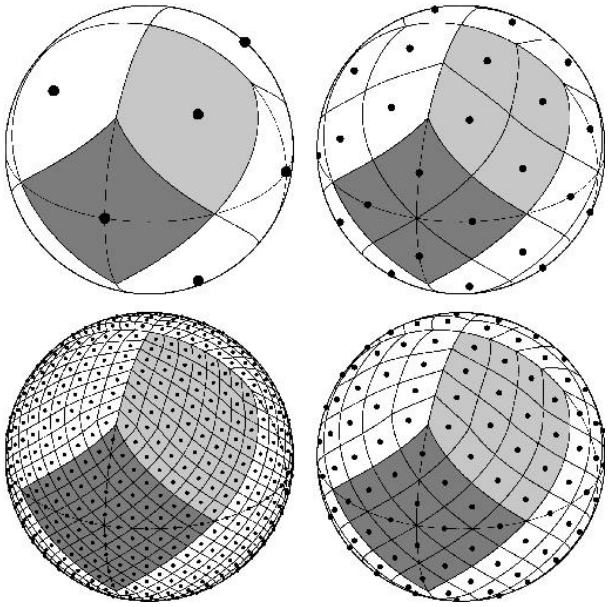

Figure 5.18: Illustration of dividing the sky into pixels (starting from top-left and go clock-wise: nside=4, 8, 16, 32). Center (dots) of each pixel is used as searching direction.

After the search being performed in every direction, the hottest spot over all sky that represents the most probable direction of source can be picked out. However, simply choosing the direction with largest TS is not enough. As can be seen from Figure 5.15, background distribution is not uniform over all declinations. As a result, event with the same TS, the significance of excess at different declination can be different. This is especially true between the region above and below $\delta = 53.6°$ in the ν_μ search. To take this into account, the local p-value (or pre-trial p-value) is calculated by comparing the TS with the distribution of TS at the same declination from pseudo-experiments. Details of the pseudo-experiments will be discussed in Section 5.6 later.

The searches with source candidates use candidates of two categories: sources from TeVCat[49], and trigger from IceCube[43]. TeVCat is a catalog of sources with TeV

gamma ray observation. IceCube trigger are triggers for high-energy currently released from 2010 to 2017. Name and position information are listed in Table A.1 and Table A.2 in Section A. For each candidate, its position is used as the search direction, and $\hat{n}_S$ and $\hat{\gamma}$ are fitted with the same procedure as for one pixel in the sky-scan is performed.

5.3.2 Time-Dependent Search

In time-integrated search, the neutrino emission is assumed to be steady over a long period comparable with SK running time. There could be, however, more drastic burst of neutrino emission in a shorter period. Such burst can be averaged out in time and does not stand out in the time-integrated search as time information is discarded. Background contamination will also be reduced within shorter time. For neutrino emitted from source $\vec{x}_{src}$ at time t_0, likelihood is

$$\mathcal{L}(n_S, \gamma|\vec{x}_{src}, t_0) = e^{-n_S} \prod_{k,j,i} \left[n_S \mathcal{F}_j^{sample}(\gamma, \delta_{src}) S_{k,j}(\vec{x}_i, E_i^{reco}, t_i|\gamma, t_0) + n_B^{k,j} B_{k,j}(\vec{x}_i, E_i^{reco}, t_i) \right] \tag{5.17}$$

The term $\mathcal{F}_k^{phase}$ that appears in $\mathcal{F}_{k,j}$ is no longer needed. The time distribution of signal events will resolve such information in it. Signal and background PDF both get a extra time term compared with time-integrated search.

$$S_{k,j} = \mathcal{P}_{k,j}^{sig}(\vec{x}_i|\vec{x}_{src}, E_i^{reco}) \mathcal{E}_{k,j}^{sig}(E_i|\gamma) \mathcal{T}^{sig}(t_i|t_0) \tag{5.18}$$

$$B_{k,j} = \mathcal{P}_{k,j}^{bkg}(\vec{x}_i|E_i^{reco}, t_i) \mathcal{E}_{k,j}^{bkg}(E_i^{reco}) \mathcal{T}^{bkg} \tag{5.19}$$

The signal time distribution is assumed to be Gaussian:

$$T^{sig}(t_i|t_0) = \frac{1}{\sqrt{2\pi}\sigma_t} \exp\left[-\frac{(t_i - t_0)^2}{2\sigma_t^2} \right] \tag{5.20}$$

where σ_t is emission time duration (Gaussian standard error) while background distribution is uniform

$$\mathcal{T}_k^{bkg} = \frac{1}{T_{live}^k} \tag{5.21}$$

There is one thing that has to be stressed. In time-integrated search the spatial distribution, time prior is marginalized, or in another way, symmetry in right ascension is assumed. as long-time exposure averaged the difference out, but this is no longer the case when the period is short (especially if shorter than a day). Such difference rise from the angle between detector coordinate and equatorial coordinate. For a given time, background event spacial distribution in equatorial coordinate will be exactly the same as the distribution in detector coordinate with a rotation of coordinate z axis. But seeing

from the equatorial coordinate, the symmetry in right ascension does not exist anymore, as is shown in Figure 5.19.

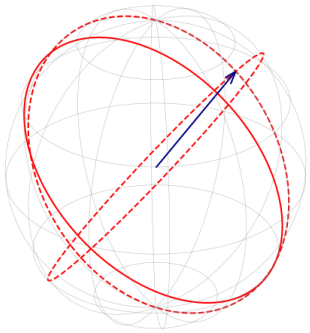

Figure 5.19: Illustration of detector coordinate (red lines) embedded in equatorial coordinate (gray lines) for a give LST. Red solid circle represents horizon (xy-axis plane) and blue arrow represents upward z direction in detector coordinate. At this moment, neutrino spatial distribution follows exactly the distribution as in detector. The break of symmetry in equatorial coordinate is obvious for UPMU events, where no events in the half-sphere of blue vector separated by red circle.

In principal a spatial distribution in equatorial coordinate at time t_i is needed, but a simpler solution is to go back to detector system. Since rotation transformation is uniform transformation, PDF normalized with respect to solid angle is kept unchanged:

$$\mathcal{P}^{bkg}_{k,j}(\vec{x}_i|E^{reco}_i,t_i) = \mathcal{P}'^{\,bkg}_{k,j}(\vec{x}'_i|E^{reco}_i,t_i) = \mathcal{P}^{bkg,alt}_{k,j}(alt_i|E^{reco}_i)/(2\pi) \tag{5.22}$$

In this search, no prior of signal time distribution is applied either. Thus t_0 and σ_t are also needed to be fitted. However, the effective trial factor will arise in this case as the choices of t_0 and σ_t are not completely independent with each other. Suppose there are n independent ways of choosing non-overlapping time windows within time range $[T_{min}, T_{max}]$ for a given σ_t, then the search is equivalent to n independent searches. This analysis follows the approach in [6] to include this affect.
First, the dependence on t_0 is marginalized by integrating $\mathcal{L}(n_S, \gamma, \sigma_t, t_0)$ with a uniform prior with respect to t_0 over $[T_{min}, T_{max}]$ using Bayesian theorem:

$$\mathcal{L}(n_S,\gamma,\sigma_t) = \int_{T_{min}}^{T_{max}} \mathcal{L}(n_S,\gamma,\sigma_t,t_0)\frac{1}{T_{max}-T_{min}}dt_0 \tag{5.23}$$

The integral is maximized with maximum likelihood $\mathcal{L}(\hat{n}_S, \hat{\gamma}, \hat{\sigma}_t, \hat{t}_0)$. Since this search aims to search drastic neutrino burst in a short period (see Figure 5.20), maximum $\mathcal{L}(n_S, \gamma, \sigma_t)$ can be approximated (omitting constant factor $\sqrt{2\pi}$) by

$$\mathcal{L}(\hat{n}_S, \hat{\gamma}, \hat{\sigma}_t) \approx \frac{\hat{\sigma}_t}{T_{max} - T_{min}} \mathcal{L}(\hat{n}_S, \hat{\gamma}, \hat{\sigma}_t, \hat{t}_0) \tag{5.24}$$

and TS becomes

$$TS = 2 \log \left[\frac{\hat{\sigma}_t}{T_{max} - T_{min}} \times \frac{\mathcal{L}(\hat{n}_S, \hat{\gamma}, \hat{\sigma}_t, \hat{t}_0)}{\mathcal{L}(n_S = 0)} \right] \tag{5.25}$$

As discussed in previous Section, minimizer is used to fit the parameters. The limits and initial value for t_0 and σ_t however are more complicated. This is because there can potentially be multiple local maximum likelihood (minimum for minimizer). The method similar to the one introduced in [6] is deployed to obtain the 'first guess' for t_0 and σ_t. The process is as follow. First select events within 5° around the search direction, and sort the events with respect to their detection time t_i. Then subsets of m (m from 2 to 10) consecutive events starting from ith event (i from 1 to n-m, where n is the number of selected events in first step) are selected (for example $[e_3, e_4, e_5]$ and $[e_4, e_5, e_6]$ are two subsets when m=3 and i=3 or 4, respectively). The mean and standard deviation of t_i of each subset events are calculated and used as t_0 and σ_t. Then likelihood in Equation 5.17 is calculated, and t_0 and σ_t that maximize the likelihood from all combination of m and i will be used as first guess.

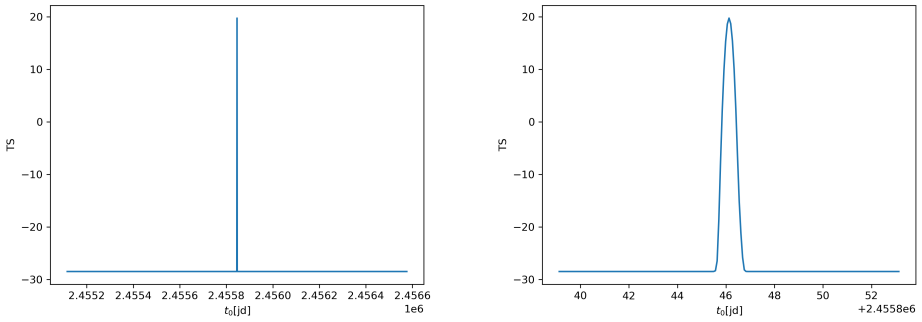

Figure 5.20: TS as a function of t_0 in time-dependent search using background and signal toy MC. n_S, γ and σ_t are fixed at the values of injected toy MC. Right plot is a zoomed-in version of left plot around t_0 of injected MC. It can be seen that TS only stands out significantly around the center.

5.4 Search for Diffuse ν_e from Galactic Plane

So far the searches being discussed assume that neutrinos come from the point-like source. The galactic plane, however, extends like a band in the sky. The neutrino emission is not expected to be uniform in the region, as the high-energy gamma ray flux observation is more intense and there are more potential sources near galactic center. Thus, a map that describes the relative intensity of neutrino emission in the galactic plane region is needed. In this analysis, the π^0 model from [1] is utilized as the map. As discussed in Section 1.2, high-energy γ rays and ν are generated during hadronic process and both succeed the spectrum of cosmic ray. For the same reason their spatial relative intensity should be the same as well. Such intensity is multiplied by the effective area of that declination pixel by pixel and normalized with respect to solid angle Ω of a HealPix sky map with nside = 64. The normalized sky map is shown in Figure 5.21.

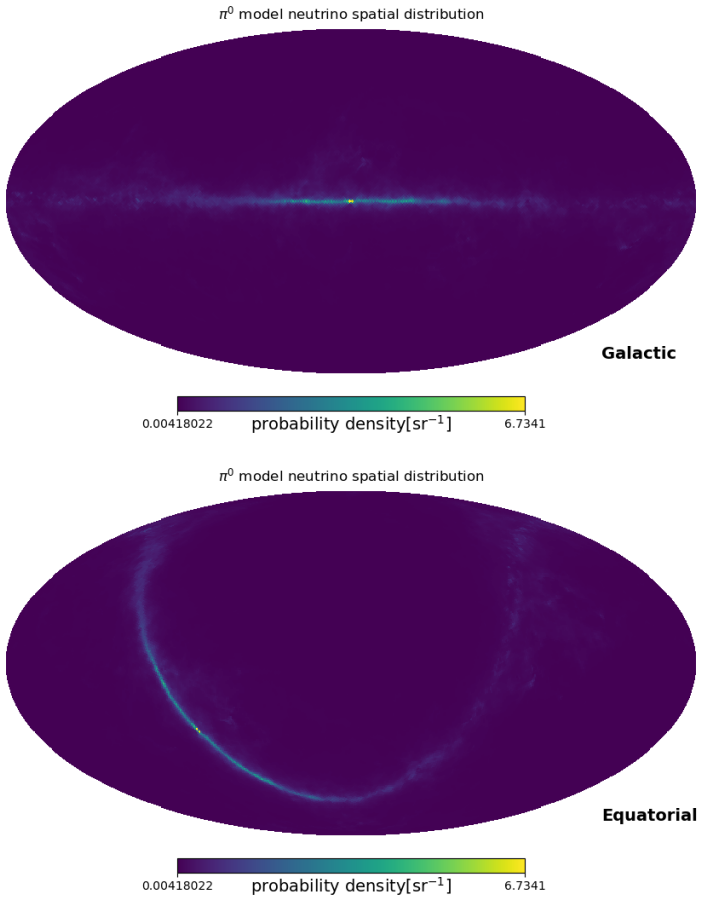

Figure 5.21: Model predicted spatial distribution in galaxy coordinate (left) and equatorial coordinate (right). Effective area of SK at different declination taken into account. Normalized to solid angle.

The search is performed with data sample for ν_e search for two reasons. First , as

discussed in Section 5.1, there are fewer atmosphere ν_e background in high-energy region. The galactic plane extended about 1/4 of the full sky and data sample is expected to be background dominated. Another reason is IceCube found evidence of diffuse neutrino from galactic plane using cascade event sample[21], which consists of a considerable fraction of ν_e.

Since the coming direction of the neutrino and reconstructed direction have an angle, the distribution of reconstructed neutrino direction will be smeared. The point spread function is calculated in the same way as discussed in Section 5.3.1, but using only the simulation of FC ν_e-like events that passed the selection discussed in Section 5.1 instead. The probability is shown in 5.22.

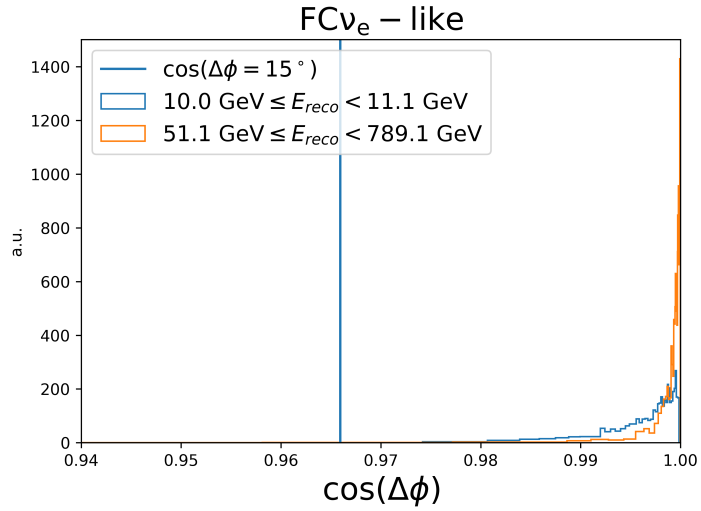

Figure 5.22: SK-IV MC point spread function of FC ν_e-like events in lowest (blue) and highest (orange) reconstructed energy bin. Vertical line indicates cos(15°).

The smeared distribution is calculated by convoluting spatial distribution with point spread function

$$\mathcal{P}_k^{smeared}(\alpha,\delta|E_{reco}) = \int_{-\pi/2}^{\pi/2}\int_0^{2\pi} \mathcal{P}^{\pi^0}(\alpha',\delta')\mathcal{P}_k^{sig}[\Delta\phi(\alpha,\delta,\alpha',\delta')|E_{reco}]d\alpha'\cos\delta' d\delta' \quad (5.26)$$

where $\mathcal{P}^{\pi^0}(\alpha',\delta')$ is the spatial distribution in Figure 5.21 and $\mathcal{P}_k^{sig}[\Delta\phi(\alpha,\delta,\alpha',\delta')|E_{reco}]$ is the point spread function in Figure 5.22. To reduce the number of background events, the search region is limited to $[-15°, 15°]$ of the latitude in galaxy coordinate. This region covers the most luminous region, and is consistent with angular resolution of selected events sample. The final normalized sky map is shown in Figure 5.23.

The search select events within ±15° region around galactic plane, and the γ in this

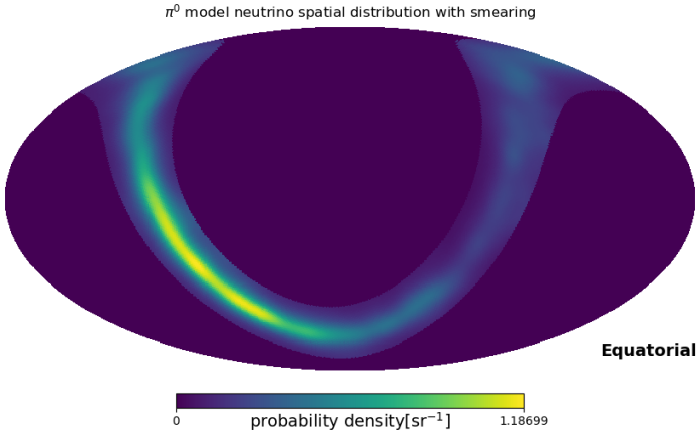

Figure 5.23: SK-IV MC signal events spatial distribution in equatorial coordinate. Smeared with point spread function in the lowest reconstructed bin. Normalized to solid angle in $|b| < 15°$.

search is also set to 2.7. Now the likelihood becomes:

$$\mathcal{L}(n_S) = e^{-n_S} \prod_{k,i} \left[n_S \mathcal{F}_k^{phase} S_k(\vec{x}_i, E_i^{reco}|\gamma) + n_B^k B_k(\vec{x}_i, E_i^{reco}) \right] \tag{5.27}$$

where n_S now represents the total number of signal events in the whole search region. As the search region covers nearly 1/4 of the sky, the potential contribution of neutrinos from the Galactic plane in the data can not be ignored. Thus, n_B^k is set to the number of MC events normalized by live time of the SK-k phase. Background PDF $B_k(\vec{x}_i, E_i^{reco})$ is also obtained using the same method discussed in Section 5.3.1. Distribution is shown in Figure5.24.

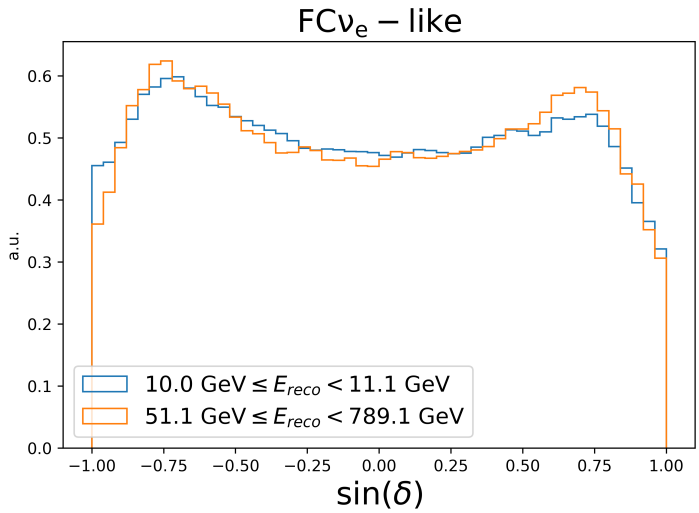

Figure 5.24: SK-IV MC spatial distribution in equatorial coordinate of FC ν_e-like events in lowest (blue) and highest (orange) reconstructed energy bin.

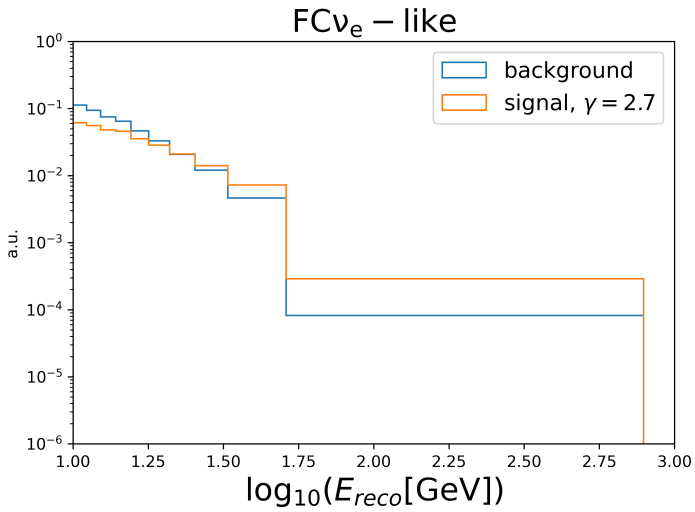

Figure 5.25: Energy distribution of FC ν_e-like events for background atmosphere neutrino and signal astrophysical neutrino assuming spectra indices $\gamma = 2.7$.

For signal PDF,

$$S_k = \mathcal{P}_k^{sig}(\vec{x}_i|E_i^{reco})\mathcal{E}_k^{sig}(E_i|\gamma) \tag{5.28}$$

definition of $\mathcal{E}_k^{sig}(E_i|\gamma)$ remains the same, and probability density for selected ν_e events is shown in Figure 5.25. $\mathcal{P}_k^{sig}(\vec{x}_i|E_i^{reco})$ is replaced with the distribution shown in Figure 5.23.

5.5 Stacked Search for ν_e from Stacked Source in Galactic Plane

In Section 1.3.4 several types of sources in galactic plane that potentially contribute to diffuse neutrinos from the galactic plane have been discussed. This search chose 36 sources from three types (12 of each): supernova remnant (SNR), pulsar wind nebula (PWN) and unidentified source (UNID). Source by source search is introduced in Section 5.3.1. By stacking together the 12 sources from the same type, the potential emission strength is enhanced, and an overall neutrino excess is searched for. Each source is assigned equal weight at this stage. Likelihood in these searches are the same as in search for point source, but the signal PDF is replaced with the sum of signal PDF of each source

$$S_{k,j}^{stack}(\vec{x}_i, E_i^{reco}|\gamma) = \frac{1}{N_{src}} \sum_{l=1}^{N_{src}} S_{k,j}^{l}(\vec{x}_i, E_i^{reco}|\gamma) \tag{5.29}$$

where N_{src} is the number of stacked sources. The signal spatial PDF shown in Figure 5.26.

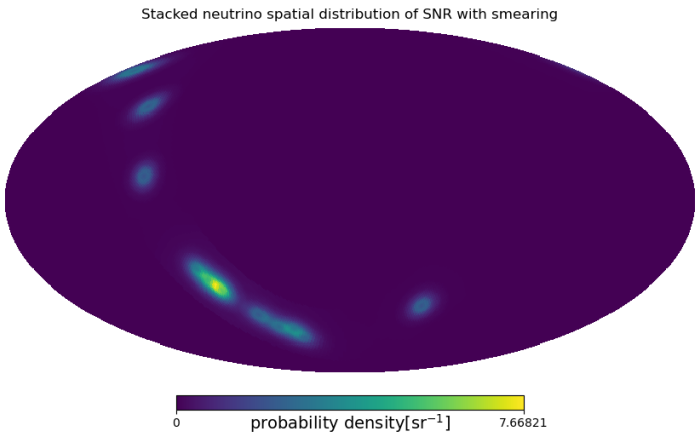

(a) SNR

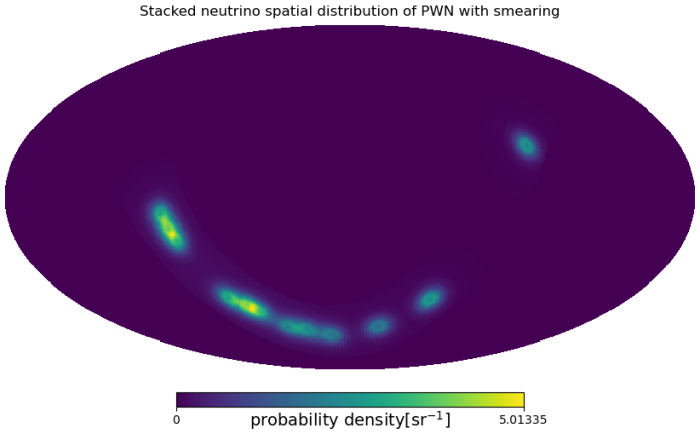

(b) PWN

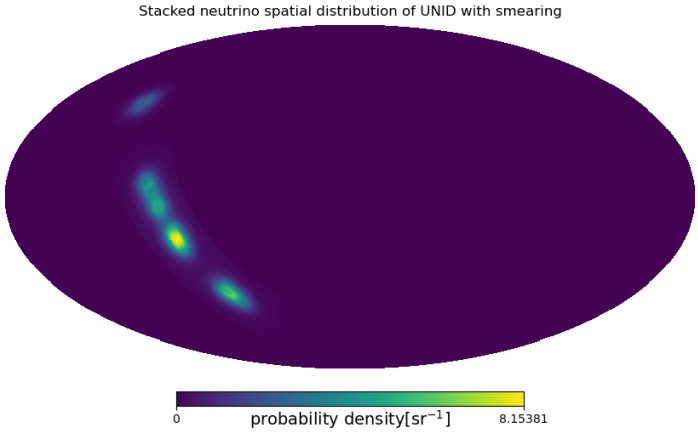

(c) UNID

Figure 5.26: SK-IV MC stacked signal events spatial distribution in equatorial coordinate for SNR (top), PWN (middle) and UNID (bottom). Smeared with point spread function in the lowest reconstructed bin. Normalized to solid angle in $|b| < 15°$.

5.6 Trial(Pseudo-experiment)

In order to estimate the significance of a result against background fluctuation, trials (or pseudo experiment) are run. Trials follow exactly the same procedures of each actual search, but uses toy MC instead of data. Toy MCs are generated from atmosphere ν MC. Each set of toy MC corresponds to events of the entire SK-I to SK-V phases. For point source search, the number of background toy MC follows Poisson distribution with mean value equal to number of observed data events, while in search for diffuse neutrino from Galactic plane and stacked search for neutrino from Galactic sources, the mean is equal to number of atmospheric MC events normalized by 6619.1-day live time. Events in toy MC are generated separately for each SK phase with respect to the distribution of each, and then merged together.

For background toy MC, number of events is chosen assuming a Poisson distribution with mean value of event rate times live time of that phase. Reconstructed energy, reconstructed direction in detector coordinate system and time of detection are assigned randomly based on their distribution (see Figure 5.16, Figure 5.15 and Figure 5.14).

5.6.1 Search Method Demonstration

Using the search methods described in the previous Section, their performances in this analysis is checked using toy MC. In Figure 5.27, the search for ν_μ sources using only background toy MC is performed and TS distribution is shown. Below $\delta = 53.6[^\circ]$ UPMU dominates due to good angular resolution and large effective area.

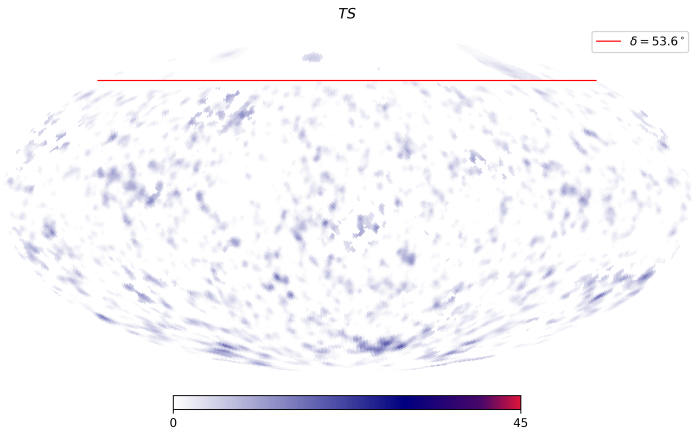

Figure 5.27: TS sky map in time-integrated search trial no signal toy MC events.

Next, several signal toy MC events are added on top of background events and performed full sky search, and the result is shown in Figure 5.28. The hottest spot find by

the algorithm is the center of the red circle, with true direction of the source marked with orange dashed line.

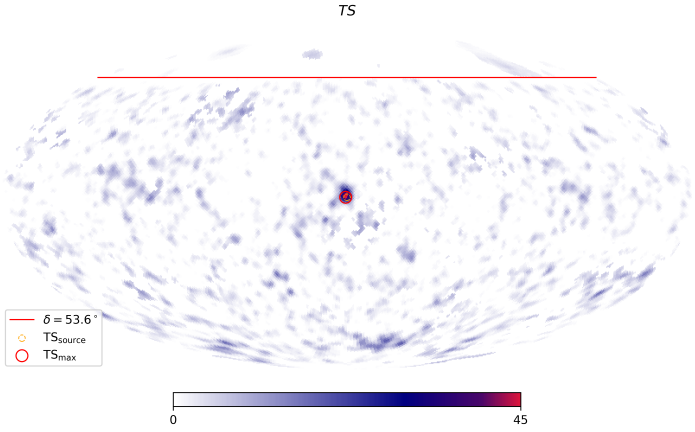

Figure 5.28: TS sky map in time-integrated search with 14 signal toy MC events at $(\alpha, \delta) = (180°, 0°)$ (yellow dashed circle). The direction of maximum TS is indicated by red circle.

The best fitted value of parameters ($\hat{n}_S$, $\hat{\gamma}$, $\hat{\sigma}_t$, $\hat{t}_0$) will not always equal to the true value due to fluctuation. The distribution of best fitted parameters from trials reflects the capability of fitting. Figure 5.29 and Figure 5.30 shows the relation between median of best fitted value and the 'true' value of generated signal toy MC used in trials, against n_S^{inj}. γ can be fitted unbiasedly with large number of generated events.

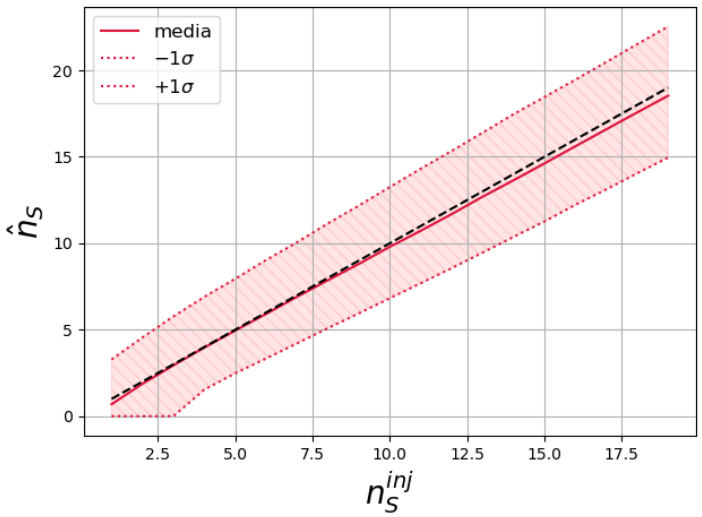

Figure 5.29: Median of $\hat{n}_S$ (solid red line) and number of injected signal toy MC (n_S^{inj}, black dashed line) against n_S^{inj}, at $\delta = -15°$, and $\gamma^{inj} = 2$ in time-integrated search.

The capabilities of fitting the time parameters t_0 and σ_t correctly is also checked by

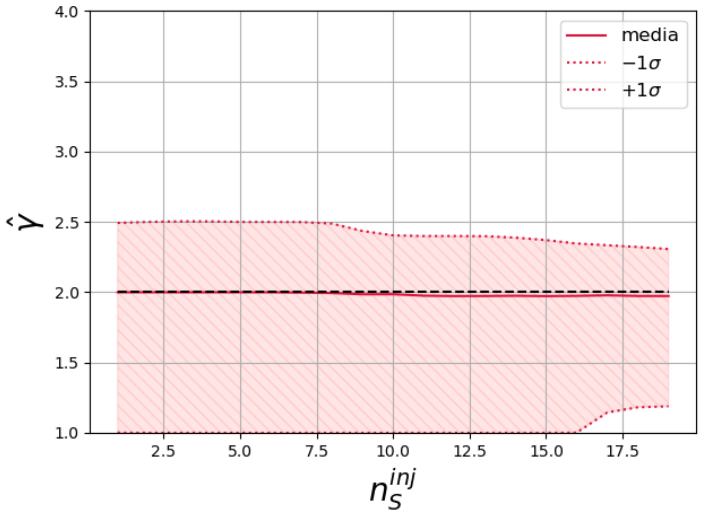

Figure 5.30: Median of $\hat{\gamma}$ (solid red line) and spetral index of injected signal toy MC (γ^{inj}, black dashed line) against n_S^{inj}, at $\delta = -15°$ in time-integrated search.

trials using both signal toy MC and background toy MC. The times of signal events are assigned according to Gaussian distribution with $\sigma_t = 10^4$ s, and TS distribution of t_0 and σ_t is shown in Figure 5.31, with the location of largest TS circled by the blue circle.

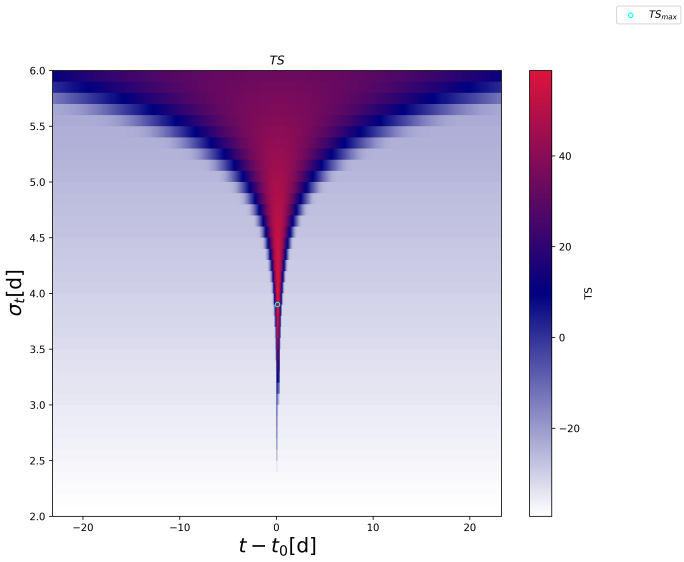

Figure 5.31: TS distribution as a function of $t - t_0$[day] (x-axis) and σ_t[day] (y-axis) in time-dependent search with 4 signal toy MC injected following a Gaussian distribution with mean of t_0 and standard error of 4 d.

5.6.2 p-values

In Section 5.3.1 it is mentioned that distribution of TS at different declination can be different. Now with the trials using sole background events, the expected distribution is shown in Figure 5.32. The pre-trial (or local) p-values are calculated by the fraction of TSs at the same δ obtained from trials with only background toy MC that are larger than the TS calculated from data.

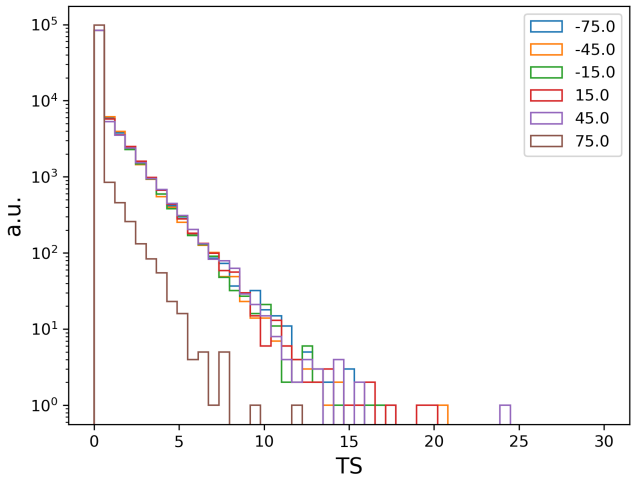

Figure 5.32: TS distribution for time-integrated search using background toy MC at different declinations.

In a trial of full-sky scan, the maximum $-\log p$ (pre-trial) over all searched directions can be found. The post-trial p-value can be calculated by comparing the fraction of $-\log p_{max}$ simulated by background only full-sky scan larger than the $-\log p_{max}$ from data.

5.6.3 Sensitivity

The sensitivity is defined as the number of signal events of which 50% of TS is larger than the 90% of background TS distribution at the same declination[51]. Suppose the TS distribution with n_S signal events at $\delta = 0°$ is $\frac{dP(TS|n_S)}{dTS}$. The median of background TS distribution $\mathrm{TS}^{50\%}(n_S = 0)$ satisfies

$$\int_0^{\mathrm{TS}^{90\%}(n_S=0)} \frac{dP(\mathrm{TS}|n_S=0)}{d\mathrm{TS}} d\mathrm{TS} = 0.9 \tag{5.30}$$

and the 10% quantile of n_S, $\mathrm{TS}^{10\%}(n_S)$ satisfies

$$\int_0^{\mathrm{TS}^{50\%}(n_S)} \frac{dP(\mathrm{TS}|n_S)}{d\mathrm{TS}} d\mathrm{TS} = 0.5 \tag{5.31}$$

then sensitivity $n_S^{90\%\ \mathrm{median}}$ is defined as the value satisfy the following equation:

$$\mathrm{TS}^{50\%}(n_S^{90\%\ \mathrm{median}}) = \mathrm{TS}^{90\%}(n_S = 0) \tag{5.32}$$

These are calculated by running trials using toy MC. Figure 5.33 shows the TS distribution for time-integrated search, ν_μ, at $\delta = 0°$ with 0, 2 and 3 signal toy MC events on top of a set of background toy MC. In these trials the signal toy MC are generated assuming the source is at $\delta = 0°$.

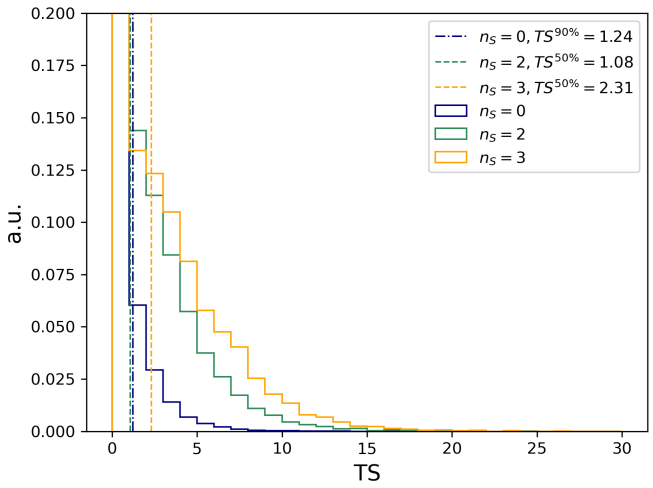

Figure 5.33: TS distribution for time-integrated search using toy MC, with 0 (blue), 2 (green), 3 (orange) signal events on top of background events.

The sensitivity for different declination δ are calculated in the same way, and covert the results to flux by:

$$\Phi_0^{90\%\ \mathrm{median}} = \frac{n_S^{90\%\ \mathrm{median}}}{\sum_j \int_{E_{min}}^{E_{max}} \left(\frac{E}{1\mathrm{GeV}}\right)^{-\gamma} A_{eff}^j(E) dE \cdot T_{total}} \tag{5.33}$$

which is shown in Figure 5.34.

In time-dependent search, the exact time-duration of potential neutrino emission is difficult to define. The fitted σ_t assuming Gaussian time distribution is merely a lower bound of emission duration. Thus the upper limits is given in neutrino fluence (flux

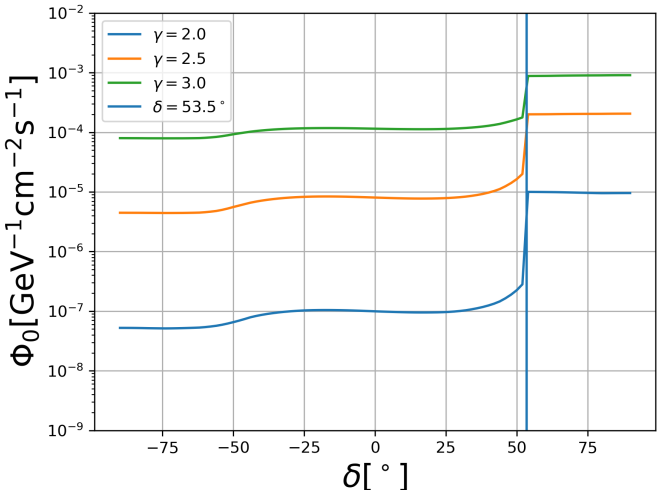

Figure 5.34: Sensitivity in terms of neutrino fluence normalization at 1GeV as a function of declination and γ (blue, orange and green).

integrated over time) with a referral duration of $\hat{\sigma}_t$ centered at $\hat{t}_0$.

$$\mathcal{F}_0^{90\%\text{ median}} = \frac{n_S^{90\%\text{ median}}}{\sum_j \int_{E_{min}}^{E_{max}} \left(\frac{E}{1\mathrm{GeV}}\right)^{-\gamma} A_{eff}^j(E) dE} \tag{5.34}$$

The sensitivity for time-dependent search depends not only on δ, but also burst duration σ_t. Sensitivities as a function of δ for different σ_t are shown in Figure 5.35.

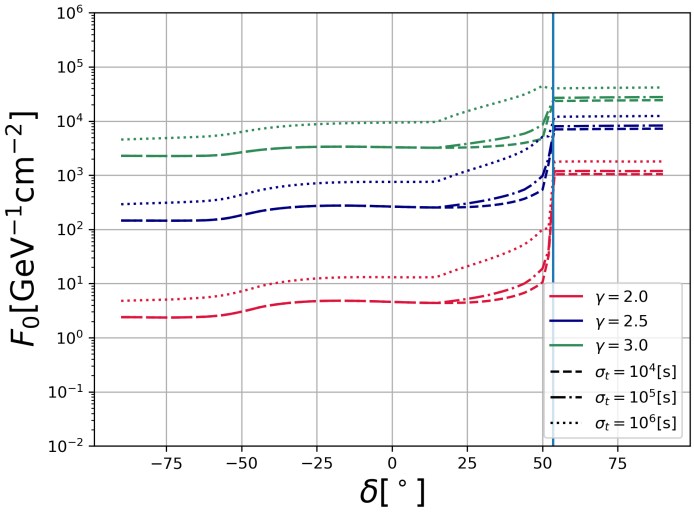

Figure 5.35: Sensitivity in terms of neutrino fluence normalization at 1GeV as a function of declination, γ (red, blue and green) and σ_t (dash, dash-dot and dot).

5.7 Upper Limit

In the case that p-value suggests no significant excess with respect to background fluctuation, a 90% confidence level (CL) upper limit will be calculated from the observed data. The log of likelihood ratio, $-2\log[\mathcal{L}(n_S,\gamma)/\mathcal{L}(\hat{n}_S,\gamma)]$, will approximately follow one-degree freedom chi-square distribution[54], so the 90% CL upper limit in terms of number of signal events, is defined as the $n_S^{90\%\text{C.L.}}$ that satisfies the following equation:

$$-2\log[\mathcal{L}(n_S^{90\%\text{C.L.}},\gamma)/\mathcal{L}(\hat{n}_S,\gamma)] = 2.71 \tag{5.35}$$

Then the number of signal events can be converted to neutrino flux (in time-integrated search)

$$\Phi_0^{90\%\text{C.L.}} = \frac{n_S^{90\%\text{C.L.}}}{\sum_j \int_{E_{min}}^{E_{max}} \left(\frac{E}{1\text{GeV}}\right)^{-\gamma} A_{eff}^j(E)dE \cdot T_{total}} \tag{5.36}$$

or neutrino fluence (in time-dependent search)

$$\mathcal{F}_0 = \frac{n_S^{90\%\text{C.L.}}}{\sum_j \int_{E_{min}}^{E_{max}} \left(\frac{E}{1\text{GeV}}\right)^{-\gamma} A_{eff}^j(E)dE} \tag{5.37}$$

5.8 Systematic Uncertainty

In this analysis, the major physical observable to be measured is neutrino flux normalization for sensitivity, and upper limit. Since the flux normalization can be expressed as

$$\Phi_0 = \frac{n_S}{A_{eff}^{integral} T_{live}} \tag{5.38}$$

where $A_{eff}^{integral} = \sum_j \int_{E_{min}}^{E_{max}} \left(\frac{E}{1\text{GeV}}\right)^{-\gamma} A_{eff}^j(E)dE$, the uncertainty can be estimated by considering uncertainty of n_S and $A_{eff}^{integral}$. The sources of systematic uncertainties and their influence on flux normalization for different searches are different and will be discussed separately.

Point Source Search

In searches for point sources, the number of observed events in data from SK-I to SK-V is used as number of background events in likelihood and toy MC generation. This data-driven approach avoids the uncertainty arise from the uncertainty of atmospheric neutrino flux model. As the result, the systematic uncertainty is dominated by the uncertainty of effective area. The major source of uncertainty for effective area is the uncertainty of the cross section of neutrino interacting with nucleon. According to Ref.[12], the uncertainty is about 10% in the search energy range in this analysis, generating a uncertainty 10%

in the effective area of FC and PC sample.

There is another source of uncertainty for the effective area of UPMU sample from Earth shadow effect, which is discussed in Ref.[51]. UPMU sample is sensitive to neutrinos with energies above 1 TeV. Such high-energy neutrinos can be 'absorbed' by Earth as they penetrate the Earth below horizon. Both CC and NC interaction will reduce neutrino flux, but outgoing ν_μ from NC interaction may still be able to generate UPMU events. The uncertainty from this is estimated as half the difference between the effective area calculated by only taking CC interaction into account and that calculated by taking both CC and NC interaction into account in Earth shadow. By adding the two sources of uncertainty quadratically, the total uncertainty of UPMU effective area is about 11%.

The search for ν_μ point sources used all three samples, yet for the benchmark signal spectrum $\gamma = 2$, contribution of signal events from FC and PC are negligible (Figure 5.12). Thus, the uncertainty of UPMU effective area is the leading uncertainty for sensitivity of search for ν_μ point sources, which in the end is 11%.

The uncertainty of the effective area of FC in the end yields a 10% uncertainty in the sensitivity of the search for the point source of ν_e. However, there is another source of uncertainty that has to be taken into account. The efficiencies of applying the cut to select ν_e events described in Section 5.1 are included in the effective areas shown in Figure 5.11. 55% of the FC events in data passed the selection while 59% in MC passed, which indicates a 7.3% efficiency difference between data and MC. A total uncertainty is estimated to be 12% by adding the two uncertainties quadratically.

Search for ν_e from Galactic Plane & Stacking Galactic Sources

In these two searches, the search region extends to nearly 1/4 of the sky, and contribution of signal events in the data set may not be negligible. As the result, the number of background events (n_B) used in likelihood and toy MC generation is the number of atmospheric neutrino MC events normalized by SK live time. In such case, the uncertainty of atmospheric neutrino flux will have an impact on the uncertainty of $n_S^{90\%\ \text{median}}$ from Equation 5.32.

The dominant source of n_B uncertainty is the uncertainty in atmospheric neutrino flux. The uncertainties for atmospheric neutrino flux are presented in Ref.[46]. Strong correlations in the uncertainties of measured fluxes are seen among energy bins above 10 GeV, as well as between ν_e and ν_μ fluxes, so conservatively the uncertainties are added linearly, which gives a total uncertainty of 13.6%.

The uncertainty that propagate to $n_S^{90\%\ \mathrm{median}}$ from n_B is estimated through trials using the method described in Section 5.6.3, with number of n_B in likelihood and background toy MC generation being varied by $\pm 13.6\%$. The result is estimated to be $n_{S,+}^{90\%\ \mathrm{median}}(n_B \to 113.6\% n_B) = 9.6$ and $n_{S,-}^{90\%\ \mathrm{median}}(-86.4\% n_B) = 8.3$. The change of $n_S^{90\%\ \mathrm{median}}$ as a result of uncertainty in n_B is 6.5%, calculated as the half difference between $n_{S,+}^{90\%\ \mathrm{median}}(n_B \to 113.6\% n_B)$ and $n_{S,-}^{90\%\ \mathrm{median}}(-86.4\% n_B)$. Adding this uncertainty with the 12% uncertainty of effective area quadratically, total uncertainty estimated to be 14%.

Chapter 6

Results

6.1 Time-Integrated Search for ν_μ and ν_e Point Source

6.1.1 Search for ν_μ

Figure 6.1 show the sky maps of $-\log_{10} p$ for the time-integrated search for ν_μ. The best fitted direction is found at right ascension and declination of $(\alpha = 32.3°, \delta = -15.1°)$ in search for ν_μ. Best fitted direction is encircled by a red solid line.

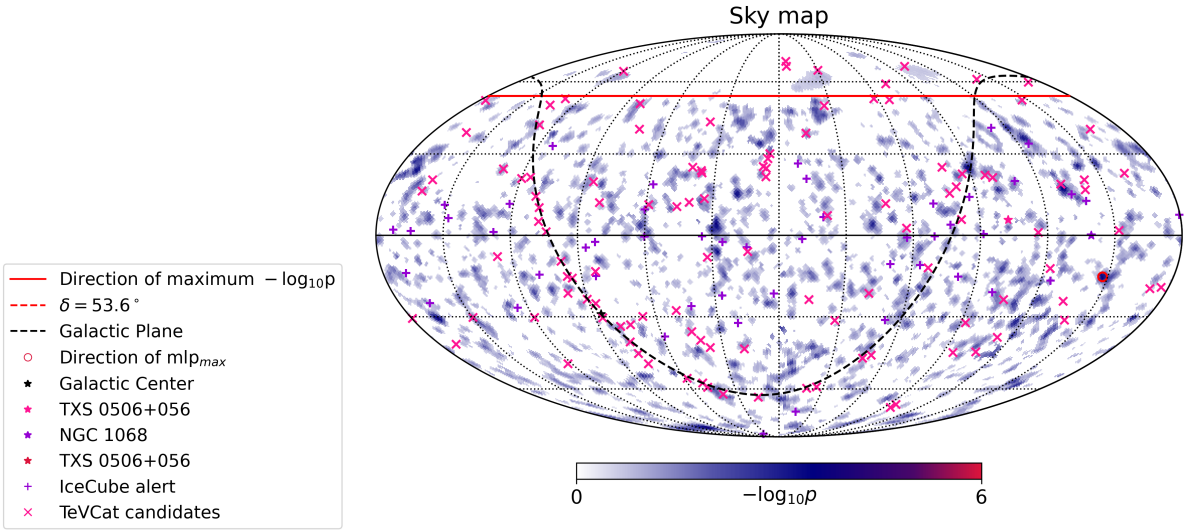

Figure 6.1: Sky map of $-\log_{10} p$ in time-integrated search for ν_μ. The best fitted direction is indicated by red circle, with galactic plane (dashed line), galactic center (black star), TXS 0506+056 (pink star), NGC 1068 (purple star), IceCube high-energy alerts (purple plus), TeVCat candidates (pink cross) and $\delta = 53.6°$ (dashed line).

Figure 6.2 show the event spatial distributions around the best fitted direction. Thirteen UPMU events are found to contribute most of TS around the best fitted direction in the search for ν_μ. The gray markers without circles surrounding are events other than

those 13 events.

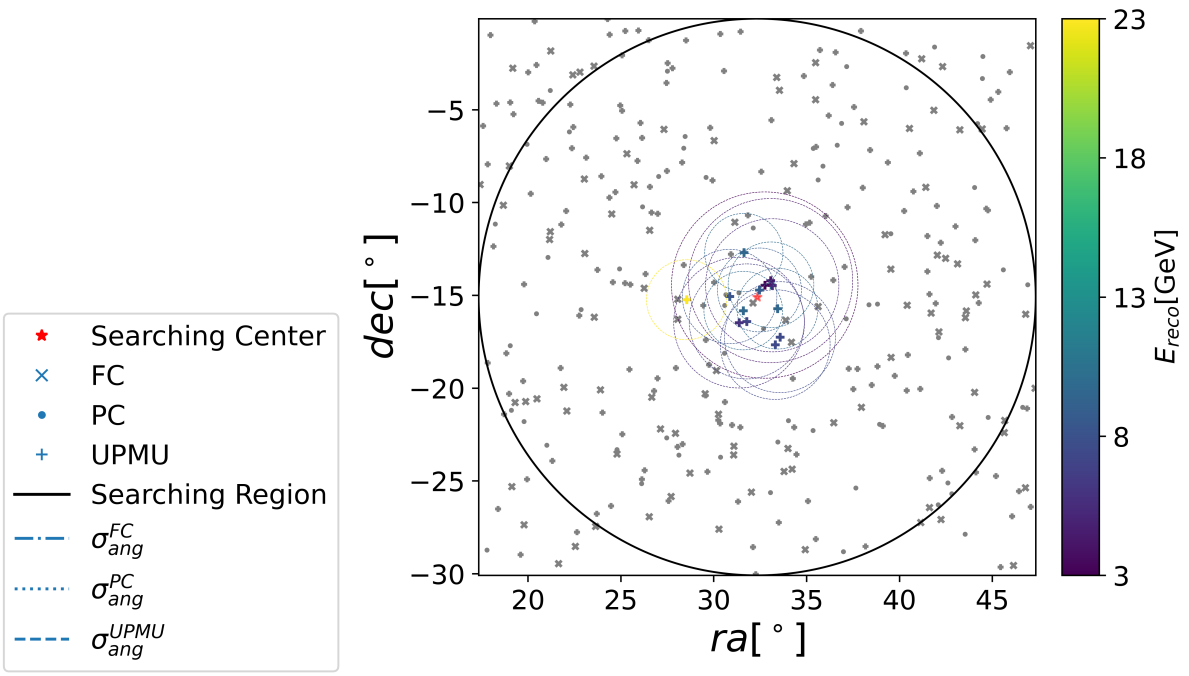

Figure 6.2: Events spatial distribution around the best fitted direction in time-integrated search for ν_μ. Colored events are events which have top 13 contribution to the TS. Cross, dot and plus markers are direction of FC, PC and UPMU events. Dash-dotted, dotted and dashed circles indicate the angular resolution of FC, PC and UPMU event, respectively. Color of marker and circle represent energy of the event. Red star is the best fitted direction, and the black solid circle is the 15° search region boundary.

Figure 6.3 shows the TS distribution of data compared to the results of trials using toy MC of time-integrated search for ν_μ. Although data has a slight downward fluctuation for TS above around 3, the distribution basically agrees with MC. The minimum pre-trial p-value is 1.3×10^{-4}, corresponding to a post-trial p value of 87.8%. Maximum $-\log_{10} p$ in data and the distribution obtained from trials are presented in Figure 6.4.

No significant excess with respect to background was found in the time-integrated search for ν_μ according to the p values, so 90% confidence level upper limit was set on the neutrino flux normalization, assuming $\gamma = 2$, to $\Phi^{90\mathrm{CL}} = 4.0 \times 10^{-7}[\mathrm{GeV}^{-1}\mathrm{cm}^{-2}\mathrm{s}^{-1}]$ at 1 GeV. The results are summarized in Table 6.1.

As other directions are even less significant than hottest spot, upper limits on neutrino fluxes are calculated in the same way as in hottest spot for every search direction, as shown in Figure 6.5. There is a clear bound for flux upper limits above and below $\delta = 53.6°$, which is due to the difference between effective area between UPMU and FC/PC events.

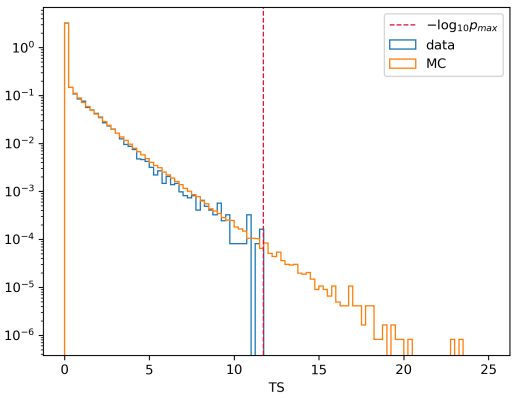

Figure 6.3: Comparison of distribution of TS from data (blue) and MC (orange) in time-integrated search for ν_μ. $-\log_{10} p_{max}$ from data indicated by dashed red line.

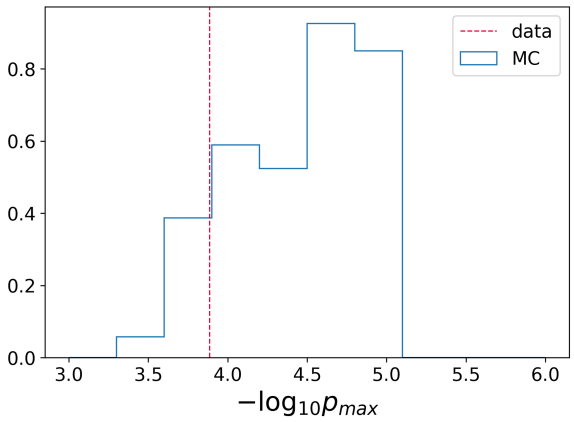

Figure 6.4: Distribution of $-\log_{10} p_{max}$ from full sky with MC in time-integrated search for ν_μ. $-\log_{10} p_{max}$ from data indicated by dashed red line.

Table 6.1: Best fitted number of events $\hat{n}_S$, energy spectrum index $\hat{\gamma}$, right ascension $\hat{\alpha}$ and declination $\hat{\delta}$, pre-trial p-value, post-trial p-value and neutrino flux normalization upper limit $\Phi_0^{90\text{CL}}$ assuming $\gamma = 2$ at 1 GeV in the time-integrated searches for ν_μ.

	$\hat{n}_S$	$\hat{\gamma}$	$\hat{\alpha}$ [°]	δ [°]	pre p	post p	$\Phi_0^{90\text{CL}}$ [GeV^{-1}cm^{-2}s^{-1}]
ν_μ	13.3	2.6	32.3	-15.1	1.3×10^{-4}	87.8%	4.0×10^{-7}

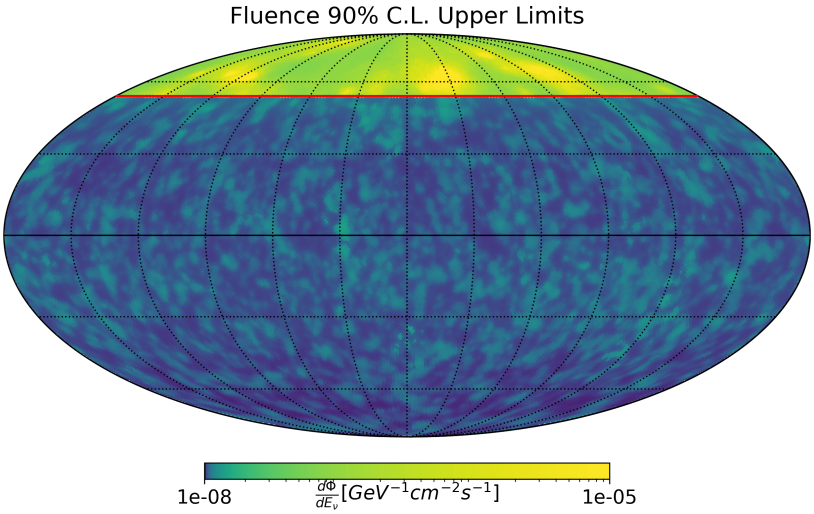

Figure 6.5: Neutrino flux normalization upper limit normalization at 1 GeV assuming $\gamma = 2$ of time-integrated search for ν_μ. Color map is in log scale. $\delta = 53.6°$ indicated by red solid line.

Figure 6.6 shows the 90% C.L. upper limits at 1 GeV assuming $\gamma = 2$ at the search directions of candidates, together with sensitivity, as a function of declination for time-integrated search for ν_μ. Details of the result for each candidate are listed in Table A.1 Table A.2 in Appendix A.

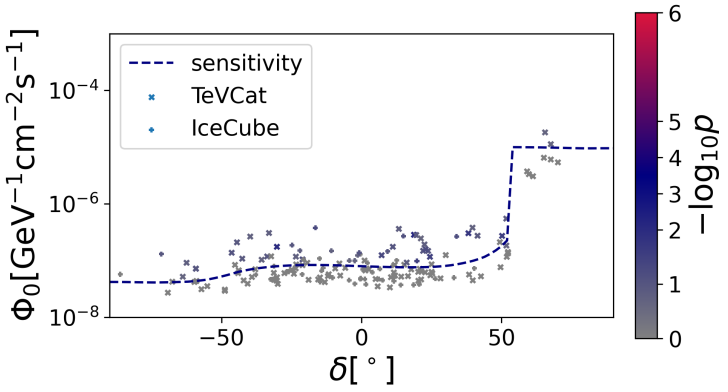

Figure 6.6: 90% CL neutrino flux normalization upper limits at 1 GeV assuming $\gamma = 2$ at directions of IceCube triggers (plus) and TeVCat candidates (cross), with sensitivity (dashed line) as a function of declination. Results are from time-integrated search for ν_μ. Color of the marker corresponds to p-value.

6.1.2 Search for ν_e

Figure 6.7 show the sky maps of $-\log_{10} p$ for the time-integrated search for ν_e. The best fitted direction are found at right ascension and declination of $(\alpha = 48.5°, \delta = 8.4°)$ in search for ν_e.

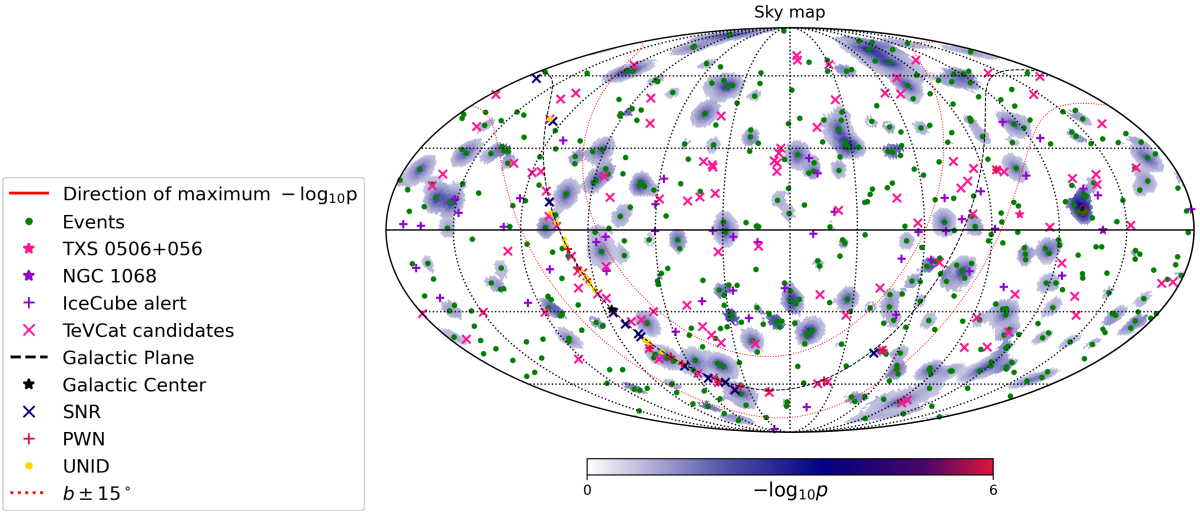

Figure 6.7: Sky map of $-\log_{10} p$ in time-integrated search for ν_e. The best fitted direction is indicated by red circle, with galactic plane (black dashed line), galactic center (black star), $|b| < 15°$ region (red dotted lines), TXS 0506+056 (pink star), NGC 1068 (purple star), IceCube high-energy alerts (purple plus), TeVCat candidates (pink cross), SNR (blue cross), PWN (red plus) and UNID (yellow dot) in galaxy, and events in SK data (green dot).

Figure 6.8 show the event spatial distributions around the best fitted direction. Six events are found to contribute most of TS around the best fitted direction in the search for ν_e. The gray markers without circles surrounding are events other than those 6 events.

Figure 6.3 shows the TS distribution of data compared to the results of MC of the time-integrated search for ν_e. The data TS distribution agrees with MC. The minimum pre-trial p values is 3.7×10^{-4} for the search for ν_e, corresponding to a post-trial p value of 72.6%. Maximum $-\log_{10} p$ in data and the distribution obtained from trials are presented in Figure 6.10.

No significant excess with respect to background was found in the time-integrated search for ν_e according to the p values, so 90% confidence level upper limit assuming $\gamma = 2$ was set on the neutrino flux normalization to $\Phi^{90\mathrm{CL}} = 1.8 \times 10^{-7} [\mathrm{GeV}^{-1}\mathrm{cm}^{-2}\mathrm{s}^{-1}]$ at 10 GeV. The results are summarized in Table 6.2.

Upper limits on neutrino flux normalizations at 10 GeV are calculated assuming $\gamma = 2$

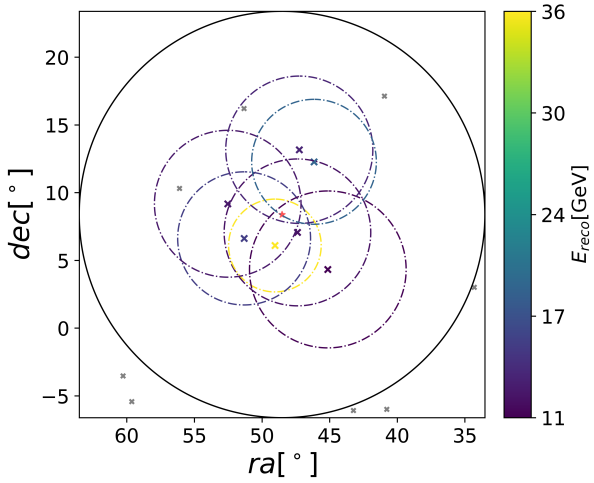

Figure 6.8: Events spatial distribution around the best fitted direction in time-integrated search for ν_e. Colored events are events which have top 6 contribution to the TS. Cross, dot and plus markers are direction of FC, PC and UPMU events. Dash-dotted, dotted and dashed circles indicate the angular resolution of FC, PC and UPMU event, respectively. Color of marker and circle represent energy of the event. Red star is the best fitted direction, and the black solid circle is the 15° search region boundary. See Figure 6.2 for legends.

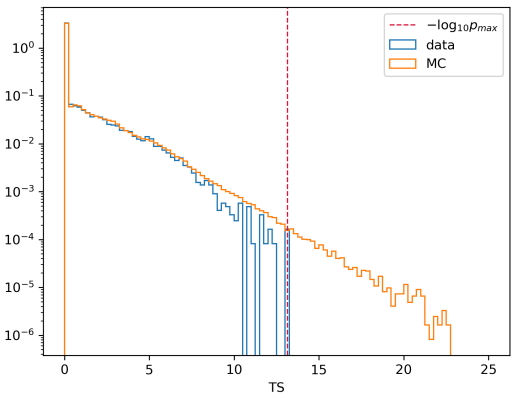

Figure 6.9: Comparison of distribution of TS from data (blue) and MC (orange) in time-integrated search for ν_e. $-\log_{10} p_{max}$ from data indicated by dashed red line.

Table 6.2: Best fitted number of events $\hat{n}_S$, energy spectrum index $\hat{\gamma}$, right ascension $\hat{\alpha}$ and declination $\hat{\delta}$, pre-trial p-value, post-trial p-value and neutrino flux normalization upper limit $\Phi_0^{90\mathrm{CL}}$ assuming $\gamma = 2$ at 10 GeV in the time-integrated searches for ν_e.

	$\hat{n}_S$	$\hat{\gamma}$	$\hat{\alpha}$ [°]	δ [°]	pre p	post p	$\Phi_0^{90\mathrm{CL}}$ [$\mathrm{GeV}^{-1}\mathrm{cm}^2\mathrm{s}^1$]
ν_e	6.4	4.0	48.5	8.4	3.7×10^{-4}	72.6%	1.8×10^{-7}

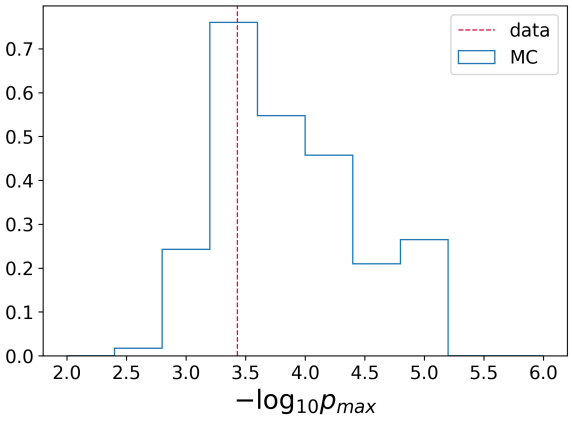

Figure 6.10: Distribution of $-\log_{10} p_{max}$ from full sky with MC in time-integrated search for ν_μ. $-\log_{10} p_{max}$ from data indicated by dashed red line.

for every search direction, as shown in Figure 6.11.

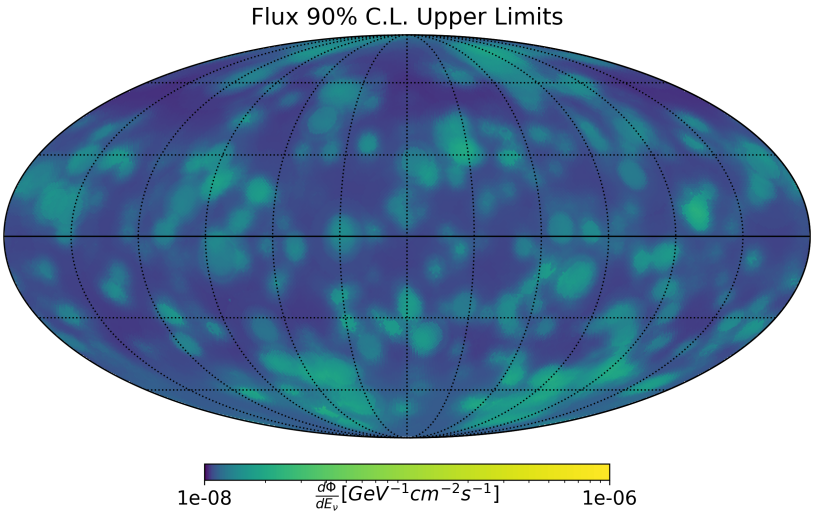

Figure 6.11: Neutrino flux normalization upper limit normalization at 10 GeV assuming $\gamma = 2$ of time-integrated search for ν_e. Color map is in log scale.

Figure 6.12 shows the 90% C.L. upper limits at 10 GeV assuming $\gamma = 2$ at the search directions of candidates, together with sensitivity, as a function of declination for time-integrated search for ν_μ. Details of the result for each candidate are listed in Table A.1 Table A.2 in Appendix A.

In addition, the searches at the directions of stacked sources are also performed in time-integrated search for ν_e. 90% C.L. upper limits at 10 GeV assuming $\gamma = 2$ at the search directions of candidates, together with sensitivity, vs declination are presented in Figure 6.13. Table 6.3 lists name, location, fitted number of signal events, flux normalization upper limits at 10 GeV assuming $\gamma = 2$ and p-value of the search with these sources.

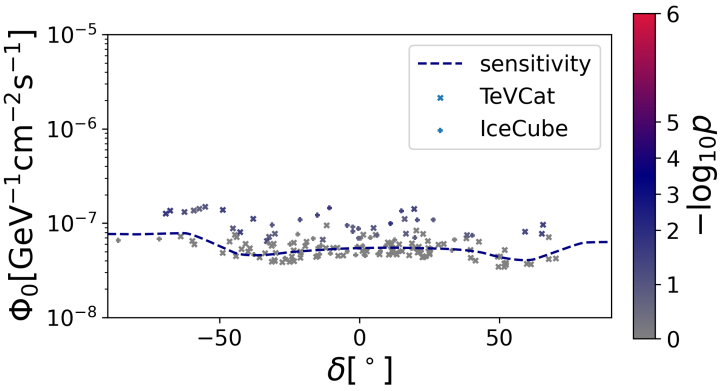

Figure 6.12: 90% CL neutrino flux normalization upper limits at 10 GeV assuming $\gamma = 2$ at directions of IceCube triggers (plus) and TeVCat candidates (cross), with sensitivity (dashed line) as a function of declination. Results are from time-integrated search for ν_e. Color of the marker corresponds to p-value.

Table 6.3: Name, right ascension (α), declination (δ), best fitted number of signal events $\hat{n}_S$, 90% C.L. flux normalization upper limits at 10 GeV ($\Phi_0^{90\%}[\times 10^{-8}\mathrm{GeV}^{-1}\mathrm{cm}^{-2}\mathrm{s}^{-1}]$) assuming $\gamma = 2$, and p-value, for SNR, PWN and UNID in time-integrated search for ν_e.

Type	Name	$\alpha[^\circ]$	$\delta[^\circ]$	$\hat{n}_S$	$\Phi_0^{90\%\mathrm{C.L.}}$	p
SNR	Vela Junior	133.0	-46.3	0.0	6.4	-
	RX J1713.7-3946	258.4	-39.8	0.0	5.0	-
	HESS J1614-518	243.6	-51.8	1.8	13.7	0.13
	HESS J1457-593	223.7	-59.1	0.6	13.4	0.19
	SNR G323.7-01.0	233.6	-57.2	0.0	12.6	-
	HESS J1731-347	263.0	-34.7	0.0	4.2	-
	Gamma Cygni	305.3	40.5	0.0	4.2	-
	RCW 86	220.1	-62.7	1.1	13.2	0.035
	HESS J1912+101	288.3	10.2	0.0	6.2	-
	HESS J1745-303	266.3	-30.2	0.0	4.1	-
	Cassiopeia A	350.9	58.8	0.0	3.5	-
	CTB 37A	258.6	-38.5	0.0	4.9	-
PWN	Vela X	128.3	-45.2	1.4	8.5	0.14
	Crab nebula	83.6	22.0	0.0	5.2	-
	HESS J1708-443	257.0	-44.3	0.0	7.3	-
	HESS J1825-137	276.6	-13.6	0.0	4.7	-
	HESS J1632-478	248.0	-47.9	1.4	11.6	0.030
	MSH 15-52	228.5	-59.2	0.4	13.6	0.20
	HESS J1813-178	273.4	-17.9	0.0	4.2	-
	HESS J1303-631	195.8	-63.2	0.0	7.0	-
	HESS J1616-508	244.1	-50.9	2.1	14.0	0.10
	HESS J1418-609	214.7	-61.0	1.0	11.8	0.10
	HESS J1837-069	279.4	-6.9	0.0	5.7	-
	HESS J1026-582	157.2	-58.3	0.0	6.0	-
UNID	MGRO J1908+06	286.9	6.3	0.4	8.5	0.17
	Westerlund 1	251.5	-45.8	1.1	10.1	0.070
	HESS J1702-420	255.7	-42.0	0.0	6.4	-
	2HWC J1814-173	273.5	-17.3	0.0	4.3	-
	HESS J1841-055	280.2	-5.6	0.0	5.7	-
	2HWC J1819-150	274.8	-15.1	0.0	4.4	-
	HESS J1804-216	271.1	-21.7	0.0	4.0	-
	HESS J1809-193	272.6	-19.3	0.0	4.1	-
	HESS J1843-033	280.8	-3.3	0.0	5.3	-
	TeV J2032+4130	307.9	41.5	0.0	4.0	-
	HESS J1708-410	257.1	-41.1	0.0	5.7	-
	HESS J1857+026	284.3	2.7	0.0	7.5	-

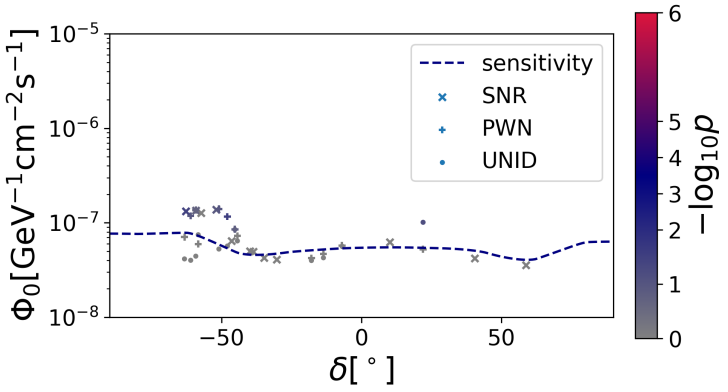

Figure 6.13: 90% CL neutrino flux normalization upper limits at 10 GeV assuming $\gamma = 2$ at directions of SNR (plus), PWN candidates (cross) and UNID (dot), with sensitivity (dashed line) as a function of declination. Results are from time-integrated search for ν_e. Color of the marker corresponds to p-value.

6.2 Time-Dependent Search for Point Source

The sky map of $-\log_{10} p$ is shown in Figure 6.14 for the time-dependent search. Directions with none 0 $\hat{n}_S$ but TS smaller than $-\log 2$ are clipped, as they are not of interest. The best fitted direction are found at $(\alpha = 111.8°, \delta = 15.7°)$, and the best fitted emission center times are $t_0 = 50927.7$ mjd.

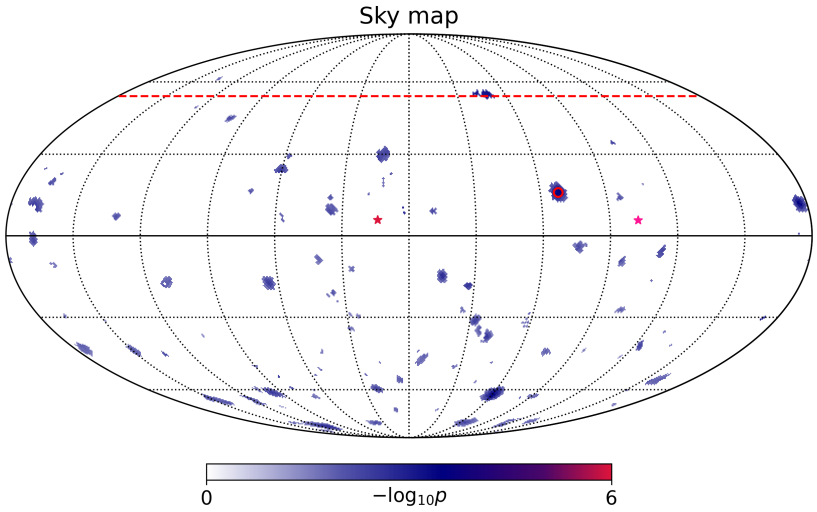

Figure 6.14: Sky map of $-\log_{10} p$ in time-dependent search. The best fitted direction is indicated by red circle, with TXS 0506+056 (pink star), 3C 279 (red star), and $\delta = 53.6°$ (dashed line). See Figure 6.1 for legend.

Figure 6.15 and Figure 6.16 show the event spatial and temporal distributions around the best fitted direction within $\hat{t}_0 \pm 3\hat{\sigma}_t$. Two UPMU events are found around the best fitted direction and best fitted emission center time within ±580s in the time-dependent search.

Figure 6.17 shows the TS distribution of data compared to the results of MC of the time-dependent search. The data TS distribution agrees with MC. The minimum pre-trial p-value of the best fitted direction in the search for ν_μ is 2.0×10^{-4}, corresponding to a post-trial p value of 68.4%.. Maximum $-\log_{10} p$ in data and the distribution obtained from trials are presented in Figure 6.18.

No significant excess with respect to background in time-dependent search was found according to the p-value, and the 90% confidence level neutrino fluence normalization upper limits was set to $F^{90\mathrm{CL}} = 11.6[\mathrm{GeV}^{-1}\mathrm{cm}^{-2}]$ at 1 GeV, assuming $\gamma = 2$. The result of this search is summarized in Table 6.4.

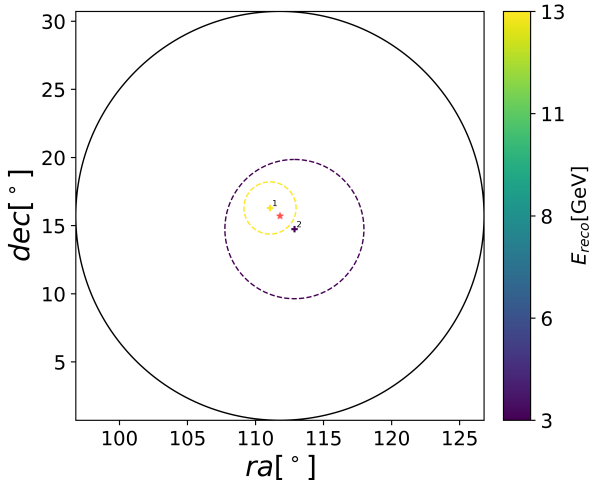

Figure 6.15: Events spatial distribution around the best fitted direction and the best fitted center of time in time-dependent search. Cross, dot and plus markers are direction of FC, PC and UPMU events. Dashed, dash-dotted and dotted circles indicate the angular resolution of FC, PC and UPMU event, respectively. Color of marker and circle represent energy of the event. Red star is the best fitted direction, and the black solid circle is the 15° search region boundary. See Figure 6.2 for legends.

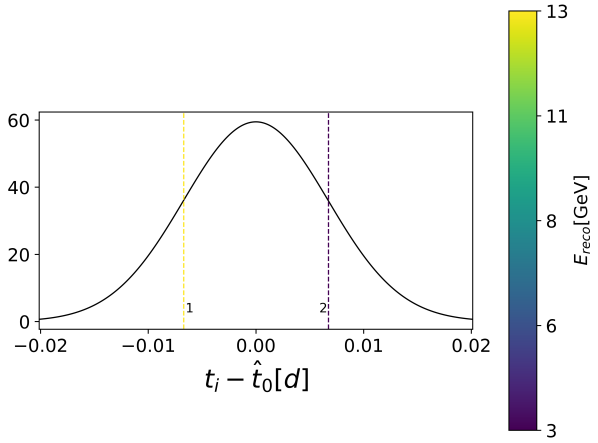

Figure 6.16: Events time distribution around the best fitted direction and the best fitted center of time in time-dependent search. Dash-dotted, dotted and dashed vertical lines are detection time relative to $\hat{t}_0$ of FC, PC and UPMU events, respectively. Color of lines represent energy of the event. The black line indicate the Gaussian distribution given $\hat{t}_0$ and $\hat{\sigma}_t$.

Table 6.4: Best fitted number of events $\hat{n}_S$, energy spectrum index $\hat{\gamma}$, right ascension $\hat{\alpha}$ and declination $\hat{\delta}$, pre-trial p-value, post-trial p-value and neutrino fluence normalization upper limit $\mathcal{F}_0^{90\mathrm{CL}}$ assuming $\gamma = 2$ at 1 GeV in the time-integrated searches for ν_μ.

$\hat{n}_S$	$\hat{\gamma}$	$\hat{\sigma}_t$ [s]	$\hat{t}_0$ [mjd]	$\hat{\alpha}$ [°]	δ [°]	pre p	post p	$\mathcal{F}_0^{90\mathrm{CL}}$ [$\mathrm{GeV}^{-1}\mathrm{cm}^{-2}$]
2.0	2.0	579.7	50927.8	111.8	15.7	2.0×10^{-4}	68.4%	11.6

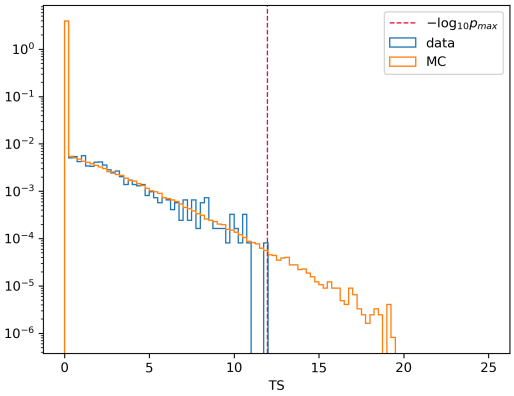

Figure 6.17: Comparison of distribution of TS from data (blue) and MC (orange) in time-dependent search. $-\log_{10} p_{max}$ from data indicated by dashed red line.

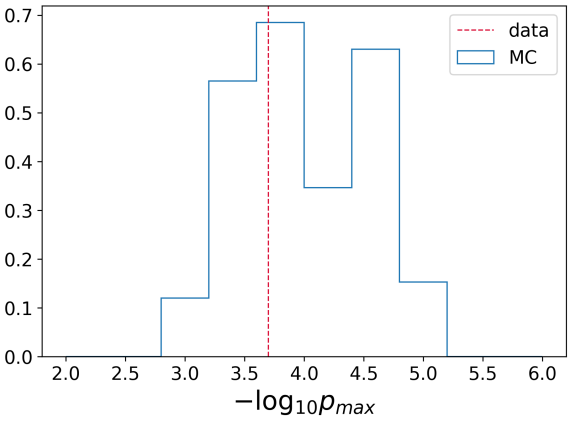

Figure 6.18: Distribution of $-\log_{10} p_{max}$ from full sky with MC in time-dependent search. $-\log_{10} p_{max}$ from data indicated by dashed red line.

Figure 6.19 and Figure 6.20 show the 90% C.L. upper limits of neutrino fluence normalization at 1 GeV assuming $\gamma = 2$, and corresponding $\hat{\sigma}_t$ at directions where the TS is larger than $-\log 2$.

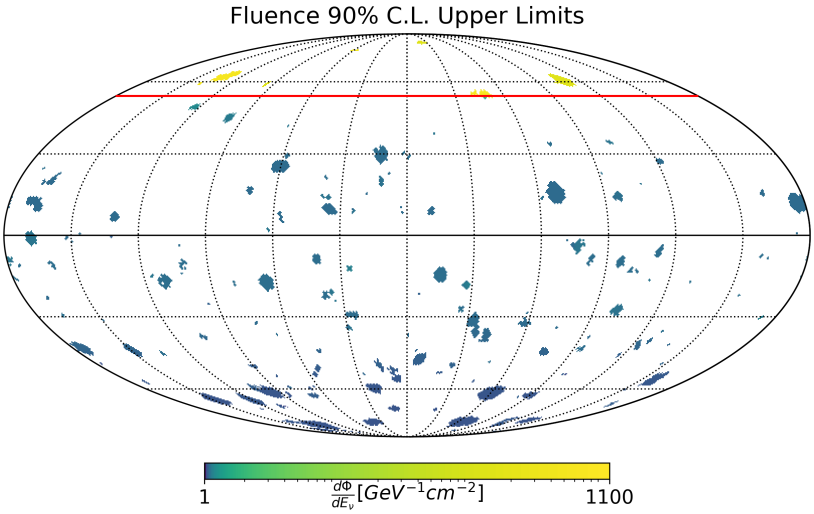

Figure 6.19: Neutrino fluence normalization upper limit normalization at 1 GeV assuming $\gamma = 2$ of time-dependent search. Color map is in log scale. $\delta = 53.6°$ indicated by red solid line.

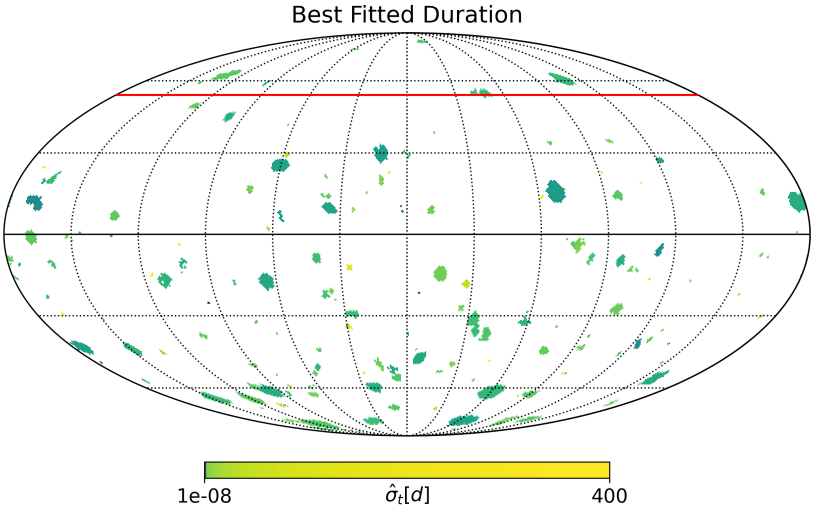

Figure 6.20: Best fitted time duration $\hat{\sigma}_t$ of time-dependent search. Color map is in log scale. $\delta = 53.6°$ indicated by red solid line.

6.3 Search for Diffuse ν_e from Galactic Plane

The number of signal events in search for ν_e from galactic plane is fitted to 0, which means no excess of events were found in the search with SK data in the $|b| < 15°$ galactic plane region according to π^0 model sky template. 90% CL neutrino flux normalization upper limit at 10 GeV is calculated assuming $\gamma = 2.7$. The results are summarized in Table 6.5.

Table 6.5: Results of search for diffuse ν_e from galactic plane. Best fitted number of signal events, 90 CL upper limit in terms of number of signal event as well as in terms of neutrino flux normalization at 10 GeV with $\gamma = 2.7$ are listed.

$\hat{n}_S$	p	$n_S^{C.L.90}$	$\Phi_0^{90\%CL}(E_\nu = 10\text{GeV})[\text{GeV}^{-1}\text{cm}^{-2}\text{s}^{-1}]$
0.0	-	9.8	7.5×10^{-7}

The data event distribution in the $|b| < 15°$ region with the probability density of the expected signal event distribution from the spatial template of the π^0 model is shown in Figure 6.21. There are not many data overlapped with expected region, which explains the result $\hat{n}_S = 0$.

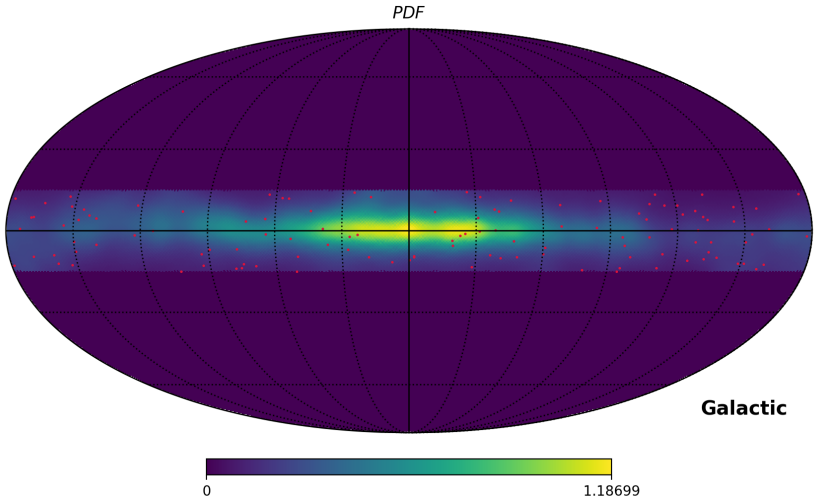

Figure 6.21: Data event distribution (red dot) compared with spatial PDF from smeared π^0 model spatial template in $|b| < 15°$

Flux upper limit and sensitivity in terms of neutrino flux of search for ν_e from galactic plane is shown in Figure 6.22, comparing with the prediction from π^0 model.

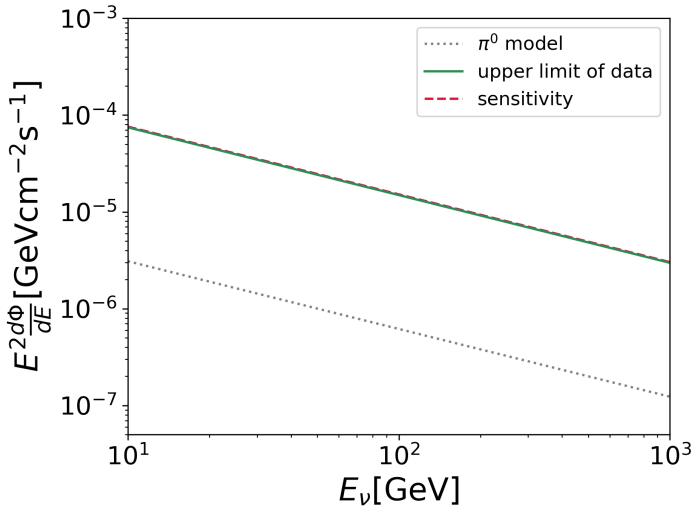

Figure 6.22: E_ν^2 times neutrino flux normalization of 90% CL upper limit (green solid) and sensitivity (red dashed) from search for ν_e from galactic plane, together with π^0 model prediction, against E_ν.

6.4 Stacked Search for ν_e from Sources in Galaxy

No significant excess was found in the stacking search of the 12 SNR, PWN or UNID sources with SK data. The results of stacked search for ν_e from sources in galaxy are listed in Table 6.6.

Table 6.6: Results of stacked search for ν_e from sources in galaxy. Best fitted number of signal events, 90 CL upper limit in terms of number of signal event as well as in terms of neutrino flux normalization at 10 GeV with $\gamma = 2.7$ for SNR, PWN and UNID are listed.

Type	$\hat{n}_S$	p	$n_S^{C.L.90}$	$\Phi_0^{90\%CL}(E_\nu = 10\text{GeV})[\text{GeV}^{-1}\text{cm}^{-2}\text{s}^{-1}]$
SNR	0.0	-	5.0	3.7×10^{-7}
PWN	1.5	0.28	8.1	6.3×10^{-7}
UNID	0.0	-	3.5	2.7×10^{-7}

The data event distribution in the $|b| < 15°$ region with the locations the SNR, PWN and UNID sources used in stacked search are shown in Figure 6.23. The reason why in all three searches $\hat{n}_S = 0$ is that the distribution of events does not coincide with the source locations.

Flux upper limits and sensitivities in terms of neutrino flux of stacked search for ν_e from three source populations are shown in Figure 6.24.

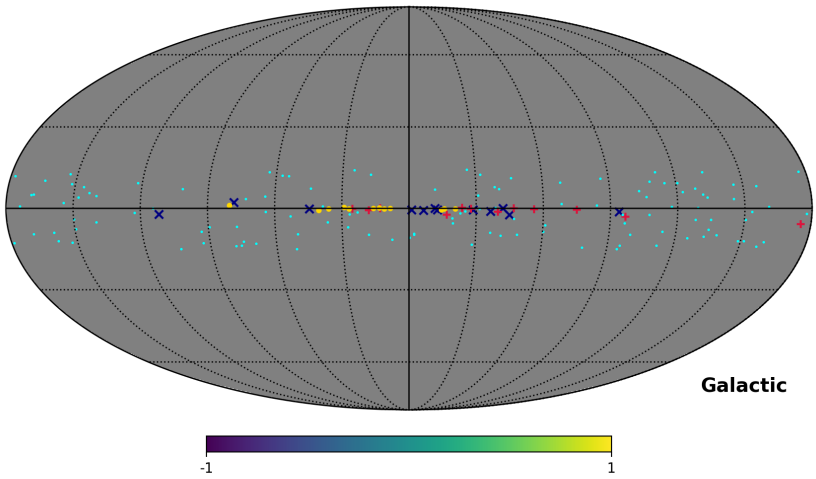

Figure 6.23: Data event distribution (cyan dot) compared with location of SNR (blue cross), PWN (red plus) and UNID (yellow circle) sources, in $|b| < 15°$

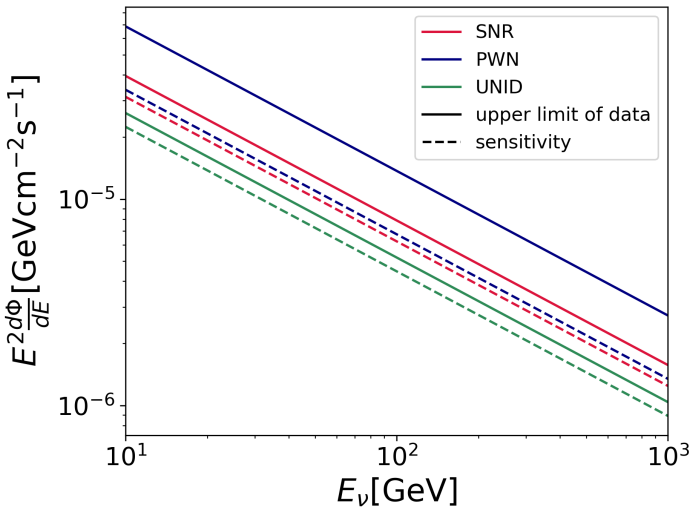

Figure 6.24: E_ν^2 times neutrino flux normalization of 90% CL upper limit (solid) and sensitivity (dashed) from stacked search for ν_e from SNR (rad), PWN (blue) and UNID (green) in galaxy.

Chapter 7

Discussion

7.1 Implications of Full-Sky Scan

In time-integrated full-sky scan for point sources, even the hottest spot has a post-trial p-value of 88.4%, suggesting no significant excess was found in any search direction without a prior. There is no coincidence in direction with any source candidates that are searched with either. The hottest candidate in both ν_e and ν_μ search is RBS0413, with a p-value of 0.54%, less than 3σ. At the direction of NGC 1068, $\hat{n}_S = 0$ in both ν_e and ν_μ search. There is no correlation found between the hottest spots in search for ν_μ and ν_e either.

The full-sky scan for time-dependent search also shows no significant excess with respect to background fluctuation. The hottest spot corresponds to 2 UPMU events with detection time interval shorter than 1200 s. The direction and time of the best fitted result does not match any candidates that are searched with in this analysis. The direction of TXS 0506+056 shows not excess. Beside the steady source of high-energy gamma ray listed in the source candidates in time-integrated search, a transient flare is also of great interest. Although blazar 3C 279 has been observed in multi-wavelength gamma ray observations, a flare during about one day from it marks one of the ever observed highest luminosity. The direction of 3C 279 is marked with red star in Figure 6.14. In the time-dependent search, no significant excess from that direction was found. This is the first time to perform time-dependent search with SK data.

7.2 Constraints on Source Models

As discussed in Section 1.2, hadronic process of cosmic ray interactions produce $\pi^\pm$ and π^0 simultaneously, and $\pi^\pm$ and π^0 decay into neutrino and gamma ray, respectively. This means there should be some connection between gamma ray and neutrino observation.

In Section 6.1, neutrino upper limits have be constrained for source candidate directions and full-sky scan search directions. From these results, further constraints can be set to the models of sources with high energy gamma ray observations. In this section four SNRs and two PWNs of the most interest are analyzed.

To constrain the source model, the 90% CL upper limit of neutrino flux normalization at minimum energy of that search in the source direction is calculated using the method describe in Section 5.7, assuming the energy spectrum is the same as the model. The effective area of SK at different energies is taken into account. Then the flux normalization times flux energy spectrum from the model is compared to the neutrino flux from model prediction in the same energy range of that search.

7.2.1 Constrain on SNR

The SNRs that selected are RX J1713.7-3946, RX J0852.0-4622, W28 and IC443. These sources have strong gamma ray flux in TeV region. The prediction models for RX J1713.7-3946, RX J0852.0-4622 are from Ref. [25] while thos for W28 and IC443 are from Ref. [31].
For the models in Ref. [25], the spectrum of neutrino and gamma ray are the same, and the normalization satisfy $\kappa_\nu = K\kappa_\gamma$. The prediction also assumes all gamma ray flux in the energy range are from hadronic process, and no $p\gamma$ interaction in the hadronic process. Spectral indices for these two sources are harder (1.72 and 1.78), and cut off are set to 1.35 TeV and 1.19 TeV.

In Ref. [31], more complicated lepto-hadronic models are constructed from MeV to TeV range by taking into account contributions from synchrotron radiation, bremsstrahlung and inverse Compton scattering in the gamma ray emission. But in the energy range from 1 GeV to 100 TeV, the models almost follow a power law spectrum with a cutoff at very high energy.

The neutrino flux from model prediction and 90% upper limit of search for ν_μ and ν_e for these four sources are shown in Figure 7.1. The ν_μ flux upper limit is two to three orders of magnitude higher than the model prediction, and ν_e flux is even one more order higher due to the small affective area. These upper limits are set in a lower energy range from 1 GeV to 100 TeV, some of which is not covered by larger neutrino observatories including IceCube.

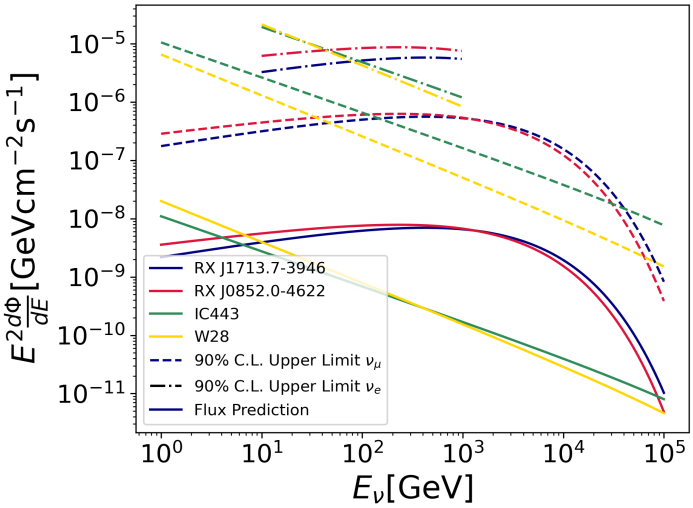

Figure 7.1: Model predicted muon neutrino fluxes (solid) and 90% C.L. ν_μ (dashed) and ν_e (dash-dotted) flux upper limits from this analysis assuming the same spectrum as prediction.

7.2.2 Constrain on PWN

In this analysis two of the top interesting sources are analysis: Crab Nebula and Vela X (also called Vela pulsar). The models to analysis with is also from Ref. [25].

The results are shown in Figure 7.2. The ν_μ 90% upper limits are still more than one order of magnitude higher than model prediction. For Crab Nebula, ν_e upper limit is only about one order magnitude higher than ν_μ, but in the case of Vela X the difference becomes almost three orders of magnitude because of the hard spectrum. The upper limits set in this analysis covers the energy range from 1 GeV to 100 TeV, and compensate the energy range that IceCube is sensitive to.

7.3 Constraint on Search for Diffuse ν_e from Galactic Plane

In Section 6.3, the result of search for diffuse ν_e from Galactic Plane gives 0 fitted number of signal events. The flux upper limit is about one order of magnitude higher than the π^0 model prediction from Ref. [1]. The result from IceCube in Ref. [21] shows a higher flux compared with this π^0 model prediction in TeV range. However, this results agrees with the observation by ARGO-YBJ[3] and Tibet[52] observation of high-energy gamma rays from Galactic Plane. The sensitive region of Tibet and ARGO-YBJ is $|b| < 5°$ and $25° < l < 100°$. To convert to the flux in the galactic plane of $|b| < 15°$, the spatial distribution of observed data from Ferimi-DGE[10] (Figure 7.3) is used, with which the

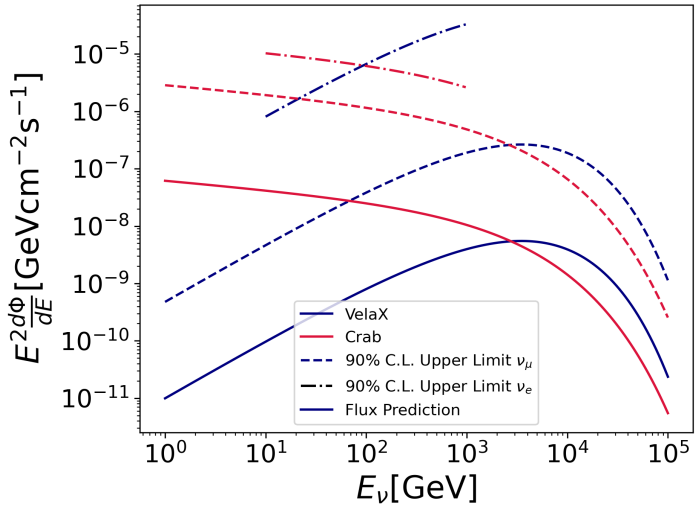

Figure 7.2: Model predicted muon neutrino fluxes (solid) and 90% C.L. ν_μ (dashed) and ν_e (dash-dotted) flux upper limits from this analysis assuming the same spectrum as prediction.

spacial distribution observed by ARGO-YBJ agrees[3]. The neutrino flux spectrum is assumed to be the same as the gamma ray spectrum, and the flux normalization of neutrino is 1/2 of the gamma ray flux from Ref. [52]. Figure 7.4 shows the comparison between 90% upper limit of this analysis, π^0 model prediction. The 90% CL flux upper limit of this search is about 1 order of magnitude higher than either model. This is the first constraint on diffuse ν_e flux from galactic plane in the energy range from 10 GeV to 1 TeV.

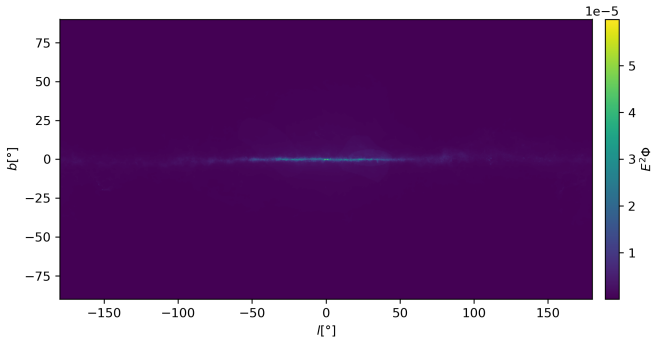

Figure 7.3: Spacial distribution of gamma ray observation from 30 MeV to from Fermi-DGE. Reproduced from Ref.[10].

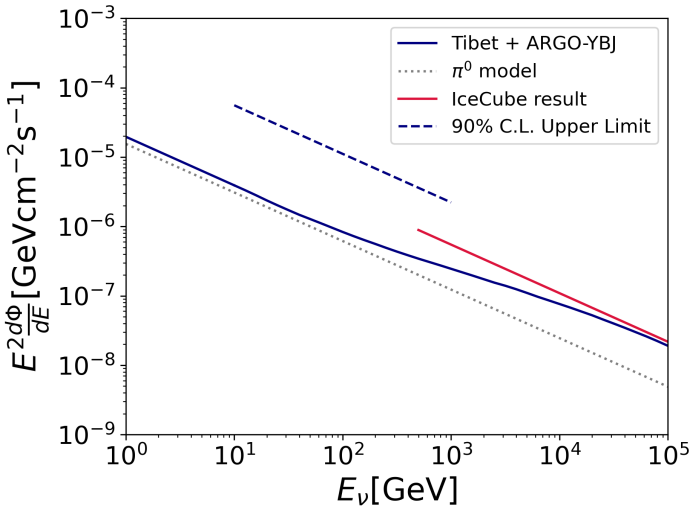

Figure 7.4: Comparison between 90% C.L. upper limits of search for diffuse ν_e from Galactic Plane in this analysis (blue dashed), π^0 model prediction from Ref.[1] (gray dotted) and prediction based on high-energy gamma ray observation by Tibet[52] and ARGO-YBJ[3] (glue solid). Result from IceCube[21] is also shown (red solid).

7.4 Constraint on Stacked Search for ν_e from SNRs in Galaxy

As discussed in Section 1.3.4, a fraction of diffuse neutrino flux in galactic plane can originate from SNRs in the galaxy. In Ref.[31], models are established to connect gamma ray observation of SNR in the galaxy with neutrino flux from SNRs. The paper analyzed 21 SNR sources in detail, and established models to predict total neutrino flux spectrum from these sources. Then, using the fraction of radio observation between the 21 analyzed sources and 243 unresolved sources in galaxy, the neutrino flux spectrum from all SNR in the Galaxy is estimated assuming similar spectra. The estimated unresolved SNR flux is about 1.5 of the resolved 21 sources. Although the sources selected in this stacked search are different, they are still part of the unresolved sources. In Figure 7.5, a comparison between the predicted unresolved neutrino flux from SNR in Galaxy and the 90% C.L. upper limits of stacked search for SNR is presented. The 90% CL upper limit of neutrino flux from 12 SNR sources is 2 to 3 orders of magnitude larger than the model prediction for the sum of 243 SNRs. The ν_e flux from stacked SNRs in galaxy in the energy range from 10 GeV to 1 TeV is constrained for the first time.

7.5 Comparison with Other Observation

In this section the search results from this analysis are compared to those from the search using SK UPMU data published in 2009[51] and from IceCube observation of TXS

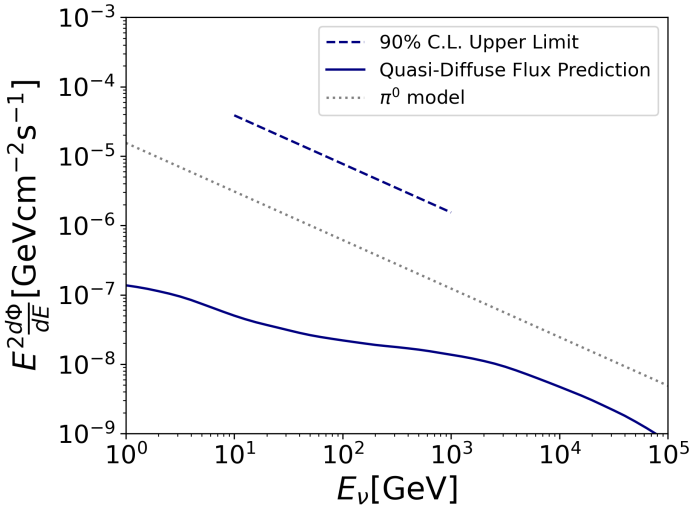

Figure 7.5: Comparison between 90% C.L. upper limits of stacked search for ν_e from SNR in Galaxy in this analysis (blue dotted), and model prediction of quasi-diffuse flux from SNR excluding the 21 sources in Ref.[31] (blue solid). π_0 model prediction from Ref.[1] is also shown (gray dotted).

0506+056[23] and NGC 1068[22].

In the previous SK search, the 90% C.L. neutrino flux upper limit is calculated and averaged in each declination bin. Here, the flux normalization upper limits from time-integrated search for ν_μ (Figure 6.5) is converted to neutrino flux upper limit by integrating $\Phi_0^{90\mathrm{CL}} \cdot \left(\frac{E_\nu}{1\ \mathrm{GeV}}\right)^{-2}$ from 1.6 GeV to 100 TeV. Then the flux upper limits of search directions below $\delta = 53.6°$ are averaged. Figure 7.6 presents the comparison of flux upper limits between this study and the previous search. A clear improvement from previous search can be seen.

In Ref. [23] and Ref.[22], the best fitted spectral index for TXS 0506+056 and NGC 1068 from IceCube results are 2.0 and 3.1, respectively. The time-integrated ν_μ searches at the direction of these two sources have the result $\hat{n}_S = 0$ in this analysis. The 90% C.L. upper limits are calculated for both sources assuming $\gamma = 2$ and $\gamma = 3.2$, respectively. The flux upper limits are shown in Figure 7.7 and compared with the IceCube observation. Note that although the energy range SK is sensitive to include with the energy range of IceCube result and upper limit is close to the observation of neutrino flux from NGC 1068, it does not mean SK is close to observe neutrino events from NGC 1068. First, there is no evidence suggesting the neutrino flux spectrum is the same in lower energy range that IceCube is not sensitive to. Second, the expected neutrinos in that energy range will only contribute a small fraction of neutrinos in the energy range SK is sensitive to (1 GeV to 100 TeV) with such a soft spectrum $\gamma = 3.2$. The expected signal events in SK with IceCube observation from 1.5 TeV to 15 TeV is 0.12, which is about 2 orders of magnitude smaller than the sensitivity of this spectrum.

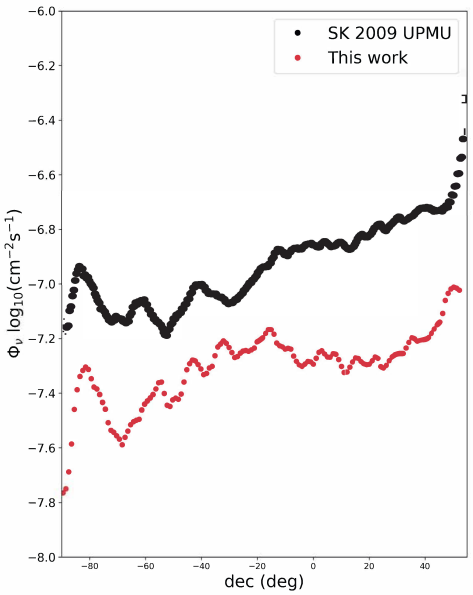

Figure 7.6: Comparison of the neutrino flux upper limit against declination in the time-integrated search for ν_μ of this work (red) and previous SK search result using UPMU (black). Flux are integrated from 1.6 GeV with $\gamma = 2$ for both cases.

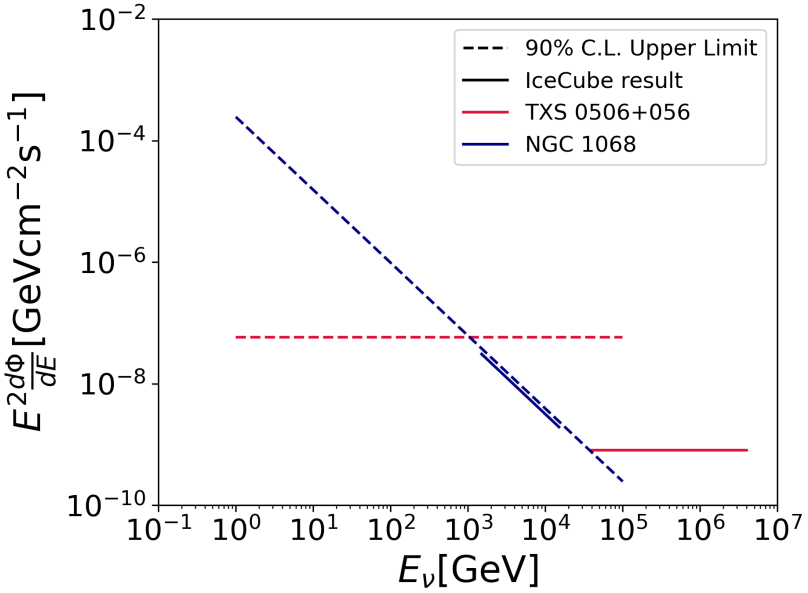

Figure 7.7: Neutrino flux upper limit times square of neutrino energy at direction of TXS 0506+056 (red dashed) and NGC 1068 (blue dashed), assuming $\gamma = 2$ and $\gamma = 3.2$, respectively. IceCube observation from Ref.[23] (red solid) and Ref.[22] (blue solid) are drawn for a comparison. Although upper limit at direction of NGC 1068 in this work looks close to the IceCube observation in 1.5 TeV to 15 TeV region, the energy range coverage is too huge to be able to draw any conclusion.

7.6 Outlook and Future

The next generation neutrino detector, Hyper-Kamiokande (HK) is scheduled to start full operation from 2028. The detector is about 7.2 times larger than SK with a volume of 197.3 kt. The effective area for UPMU events is proportional to the cross section of the tank (as ν_μ does not interact in the tank), so HK will have an affective area 3.4 larger than SK. Assuming the detection condition for HK is similar to SK, the exposure of HK to UPMU with 20 years run will be ~3.8 times larger than that of this study. However, the number of background events will be 3.8 times larger as well. To estimate the sensitivity for the search for the astrophysical ν_μ point source of HK, the same method described in Section 5.6.3 is used. The background toy MC used in trials is 3.8 times the one used in this work. The number of signal events that satisfies the Equation 5.32, $n_S^{90\%\ \text{median}}$, is 7, which is ~1.8 times of that in this analysis. The neutrino flux normalization of sensitivity is then given by

$$\Phi_{0,\nu_\mu}^{90\%\ \text{median,HK}} = \frac{n_{S,\nu_\mu}^{90\%\ \text{median,HK}}}{A_{eff,\nu_\mu}^{\text{HK}} T_{live}^{\text{HK}}} \approx \frac{1.8 \times n_{S,\nu_\mu}^{90\%\ \text{median,SK}}}{3.8 \times A_{eff,\nu_\mu}^{\text{SK}} T_{live}^{\text{SK}}} = 0.49 \Phi_{0,\nu_\mu}^{90\%\ \text{median,SK}} \tag{7.1}$$

The comparison of the estimated sensitivity of HK and the sensitivity of this work assuming $\gamma = 2$ at 1 GeV is presented in Figure 7.8.

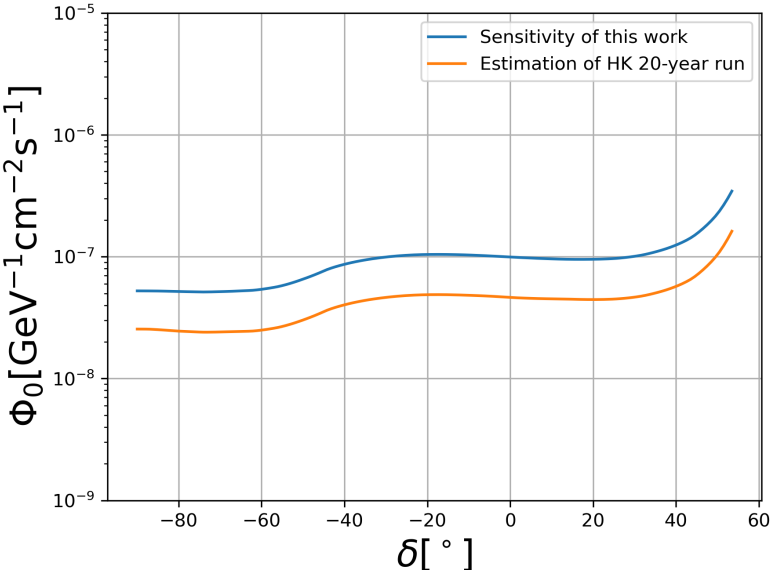

Figure 7.8: Comparison of sensitivity of search for ν_μ point source estimated for HK 20-year run (orange) and this work (blue) assuming $\gamma = 2$ at 1 GeV as a function of declination.

For search for ν_e, the effective area of FC events (which is proportional to volume) is

about 7.2 times larger. Assume the same detection condition and same selection efficiency for CCν_e events in HK, the exposure of HK 20-year run is ~8.1 times larger than SK-I to SK-V. The $n_S^{90\%\ \text{median}}$ for points source search is estimated in the same way as the estimation for ν_μ using trials, in which the background toy MC is 8.1 times that of this work. $n_{S,\nu_e}^{90\%\ \text{median,HK}} = 5$, and is $\sim 1.7 \cdot n_{S,\nu_e}^{90\%\ \text{median,SK}}$. The sensitivity is

$$\Phi_{0,\nu_\mu}^{90\%\ \text{median,HK}} \approx \frac{1.7 \times n_{S,\nu_e}^{90\%\ \text{median,SK}}}{8.1 \times A_{eff,\nu_\mu}^{\text{SK}} T_{live}^{\text{SK}}} = 0.21 \Phi_{0,\nu_\mu}^{90\%\ \text{median,SK}} \tag{7.2}$$

and comparison between sensitivities assuming $\gamma = 2$ at 10 GeV is presented in Figure 7.9.

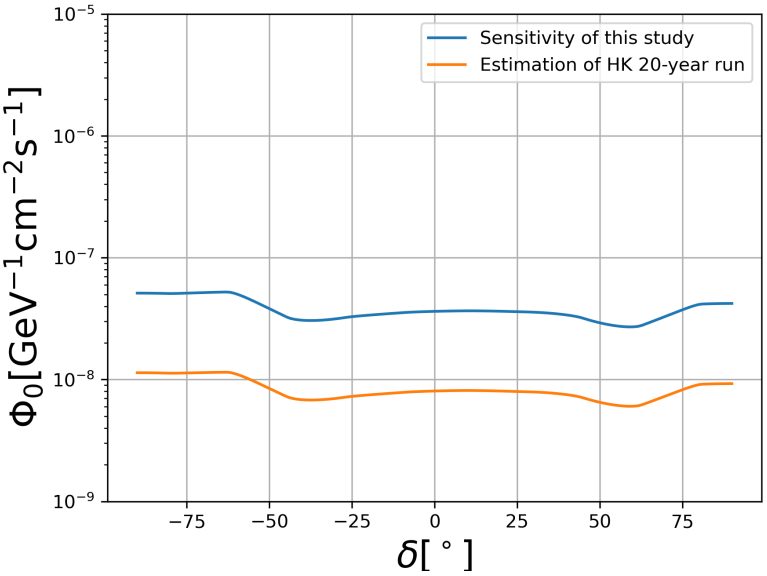

Figure 7.9: Comparison of sensitivity of search for ν_e point source estimated for HK 20-year run (orange) and this work (blue) assuming $\gamma = 2$ at 10 GeV as a function of declination.

The sensitivity of search for diffuse ν_e from Galactic plane with HK 20-year run is also estimated. $n_{S,\text{diffuse Galactic}}^{90\%\ \text{median,HK}}$ is calculated to be 23, 2.3 times higher than in this analysis, and $\Phi_{0,\text{diffuse Galactic}}^{90\%\ \text{median,HK}} \approx 0.28 \Phi_{0,\text{diffuse Galactic}}^{90\%\ \text{median,SK}}$. A comparison between estimated sensitivity and sensitivity from this work is shown in Figure 7.10.

It is worth noticing that this is a rough estimate assuming exactly the same detection condition as for SK. There are two key points that can improve the sensitivity of HK in addition to the large size of the detector. The first is the improvement of the angular resolution. With better angular resolution, the expected signal event distribution will be more concentrated, making it easier to separate them from background events. Another aspect is the energy scale. With larger detector, the energy measurement range will

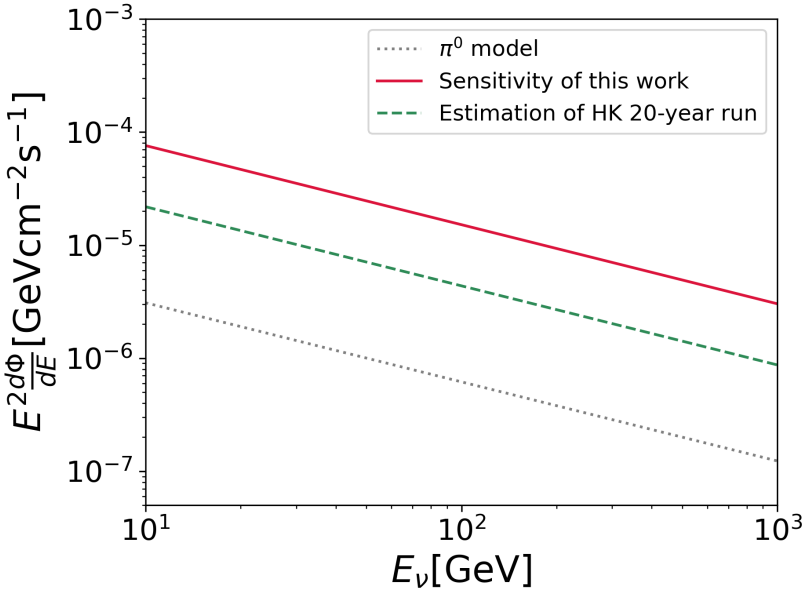

Figure 7.10: Comparison of sensitivity of search for diffuse neutrino from Galactic plane estimated for HK 20-year run (orange) and this work (blue) assuming $\gamma = 2.7$ as a function of neutrino energy.

increase. Background contamination can be further reduced by setting a higher energy cut, and higher energy events are less likely to be background events.

Chapter 8

Conclusions

In this thesis, results for searches for high-energy astrophysical neutrino sources using the 6619.1 days Super-Kamiokande (SK) data is presented. Comparing with the previous published SK result, the live-time is twice larger. The data used in the analysis are extended to all three high-energy data samples (fully contained, partially contained and upward-going muon), covering energy range from 1 GeV to 100 TeV. An updated unbinned maximum likelihood method which include the energy probability densities of given event energies is applied. The fit of neutrino energy spectrum is achieved in searches for point sources with the inclusion of energy probability in the likelihood.

An improved event classification in fully contained sample is deployed to separate charged-current interacted ν_e-like events from other events. Searches for high-energy astrophysical ν_e are performed for the first time in SK with the selected data set. The advantage of searching with ν_e is that atmosphere ν_e spectrum is much softer than ν_μ in GeV region. An energy cut on visible energies is set to 10 GeV, from where atmosphere ν_e flux start to become much lower than ν_μ. The multi-ring classification uses boosted decision tree, and background rejection increased 15% compared with classification using particle ID of the most energetic ring at the signal efficiency of 60%.

Full-sky scans are performed in time-integrated search for ν_μ and ν_e with over 49,000 search directions. 114 sources from TeV Catalog and 49 high-energy event alert from IceCube are checked in time-integrated searches for ν_μ and ν_e point source as priors. Sensitivities is calculated using pseudo-experiments with toy Monte Carlo for each search.

No significant excesses of high-energy astrophysical neutrinos over atmosphere neutrino background were found in the searches. The hottest spots found in time-integrated search for ν_μ and ν_e are at $(32.3^\circ, -15.1^\circ)$ and $(48.5^\circ, 8.4^\circ)$ in equatorial coordinates (J2000), with p-values of 88.4%, 54.7%. The p-value of the most probable source in the lists of candidates is RBS0413, an AGN. The p-value is 0.54%, which is less significant

than 3σ. 90% confidence level upper limits of neutrino flux are set for time-integrated search.

Comparisons between the upper limits of ν_μ and ν_e flux obtained in this analysis and model predictions[25, 31] are made for 4 SNRs (RX J1713.7-3946, RX J0852.0-4622, IC443 and W28) and 2 PWNs (Crab Nebula and Vela X). The results of this study is consistent with the models (upper limits are larger than model predictions). The upper limits are set for these sources from 1 GeV to 100 TeV, which covers the GeV region that large neutrino observatories including IceCube are not sensitive to.

Time-dependent search is performed for the first time in SK. While time-integrated search searches for neutrino spatial cluster from continuous emission source, short-duration but intense emission may be diluted by background over the long-time period. Time-dependent search is more sensitive to transient neutrino emission. The full sky-scan shows no significant excess. Hottest spot is at $(111.8°, 15.7°)$, with a fitted duration of 1200 s on 50927.8 modified Julian date with a p-value of 68.5%. Neutrino fluence upper limits, which corresponding to the best fitted emission duration, are set for search directions with none-zero fitted number of signal events in full-sky scan.

Recent result published by IceCube provides evidence of observation of high-energy diffuse neutrino from galactic plane. Since the model based on high-energy gamma ray observations predicts a continuous diffuse neutrino spectrum down to GeV region, and the cascade sample of IceCube used by that analysis consists of a considerable fraction of ν_e, the search for diffuse neutrino from galactic plane is performed using the selected ν_e data. The search assumes that neutrino spatial distribution follows the one from π^0 model established on high-energy gamma ray observation[1], and assumes a power-law energy spectrum with $\gamma = 2.7$. The search region is limited to $|b| < 15°$, which is chosen on the basis of gamma ray distribution and angular resolution of SK events, to reduce background.

Although the search for diffuse ν_e from galactic plane gives a result of 0 excess in number of signal events, an upper limit of ν_e flux is set to $\left(\frac{d\Phi}{dE}\right)^{\mathrm{90C.L.}}_{\mathrm{diffuse}} = 7.6 \times 10^{-7}\ \mathrm{GeV^{-1}cm^{-2}s^{-1}} \cdot \left(\frac{\mathrm{E}_\nu}{10\mathrm{GeV}}\right)^{-2.7}$ from 10 GeV to 1 TeV, which marks the first neutrino upper limit in this energy range. This result is compared to predictions based on ARGO-YBJ[3] and Tibet[52] observations and is consistent.

The sources for cosmic ray acceleration in galaxy are candidates for diffuse neutrinos from galactic plane as well. Such sources include supernova remnant (SNR), pulsar wind nebula (PWN) and unidentified source (UNID). In this analysis, three distinct searches

for ν_e are performed from these three types of sources. The search is enhanced by stacking 12 sources of each type together.

None of the three types of sources shows an excess. Summed-up ν_e flux upper limits for each source type is set to $\left(\frac{d\Phi}{dE}\right)^{90\text{C.L.}}_{\text{SNR}} = 3.7\times10^{-7}\ \text{GeV}^{-1}\text{cm}^{-2}\text{s}^{-1}\cdot\left(\frac{\text{E}_\nu}{10\text{GeV}}\right)^{-2.7}$, $\left(\frac{d\Phi}{dE}\right)^{90\text{C.L.}}_{\text{PWN}} = 6.3\times10^{-7}\ \text{GeV}^{-1}\text{cm}^{-2}\text{s}^{-1}\cdot\left(\frac{\text{E}_\nu}{10\text{GeV}}\right)^{-2.7}$ and $\left(\frac{d\Phi}{dE}\right)^{90\text{C.L.}}_{\text{UNID}} = 2.7\times10^{-7}\ \text{GeV}^{-1}\text{cm}^{-2}\text{s}^{-1}\cdot\left(\frac{\text{E}_\nu}{10\text{GeV}}\right)^{-2.7}$ in the 10 GeV to 1 TeV energy range, respectively. The upper limit is compared with the quasi-diffuse neutrino predicted from SNRs[31] and no inconsistency was observed.

Appendix A

Results of Search With List of Candidates

Table A.1: Results of time-integrated search with list of source candidates from TeVCat, including name, right ascension (α), declination (δ), and best fitted number of signal events $\hat{n}_S$, 90% C.L. flux normalization upper limits at 1 GeV ($\Phi_0^{90\%}[\times 10^{-8}\mathrm{GeV}^{-1}\mathrm{cm}^{-2}\mathrm{s}^{-1}]$) assuming $\gamma = 2$, and p-value, in time-integrated search for ν_ν and ν_e.

Name	$\delta[^\circ]$	$\alpha[^\circ]$	ν_μ			ν_e		
			$\hat{n}_S$	$\Phi_0^{90\%}$	p	$\hat{n}_S$	$\Phi_0^{90\%}$	p
PKS2005-489	302.4	-48.8	0.0	3.1	-	0.0	483.3	-
PKS0537-441	84.7	-44.1	0.0	6.0	-	0.0	446.7	-
PKS0447-439	72.4	-43.8	0.0	6.7	-	0.0	711.2	-
1ES1312-423	198.7	-42.6	1.5	10.8	0.12	1.0	802.7	0.027
1ES2322-409	351.2	-40.7	0.0	3.9	-	0.0	602.4	-
PKS1440-389	221.0	-39.1	0.0	5.1	-	0.0	541.9	-
PKS0426-380	67.2	-37.9	0.0	7.0	-	2.8	1111.9	0.039
PKS1454-354	224.4	-35.7	0.9	10.3	0.21	0.0	433.2	-
TXS1714-336	259.4	-33.7	1.5	11.8	0.11	0.0	479.6	-
PKS0548-322	87.7	-32.3	0.0	11.9	-	0.9	716.7	0.16
1RXSJ101015.9-311909	152.6	-31.3	0.0	6.1	-	0.0	575.0	-
1RXSJ023832.6-311658	39.6	-31.3	0.0	4.6	-	0.0	389.9	-
H2356-309	359.8	-30.6	0.0	4.7	-	0.0	604.2	-
PKS2155-304	329.7	-30.2	3.1	17.5	0.0097	0.0	396.5	-
1RXSJ195815.6-301119	299.6	-30.2	0.0	5.1	-	1.2	772.7	0.17
TXS1515-273	229.5	-27.5	0.0	6.0	-	0.0	385.1	-
PKS0301-243	45.8	-24.1	0.0	5.9	-	0.0	441.7	-
1ES1101-232	165.9	-23.5	0.0	7.3	-	0.0	514.1	-
MRC0910-208	138.2	-21.1	1.2	10.5	0.056	0.0	499.7	-
KUV00311-1938	8.4	-19.4	0.0	9.1	-	0.0	572.1	-
SHBLJ001355.9-185406	3.5	-18.9	0.0	4.6	-	0.0	635.3	-
1ES0347-121	57.4	-12.0	0.0	5.3	-	0.0	544.5	-
1ES 0414+009	64.2	1.1	0.0	10.0	-	0.0	508.2	-
RGBJ0152+017	28.2	1.8	0.0	7.2	-	0.0	479.7	-
1RXS J081201.8+023735	123.0	2.6	0.0	7.0	-	0.0	503.9	-
PG1553+113	238.9	11.2	2.5	17.5	0.096	0.0	572.1	-
RBS0723	131.8	11.6	0.0	6.2	-	0.0	509.3	-
H1722+119	261.3	11.9	0.0	8.4	-	0.0	543.7	-

Continued on next page

Table A.1: (Continued) Results of time-integrated search with list of source candidates from TeVCat, including name, right ascension (α), declination (δ), and best fitted number of signal events $\hat{n}_S$, 90% C.L. flux normalization upper limits at 1 GeV ($\Phi_0^{90\%}[\times 10^{-8}\mathrm{GeV}^{-1}\mathrm{cm}^{-2}\mathrm{s}^{-1}]$) assuming $\gamma = 2$, and p-value, for SNR, PWN and UNID in time-integrated search for ν_ν and ν_e.

Name	$\alpha[^\circ]$	$\delta[^\circ]$	ν_μ			ν_e		
			$\hat{n}_S$	$\Phi_0^{90\%}$	p	$\hat{n}_S$	$\Phi_0^{90\%}$	p
1ES1440+122	220.8	12.0	0.0	5.4	-	0.0	479.7	-
RXJ0648.7+1516	102.2	15.3	0.0	8.4	-	0.0	504.8	-
PKS0235+164	39.7	16.6	0.0	5.3	-	0.8	773.1	0.15
RBS0413	50.0	18.8	6.6	28.5	0.0054	0.0	610.3	-
1ES1741+196	266.0	19.6	3.8	28.2	0.14	3.0	1412.7	0.036
1ES0229+200	38.2	20.3	0.0	6.3	-	0.0	543.5	-
RGBJ2243+203	341.0	20.3	0.0	4.4	-	0.0	834.7	-
VERJ0521+211	80.4	21.2	1.3	24.6	0.26	0.0	563.0	-
HESSJ1943+213	296.0	21.3	0.0	4.6	-	0.0	496.6	-
S20109+22	18.0	22.7	0.0	6.2	-	0.0	769.0	-
PKS1424+240	216.8	23.8	2.1	14.8	0.10	0.0	446.9	-
RGBJ2042+244	310.5	24.4	1.9	11.6	0.035	0.0	645.5	-
MS1221.8+2452	186.1	24.6	0.0	5.5	-	0.0	544.2	-
1ES0647+250	102.7	25.0	0.0	6.3	-	0.0	467.3	-
S31227+25	187.6	25.3	0.0	5.9	-	0.0	529.1	-
WComae	185.4	28.2	0.0	4.8	-	0.0	590.8	-
1ES1215+303	184.4	30.1	0.0	12.5	-	0.0	602.0	-
Markarian421	166.1	38.2	5.1	30.3	0.019	0.0	689.6	-
B32247+381	342.5	38.4	0.0	5.7	-	0.7	747.5	0.16
RGBJ0136+391	16.6	39.7	3.4	38.0	0.19	0.0	519.8	-
Markarian501	253.5	39.8	0.0	4.5	-	0.0	428.6	-
H1426+428	217.1	42.7	0.0	5.3	-	0.0	635.3	-
1ES1011+496	153.8	49.4	0.0	21.1	-	0.0	441.1	-
1ES1727+502	262.1	50.2	1.7	27.2	0.028	0.0	442.0	-
1ES2344+514	356.8	51.7	2.5	54.9	0.14	0.0	343.8	-
TXS0210+515	33.6	51.8	0.2	18.4	0.27	0.0	372.8	-
PGC2402248	113.4	51.9	0.0	11.6	-	0.0	518.9	-
1ES0806+524	122.5	52.3	0.0	14.1	-	0.0	379.5	-
1ES2037+521	309.8	52.3	0.0	13.4	-	0.0	361.9	-
RGBJ0710+591	107.6	59.2	0.0	373.5	-	1.7	811.2	0.054
1ES0033+595	8.8	59.8	0.0	333.4	-	0.0	370.1	-
1ES1959+650	300.0	65.2	0.0	650.7	-	1.2	771.9	0.040
RXJ1136.5+6737	174.1	67.6	0.0	605.3	-	0.0	415.6	-
1ES0502+675	77.0	67.6	1.5	1128.6	0.23	0.0	709.4	-
Markarian180	174.1	70.2	0.0	539.2	-	0.0	422.4	-
LMCP3	84.0	-67.6	0.0	4.2	-	1.0	1356.2	0.023
PSRB1259-63	195.7	-63.8	0.7	5.2	0.23	0.0	722.5	-
EtaCarinae	161.2	-59.7	0.0	4.2	-	0.0	648.3	-
HESSJ1018-589A	154.7	-59.0	0.0	4.4	-	0.0	595.4	-
CirX-1	230.2	-57.2	0.0	3.1	-	0.8	1419.1	0.18
GX339-4	255.7	-48.8	0.0	2.9	-	2.8	1381.7	0.028
LS5039	276.6	-14.8	0.0	5.0	-	0.0	450.1	-
HESSJ1832-093	278.2	-9.4	0.0	7.3	-	0.0	545.4	-
SS433w1	287.6	5.0	0.0	4.7	-	0.9	888.8	0.11
HESSJ0632+057	98.2	5.8	0.0	3.5	-	0.0	753.0	-
PSR J2032+4127	308.0	41.5	2.8	27.4	0.12	0.0	400.8	-
LSI+61303	40.1	61.3	0.0	306.8	-	0.0	365.7	-
MSH15-52	228.5	-59.1	1.6	7.2	0.10	0.4	1358.2	0.20
VelaPulsar	128.8	-45.2	0.0	8.4	-	1.5	880.2	0.12

Continued on next page

Table A.1: (Continued) Results of time-integrated search with list of source candidates from TeVCat, including name, right ascension (α), declination (δ), and best fitted number of signal events $\hat{n}_S$, 90% C.L. flux normalization upper limits at 1 GeV ($\Phi_0^{90\%}[\times 10^{-8}\mathrm{GeV}^{-1}\mathrm{cm}^{-2}\mathrm{s}^{-1}]$) assuming $\gamma = 2$, and p-value, for SNR, PWN and UNID in time-integrated search for ν_ν and ν_e.

Name	$\alpha[^\circ]$	$\delta[^\circ]$	ν_μ			ν_e		
			$\hat{n}_S$	$\Phi_0^{90\%}$	p	$\hat{n}_S$	$\Phi_0^{90\%}$	p
HESSJ1708-443	257.4	-44.5	3.6	20.9	0.12	0.0	752.9	-
Terzan5	267.0	-24.9	0.0	6.9	-	0.0	388.7	-
Geminga	98.5	17.8	0.0	7.0	-	0.0	455.7	-
PSRB1957+20	299.9	20.8	0.0	7.1	-	0.0	488.2	-
Crab	83.6	22.0	1.9	14.8	0.099	0.0	523.5	-
PKS1424-418	217.0	-42.1	0.0	4.5	-	0.0	530.6	-
SwiftJ1656.3-3302	254.1	-33.0	3.7	30.6	0.16	0.9	646.1	0.056
PKS1622-297	246.5	-29.9	0.0	3.9	-	0.0	483.1	-
PKS0454-234	74.3	-23.4	1.1	11.7	0.18	0.0	619.8	-
PKS1830-211	278.4	-21.1	0.0	8.3	-	0.0	429.4	-
QSO1730-130	263.3	-13.1	0.0	4.2	-	0.5	668.0	0.18
PKS0727-11	112.6	-11.7	0.0	5.7	-	0.0	947.2	-
PKS1406-076	212.2	-7.9	0.0	8.9	-	0.0	548.9	-
QSO2022-077	306.4	-7.6	0.0	5.4	-	0.0	451.2	-
3C279	194.0	-5.8	0.0	7.4	-	0.0	454.4	-
B1030+074	158.4	7.2	1.9	12.4	0.050	0.0	466.5	-
PKS1502+106	226.1	10.5	0.0	5.1	-	0.0	462.5	-
3C454.3	343.5	16.2	1.0	9.2	0.14	1.3	1107.2	0.14
4C+21.35	186.2	21.4	0.0	6.4	-	0.0	503.0	-
B1422+231	216.2	22.9	2.6	15.8	0.060	0.0	438.8	-
PKS1441+25	221.0	25.0	0.0	8.6	-	0.0	479.1	-
LHA120-N-157B	84.4	-69.2	0.0	2.7	-	1.0	1261.7	0.018
RCW86	220.7	-62.5	1.9	9.1	0.17	1.1	1312.7	0.058
MSH15-52	228.5	-59.2	1.6	7.2	0.10	0.4	1362.9	0.20
SNRG327.1-01.1	238.2	-55.1	0.0	3.5	-	1.7	1490.0	0.10
RXJ0852.0-4622	133.0	-46.4	2.7	13.7	0.090	0.0	638.0	-
RXJ1713.7-3946	258.2	-39.8	3.3	26.5	0.19	0.0	499.2	-
HESS J1745-303	266.3	-30.4	0.0	4.4	-	0.0	406.9	-
W28	270.4	-23.3	0.0	8.5	-	0.0	395.1	-
SNRG015.4+00.1	274.5	-15.5	0.0	4.6	-	0.0	438.4	-
W44	284.0	1.4	0.0	6.7	-	0.0	754.4	-
HESSJ1912+101	288.2	10.2	0.0	3.4	-	0.0	624.4	-
W51C	290.8	14.2	0.0	5.2	-	0.0	596.5	-
IC443	94.2	22.5	2.4	19.2	0.16	0.0	434.6	-
S40954+65	149.7	65.6	2.5	1820.0	0.22	2.7	961.1	0.036
RGBJ2056+496	314.2	49.7	0.0	7.6	-	0.0	344.6	-
PKS1413+135	214.0	13.3	4.8	36.2	0.16	0.0	464.9	-

Table A.2: Results of time-integrated search with list of source candidates from IceCube trigger alert, including right ascension (α), declination (δ), and best fitted number of signal events $\hat{n}_S$, 90% C.L. flux normalization upper limits at 1 GeV ($\Phi_0^{90\%}[\times 10^{-8}\mathrm{GeV}^{-1}\mathrm{cm}^{-2}\mathrm{s}^{-1}]$) assuming $\gamma = 2$, and p-value, in time-integrated search for ν_ν and ν_e.

$\delta[^\circ]$	$\alpha[^\circ]$	ν_μ			ν_e			$\delta[^\circ]$	$\alpha[^\circ]$	ν_μ			ν_e		
		$\hat{n}_S$	$\Phi_0^{90\%}$	p	$\hat{n}_S$	$\Phi_0^{90\%}$	p			$\hat{n}_S$	$\Phi_0^{90\%}$	p	$\hat{n}_S$	$\Phi_0^{90\%}$	p
127.9	-31.2	0.0	8.0	-	1.9	957.6	0.13	266.5	-4.4	0.0	4.5	-	1.2	945.0	0.11
110.6	-0.4	0.0	4.7	-	1.0	875.9	0.10	238.0	18.6	0.0	3.7	-	0.0	541.4	-
182.4	-21.2	0.0	5.7	-	2.3	1089.3	0.071	171.0	26.4	0.0	4.8	-	1.7	1087.2	0.11
67.9	40.3	0.0	7.3	-	0.8	742.2	0.10	70.8	19.8	1.3	9.8	0.036	0.6	702.9	0.16
345.6	-24.8	2.3	18.7	0.11	0.0	599.3	-	205.2	-2.4	0.8	9.9	0.21	0.9	817.3	0.10
164.8	-71.5	3.8	13.0	0.11	0.0	679.5	-	129.8	-10.4	0.0	5.0	-	0.0	478.1	-
167.2	20.7	0.0	3.8	-	1.9	1083.1	0.078	301.8	11.5	0.0	5.0	-	0.0	568.0	-
93.4	14.0	0.0	3.7	-	0.0	498.1	-	289.2	-14.2	0.0	6.6	-	0.0	468.5	-
206.6	-22.0	1.4	14.9	0.16	0.0	762.9	-	344.5	1.6	0.0	3.8	-	0.0	517.9	-
219.6	-86.2	0.0	5.7	-	0.0	656.7	-	292.8	33.1	0.0	5.0	-	0.0	516.2	-
239.0	-37.7	0.0	5.6	-	0.0	464.2	-	349.5	-13.7	0.0	7.5	-	0.0	577.4	-
55.6	-16.5	5.0	37.7	0.056	0.0	686.4	-	110.3	11.6	0.0	4.3	-	0.0	619.9	-
160.0	6.6	0.0	7.1	-	0.0	471.5	-	169.7	-1.3	1.0	12.4	0.22	0.0	460.0	-
80.8	-20.8	0.0	10.4	-	0.0	472.9	-	328.2	6.2	0.0	4.7	-	0.5	745.1	0.17
240.2	-0.4	0.0	12.9	-	0.0	554.8	-	54.8	34.0	4.3	26.6	0.064	0.0	668.7	-
0.4	7.5	0.0	4.5	-	0.0	507.3	-	103.3	3.9	0.0	6.2	-	0.0	703.5	-
240.6	9.3	1.9	14.5	0.10	0.0	572.4	-	194.5	-4.3	0.5	10.0	0.26	0.0	502.8	-
200.3	-32.4	0.0	4.7	-	0.0	613.3	-	262.2	-2.4	0.0	3.9	-	0.7	911.3	0.19
40.8	12.6	0.0	10.1	-	0.0	663.5	-	263.4	-14.8	0.0	4.2	-	0.0	553.8	-
305.2	-26.6	0.0	6.4	-	0.0	425.6	-	352.3	2.1	0.0	9.1	-	0.0	452.7	-
221.8	-26.0	0.0	6.4	-	0.0	412.2	-	214.5	-0.3	0.0	4.8	-	0.2	692.9	0.20
331.1	11.1	0.0	8.0	-	1.3	989.6	0.012	122.8	-0.8	1.8	13.7	0.085	0.0	568.8	-
88.7	0.5	0.0	7.0	-	0.0	693.5	-	46.6	15.0	4.5	27.0	0.083	3.3	1349.0	0.033
307.5	1.2	0.0	4.7	-	0.0	575.7	-	98.3	-15.0	0.0	10.9	-	2.6	1217.2	0.032
116.4	-10.7	1.2	14.8	0.19	4.0	1454.0	0.020								

Bibliography

[1] M. Ackermann et al. "FERMI-LAT OBSERVATIONS OF THE DIFFUSE -RAY EMISSION: IMPLICATIONS FOR COSMIC RAYS AND THE INTERSLAR MEDIUM". en. In: *The Astrophysical Journal* 750.1 (Apr. 2012). Publisher: The American Astronomical Society, p. 3. ISSN: 0004-637X. DOI: 10.1088/0004-637X/750/1/3. URL: https://dx.doi.org/10.1088/0004-637X/750/1/3 (visited on 07/06/2025).

[2] J. Alcaraz et al. "Cosmic protons". In: *Physics Letters B* 490.1 (Sept. 2000), pp. 27–35. ISSN: 0370-2693. DOI: 10.1016/S0370-2693(00)00970-9. URL: https://www.sciencedirect.com/science/article/pii/S0370269300009709 (visited on 07/06/2025).

[3] B. Bartoli et al. "STUDY OF THE DIFFUSE GAMMA-RAY EMISSION FROM THE GALACTIC PLANE WITH ARGO-YBJ". en. In: *The Astrophysical Journal* 806.1 (June 2015). Publisher: The American Astronomical Society, p. 20. ISSN: 0004-637X. DOI: 10.1088/0004-637X/806/1/20. URL: https://dx.doi.org/10.1088/0004-637X/806/1/20 (visited on 07/06/2025).

[4] Julia K. Becker. "High-energy neutrinos in the context of multimessenger astrophysics". In: *Physics Reports* 458.4 (Mar. 2008), pp. 173–246. ISSN: 0370-1573. DOI: 10.1016/j.physrep.2007.10.006. URL: https://www.sciencedirect.com/science/article/pii/S037015730800029X (visited on 07/06/2025).

[5] Pasquale Blasi. "The origin of galactic cosmic rays". en. In: *The Astronomy and Astrophysics Review* 21.1 (Nov. 2013), p. 70. ISSN: 1432-0754. DOI: 10.1007/s00159-013-0070-7. URL: https://doi.org/10.1007/s00159-013-0070-7 (visited on 07/04/2025).

[6] Jim Braun et al. "Time-dependent point source search methods in high energy neutrino astronomy". In: *Astroparticle Physics* 33.3 (Apr. 2010), pp. 175–181. ISSN: 0927-6505. DOI: 10.1016/j.astropartphys.2010.01.005. URL: https://www.sciencedirect.com/science/article/pii/S0927650510000241 (visited on 07/06/2025).

[7] The IceCube Collaboration et al. “Multimessenger observations of a flaring blazar coincident with high-energy neutrino IceCube-170922A”. EN. In: *Science* (July 2018). Publisher: American Association for the Advancement of Science. DOI: 10.1126/science.aat1378. URL: https://www.science.org/doi/10.1126/science.aat1378 (visited on 08/13/2025).

[8] ENRICO Fermi. “On the Origin of the Cosmic Radiation”. In: *Physical Review* 75.8 (Apr. 1949). Publisher: American Physical Society, pp. 1169–1174. DOI: 10.1103/PhysRev.75.1169. URL: https://link.aps.org/doi/10.1103/PhysRev.75.1169 (visited on 07/04/2025).

[9] *Fermi Gamma-ray Space Telescope: Exploring the Extreme Universe*. URL: https://fermi.gsfc.nasa.gov/science/eteu/agn/ (visited on 07/06/2025).

[10] *FSSC: Data » Data Access » LAT Background Models*. URL: https://fermi.gsfc.nasa.gov/ssc/data/access/lat/BackgroundModels.html (visited on 07/06/2025).

[11] S. Fukuda et al. “The Super-Kamiokande detector”. In: *Nuclear Instruments and Methods in Physics Research Section A: Accelerators, Spectrometers, Detectors and Associated Equipment* 501.2 (Apr. 2003), pp. 418–462. ISSN: 0168-9002. DOI: 10.1016/S0168-9002(03)00425-X. URL: https://www.sciencedirect.com/science/article/pii/S016890020300425X (visited on 07/06/2025).

[12] Raj Gandhi et al. “Ultrahigh-energy neutrino interactions”. In: *Astroparticle Physics* 5.2 (Aug. 1996), pp. 81–110. ISSN: 0927-6505. DOI: 10.1016/0927-6505(96)00008-4. URL: https://www.sciencedirect.com/science/article/pii/0927650596000084 (visited on 08/12/2025).

[13] R. Gran et al. “Neutrino-nucleus quasi-elastic and 2p2h interactions up to 10 GeV”. In: *Physical Review D* 88.11 (Dec. 2013). Publisher: American Physical Society, p. 113007. DOI: 10.1103/PhysRevD.88.113007. URL: https://link.aps.org/doi/10.1103/PhysRevD.88.113007 (visited on 07/06/2025).

[14] Kenneth Greisen. “End to the Cosmic-Ray Spectrum?” In: *Physical Review Letters* 16.17 (Apr. 1966). Publisher: American Physical Society, pp. 748–750. DOI: 10.1103/PhysRevLett.16.748. URL: https://link.aps.org/doi/10.1103/PhysRevLett.16.748 (visited on 07/04/2025).

[15] S. Haino et al. “Measurements of primary and atmospheric cosmic-ray spectra with the BESS-TeV spectrometer”. In: *Physics Letters B* 594.1 (July 2004), pp. 35–46. ISSN: 0370-2693. DOI: 10.1016/j.physletb.2004.05.019. URL: https://www.sciencedirect.com/science/article/pii/S0370269304007567 (visited on 07/06/2025).

[16] Francis Halzen et al. "HIGH-ENERGY NEUTRINOS FROM RECENT BLAZAR FLARES". en. In: *The Astrophysical Journal* 831.1 (Oct. 2016). Publisher: The American Astronomical Society, p. 12. ISSN: 0004-637X. DOI: 10.3847/0004-637X/831/1/12. URL: https://dx.doi.org/10.3847/0004-637X/831/1/12 (visited on 07/04/2025).

[17] *HEALPix - Features*. URL: https://healpix.sourceforge.io/ (visited on 07/06/2025).

[18] M. Honda et al. "Improvement of low energy atmospheric neutrino flux calculation using the JAM nuclear interaction model". In: *Physical Review D* 83.12 (June 2011). Publisher: American Physical Society, p. 123001. DOI: 10.1103/PhysRevD.83.123001. URL: https://link.aps.org/doi/10.1103/PhysRevD.83.123001 (visited on 07/06/2025).

[19] P. V. C. Hough. "Machine Analysis of Bubble Chamber Pictures". In: *Conf. Proc. C* 590914 (1959). Ed. by L. Kowarski, pp. 554–558.

[20] S. Hümmer et al. "Energy dependent neutrino flavor ratios from cosmic accelerators on the Hillas plot". In: *Astroparticle Physics* 34.4 (Nov. 2010), pp. 205–224. ISSN: 0927-6505. DOI: 10.1016/j.astropartphys.2010.07.003. URL: https://www.sciencedirect.com/science/article/pii/S092765051000126X (visited on 07/04/2025).

[21] IceCube Collaboration. "Observation of high-energy neutrinos from the Galactic plane". In: *Science* 380.6652 (June 2023). Publisher: American Association for the Advancement of Science, pp. 1338–1343. DOI: 10.1126/science.adc9818. URL: https://www.science.org/doi/10.1126/science.adc9818 (visited on 07/06/2025).

[22] IceCube Collaboration et al. "Evidence for neutrino emission from the nearby active galaxy NGC 1068". In: *Science* 378.6619 (Nov. 2022). Publisher: American Association for the Advancement of Science, pp. 538–543. DOI: 10.1126/science.abg3395. URL: https://www.science.org/doi/10.1126/science.abg3395 (visited on 07/31/2025).

[23] IceCube Collaboration et al. "Neutrino emission from the direction of the blazar TXS 0506+056 prior to the IceCube-170922A alert". In: *Science* 361.6398 (July 2018). Publisher: American Association for the Advancement of Science, pp. 147–151. DOI: 10.1126/science.aat2890. URL: https://www.science.org/doi/10.1126/science.aat2890 (visited on 08/13/2025).

[24] C. Kachulis. "Boosted Dark Matter and Atmospheric Neutrino Earth Matter Effects at Super-Kamiokande". PhD thesis. USA: Boston University.

[25] Alexander Kappes et al. “Potential Neutrino Signals from Galactic -Ray Sources”. en. In: *The Astrophysical Journal* 656.2 (Feb. 2007). Publisher: IOP Publishing, p. 870. ISSN: 0004-637X. DOI: 10.1086/508936. URL: https://iopscience.iop.org/article/10.1086/508936/meta (visited on 07/06/2025).

[26] Kumiko Kotera et al. “The Astrophysics of Ultrahigh-Energy Cosmic Rays”. en. In: *Annual Review of Astronomy and Astrophysics* 49.Volume 49, 2011 (Sept. 2011). Publisher: Annual Reviews, pp. 119–153. ISSN: 0066-4146, 1545-4282. DOI: 10.1146/annurev-astro-081710-102620. URL: https://www.annualreviews.org/content/journals/10.1146/annurev-astro-081710-102620 (visited on 07/04/2025).

[27] P. O. Lagage et al. “The maximum energy of cosmic rays accelerated by supernova shocks.” In: *Astronomy and Astrophysics* 125 (Sept. 1983). ADS Bibcode: 1983A&A...125..249L, pp. 249–257. ISSN: 0004-6361. URL: https://ui.adsabs.harvard.edu/abs/1983A&A...125..249L (visited on 07/06/2025).

[28] L. K. Lee. “Study of the neutrino mass hierarchy with the atmospheric neutrino data observed in Super-Kamiokande”. PhD thesis. Japan: University of Tokyo, 2012.

[29] Malcolm S. Longair. *High Energy Astrophysics*. Publication Title: High Energy Astrophysics ADS Bibcode: 2011hea..book.....L. Feb. 2011. URL: https://ui.adsabs.harvard.edu/abs/2011hea..book.....L (visited on 07/04/2025).

[30] Ziro Maki et al. “Remarks on the Unified Model of Elementary Particles”. In: *Progress of Theoretical Physics* 28.5 (Nov. 1962), pp. 870–880. ISSN: 0033-068X. DOI: 10.1143/PTP.28.870. URL: https://doi.org/10.1143/PTP.28.870 (visited on 07/04/2025).

[31] Matthias Mandelartz et al. “Prediction of the diffuse neutrino flux from cosmic ray interactions near supernova remnants”. In: *Astroparticle Physics* 65 (May 2015), pp. 80–100. ISSN: 0927-6505. DOI: 10.1016/j.astropartphys.2014.12.002. URL: https://www.sciencedirect.com/science/article/pii/S0927650514001881 (visited on 07/04/2025).

[32] Kohta Murase. “Active Galactic Nuclei as High-Energy Neutrino Sources”. In: *Neutrino Astronomy*. WORLD SCIENTIFIC, Dec. 2015, pp. 15–31. ISBN: 978-981-4759-40-3. DOI: 10.1142/9789814759410_0002. URL: https://www.worldscientific.com/doi/abs/10.1142/9789814759410_0002 (visited on 07/06/2025).

[33] Kohta Murase et al. “Constraining high-energy cosmic neutrino sources: Implications and prospects”. In: *Physical Review D* 94.10 (Nov. 2016). Publisher: American Physical Society, p. 103006. DOI: 10.1103/PhysRevD.94.103006. URL: https://link.aps.org/doi/10.1103/PhysRevD.94.103006 (visited on 07/04/2025).

[34] Koji Niita et al. “PHITS—a particle and heavy ion transport code system”. In: *Radiation Measurements*. Space Radiation Transport, Shielding, and Risk Assessment Models 41.9 (Oct. 2006), pp. 1080–1090. ISSN: 1350-4487. DOI: 10.1016/j.radmeas.2006.07.013. URL: https://www.sciencedirect.com/science/article/pii/S1350448706001351 (visited on 07/06/2025).

[35] H. Nishino et al. “High-speed charge-to-time converter ASIC for the Super-Kamiokande detector”. In: *Nuclear Instruments and Methods in Physics Research Section A: Accelerators, Spectrometers, Detectors and Associated Equipment* 610.3 (Nov. 2009), pp. 710–717. ISSN: 0168-9002. DOI: 10.1016/j.nima.2009.09.026. URL: https://www.sciencedirect.com/science/article/pii/S0168900209017495 (visited on 07/06/2025).

[36] C. Patrignani. “Review of Particle Physics”. en. In: *Chinese Physics C* 40.10 (Oct. 2016), p. 100001. ISSN: 1674-1137. DOI: 10.1088/1674-1137/40/10/100001. URL: https://dx.doi.org/10.1088/1674-1137/40/10/100001 (visited on 07/04/2025).

[37] B. Peters. “Primary cosmic radiation and extensive air showers”. en. In: *Il Nuovo Cimento (1955-1965)* 22.4 (Nov. 1961), pp. 800–819. ISSN: 1827-6121. DOI: 10.1007/BF02783106. URL: https://doi.org/10.1007/BF02783106 (visited on 07/04/2025).

[38] B. Pontecorvo. “Neutrino Experiments and the Problem of Conservation of Leptonic Charge”. In: *Zh. Eksp. Teor. Fiz.* 53 (1967), pp. 1717–1725.

[39] M. S. Potgieter. “The heliospheric modulation of galactic cosmic rays at solar minimum”. In: *Advances in Space Research*. The Heliosphere at Solar Minimum and Beyond 19.6 (Jan. 1997), pp. 883–892. ISSN: 0273-1177. DOI: 10.1016/S0273-1177(97)00297-4. URL: https://www.sciencedirect.com/science/article/pii/S0273117797002974 (visited on 07/06/2025).

[40] S. Roesler et al. “The Monte Carlo Event Generator DPMJET-III”. en. In: *Advanced Monte Carlo for Radiation Physics, Particle Transport Simulation and Applications*. Ed. by Andreas Kling et al. Berlin, Heidelberg: Springer, 2001, pp. 1033–1038. ISBN: 978-3-642-18211-2. DOI: 10.1007/978-3-642-18211-2_166.

[41] M. Shiozawa. “Reconstruction algorithms in the Super-Kamiokande large water Cherenkov detector”. In: *Nuclear Instruments and Methods in Physics Research Section A: Accelerators, Spectrometers, Detectors and Associated Equipment* 433.1 (Aug. 1999), pp. 240–246. ISSN: 0168-9002. DOI: 10.1016/S0168-9002(99)00359-9. URL: https://www.sciencedirect.com/science/article/pii/S0168900299003599 (visited on 07/06/2025).

[42] Maurizio Spurio. *Probes of Multimessenger Astrophysics: Charged cosmic rays, neutrinos, -rays and gravitational waves*. Astronomy and Astrophysics Library. Cham: Springer International Publishing, 2018. ISBN: 978-3-319-96853-7 978-3-319-96854-4. DOI: 10.1007/978-3-319-96854-4. URL: http://link.springer.com/10.1007/978-3-319-96854-4 (visited on 07/04/2025).

[43] Staff. *IceCube catalog of alert events up through IceCube-170922A*. en-US. July 2018. URL: https://icecube.wisc.edu/data-releases/2018/07/icecube-catalog-of-alert-events-up-through-icecube-170922a/ (visited on 07/06/2025).

[44] Todor Stanev. *High Energy Cosmic Rays*. en. Vol. 462. Astrophysics and Space Science Library. Cham: Springer International Publishing, 2021. ISBN: 978-3-030-71566-3 978-3-030-71567-0. DOI: 10.1007/978-3-030-71567-0. URL: https://link.springer.com/10.1007/978-3-030-71567-0 (visited on 07/06/2025).

[45] Super-Kamiokande Collaboration et al. "Atmospheric neutrino oscillation analysis with external constraints in Super-Kamiokande I-IV". In: *Physical Review D* 97.7 (Apr. 2018). Publisher: American Physical Society, p. 072001. DOI: 10.1103/PhysRevD.97.072001. URL: https://link.aps.org/doi/10.1103/PhysRevD.97.072001 (visited on 07/06/2025).

[46] Super-Kamiokande Collaboration et al. "Measurements of the atmospheric neutrino flux by Super-Kamiokande: Energy spectra, geomagnetic effects, and solar modulation". In: *Physical Review D* 94.5 (Sept. 2016). Publisher: American Physical Society, p. 052001. DOI: 10.1103/PhysRevD.94.052001. URL: https://link.aps.org/doi/10.1103/PhysRevD.94.052001 (visited on 07/06/2025).

[47] Super-Kamiokande Collaboration et al. "Search for proton decay via $p\ensuremath{\rightarrow}{
and $p\ensuremath{\rightarrow}{\ensuremath{\mu}}^{+}{\ensuremath{\pi}}^{0}$
with an enlarged fiducial volume in Super-Kamiokande I-IV". In: *Physical Review D* 102.11 (Dec. 2020). Publisher: American Physical Society, p. 112011. DOI: 10.1103/PhysRevD.102.112011. URL: https://link.aps.org/doi/10.1103/PhysRevD.102.112011 (visited on 08/17/2025).

[48] A Takenaka. "Search for Proton Decay via p \to e^++ \pi^0 and p \to \mu^++ \pi^0 with an Enlarged Fiducial Mass of the Super-Kamiokande Detector". PhD thesis. Japan: University of Tokyo, 2020.

[49] *TeVCat 2 | Home*. URL: https://tevcat2.tevcat.org/ (visited on 07/06/2025).

[50] The Super-Kamiokande Collaboration et al. "Atmospheric neutrino oscillation analysis with neutron tagging and an expanded fiducial volume in Super-Kamiokande I–V". In: *Physical Review D* 109.7 (Apr. 2024). Publisher: American Physical Society, p. 072014. DOI: 10.1103/PhysRevD.109.072014. URL: https://link.aps.org/doi/10.1103/PhysRevD.109.072014 (visited on 07/06/2025).

[51] E. Thrane et al. “SEARCH FOR ASTROPHYSICAL NEUTRINO POINT SOURCES AT SUPER-KAMIOKANDE”. en. In: *The Astrophysical Journal* 704.1 (Sept. 2009). Publisher: The American Astronomical Society, p. 503. ISSN: 0004-637X. DOI: 10.1088/0004-637X/704/1/503. URL: https://dx.doi.org/10.1088/0004-637X/704/1/503 (visited on 07/06/2025).

[52] Tibet AS Collaboration et al. “First Detection of sub-PeV Diffuse Gamma Rays from the Galactic Disk: Evidence for Ubiquitous Galactic Cosmic Rays beyond PeV Energies”. In: *Physical Review Letters* 126.14 (Apr. 2021). Publisher: American Physical Society, p. 141101. DOI: 10.1103/PhysRevLett.126.141101. URL: https://link.aps.org/doi/10.1103/PhysRevLett.126.141101 (visited on 07/06/2025).

[53] T. Wester. “DISCERNING THE NEUTRINO MASS ORDERING USING ATMOSPHERIC NEUTRINOS IN SUPER-KAMIOKANDE I–V”. PhD thesis. USA: Boston University.

[54] S. S. Wilks. “The Large-Sample Distribution of the Likelihood Ratio for Testing Composite Hypotheses”. In: *The Annals of Mathematical Statistics* 9.1 (Mar. 1938). Publisher: Institute of Mathematical Statistics, pp. 60–62. ISSN: 0003-4851, 2168-8990. DOI: 10.1214/aoms/1177732360. URL: https://projecteuclid.org/journals/annals-of-mathematical-statistics/volume-9/issue-1/The-Large-Sample-Distribution-of-the-Likelihood-Ratio-for-Testing/10.1214/aoms/1177732360.full (visited on 07/06/2025).

[55] G. T. Zatsepin et al. “Upper Limit of the Spectrum of Cosmic Rays”. In: *Soviet Journal of Experimental and Theoretical Physics Letters* 4 (Aug. 1966). Publisher: Springer ADS Bibcode: 1966JETPL...4...78Z, p. 78. ISSN: 0021-3640. URL: https://ui.adsabs.harvard.edu/abs/1966JETPL...4...78Z (visited on 07/04/2025).